FREQUENCY RESPONSE ANALYSIS AND RECONSTRUCTION WEIGHTING SCHEMES FOR MR ELASTOGRAPHY

A DISSERTATION SUBMITTED TO
THE GRADUATE SCHOOL OF ENGINEERING AND SCIENCE
OF BILKENT UNIVERSITY
IN PARTIAL FULFILLMENT OF THE REQUIREMENTS FOR
THE DEGREE OF
DOCTOR OF PHILOSOPHY
IN
ELECTRICAL AND ELECTRONICS ENGINEERING

By
Cemre Arıyürek
September 2020

FREQUENCY RESPONSE ANALYSIS AND RECONSTRUCTION WEIGHTING SCHEMES FOR MR ELASTOGRAPHY

By Cemre Arıyürek

September 2020

We certify that we have read this dissertation and that in our opinion it is fully adequate, in scope and in quality, as a dissertation for the degree of Doctor of Philosophy.

Ergin Atalar(Advisor)

Yusuf Ziya İder(Co-Advisor)

Emine Ülkü Sarıtaş Çukur

Behçet Murat Eyüboğlu

Esin Öztürk Işık

Hatice Kader Karlı Oğuz

Approved for the Graduate School of Engineering and Science:

Ezhan Karaşan
Director of the Graduate School

ABSTRACT

FREQUENCY RESPONSE ANALYSIS AND RECONSTRUCTION WEIGHTING SCHEMES FOR MR ELASTOGRAPHY

Cemre Arıyürek
Ph.D. in Electrical and Electronics Engineering
Advisor: Ergin Atalar
Co-Advisor: Yusuf Ziya İder
September 2020

Magnetic resonance elastography (MRE) non-invasively and quantitatively assesses the elasticity of the in-vivo tissue. In MRE, shear waves are induced to the tissue by an actuator, while phase-contrast images are obtained by magnetic resonance imaging (MRI). Finally, elasticity maps are generated using displacement information carried by phase-contrast images.

The direction and frequency of the induced shear waves could be crucial in MRE. Here, it is demonstrated by the frequency response MRE simulations that modes of the shear waves can be observed in the brain during MR elastography with high shear wave displacement values at the mode frequencies. High shear wave displacements, 10-20 times of the applied displacement, were observed at mode frequencies in phantom MRE experiments.

The second part of the thesis focuses on weighting schemes to combine multiple elasticity maps reconstructed from data collected for different excitation frequencies and motion direction.

A new weighting scheme, which maximizes the signal-to-noise ratio (SNR) of the final wave speed map, has been proposed for tomoelastography and Helmholtz inversions. For both inversion techniques, considering the noise on the complex MRI signal, the SNR of the reconstructed wave speed map was formulated by an analytical approach assuming a high SNR. Thus, with the proposed SNR weighting method, while not altering the accuracy or spatial resolution of the wave speed map, the SNR of the wave speed map has been improved by 2 and 1.6 times for tomoelastography and Helmholtz inversion, respectively. The bias occurring for low SNR data cases was eliminated in tomoelastography and reduced in Helmholtz inversion with the proposed SNR-weighted reconstructions.

Similarly, a strain-based weighting for MRE reconstruction has been introduced. Experimental results demonstrated that strain weights could prevent

artifacts at the boundaries of encapsulated tumors or tissues with membranes; however, further examination is required.

In this thesis, two independent contributions have been made to the field of magnetic resonance elastography. By showing the existence of modes of the shear waves in the body, new fronts are opened in the MRE actuation methods and safety. The improvements in the elasticity map inversions could lead to the routine use of MRE in clinical practice.

Keywords: magnetic resonance elastography, modes of shear waves, signal-to-noise ratio, octahedral shear strain, shear wave speed, elasticity, finite element method simulations, Monte Carlo simulations.

ÖZET

MR ELASTOGRAFİ'DE FREKANS YANITI ANALİZİ VE GERİÇATIM AĞIRLIKLANDIRMA YÖNTEMLERİ

Cemre Arıyürek
Elektrik ve Elektonik Mühendisliği, Doktora
Tez Danışmanı: Ergin Atalar
İkinci Tez Danışmanı: Yusuf Ziya İder
Eylül 2020

Manyetik rezonans elastografi (MRE), invaziv olmayan ve kantitatif olarak in-vivo dokunun elastikliğini değerlendirir. MRE'de, makaslama dalgaları bir aktüatör tarafından dokuya iletilirken, faz kontrast görüntüleri manyetik rezonans görüntüleme (MRG) ile elde edilir. Son olarak, elastiklik haritaları, faz kontrast görüntülerinin içerdiği yerdeğişimi bilgileri kullanılarak oluşturulur.

MRE'de dokuda oluşturulan makaslama dalgalarının yönü ve frekansı önemlidir. Bu tezde, MR elastografi sırasında, mod frekanslarında makaslama dalgasının yüksek yerdeğişimi değerleri ile makaslama dalgalarının modlarının beyinde gözlemlenebildiği frekans yanıtı MRE simülasyonları kullanılarak gösterilmiştir. Fantom MRE deneylerinde, uygulanan yerdeğişiminin, 10-20 katı olan yüksek yerdeğişimi dalgaları mod frekanslarında gözlemlenmiştir.

Tezin ikinci bölümü, farklı uyarma frekansları ve hareket yönü için toplanan verilerinin her birinden elde edilen elastiklik haritalarını birleştirmek için ağırlıklandırma yöntemlerine odaklanmaktadır.

Nihai dalga hızı haritasının sinyal-gürültü oranı (SGO) değerini maksimize eden yeni bir ağırlıklandırma yöntemi, tomoelastografi ve Helmholtz geriçatımları için önerilmiştir. Her iki geriçatım tekniği için, karmaşık MRI sinyalindeki gürültü bilgisi kullanılarak, dalga hızı haritalarının SGO değeri, yüksek SGO varsayımıyla analitik bir yaklaşımla formüle edilmiştir. Böylelikle önerilen SGO ağırlıklandırma yöntemi ile dalga hızı haritasının doğruluğunu veya uzaysal çözünürlüğünü değiştirmemekle birlikte, dalga hızı haritasının SGO'sunu tomoelastografi ve Helmholtz geriçatımı için sırasıyla 2 ve 1,6 kat iyileştirilmiştir. Ayrıca önerilen SGO ağırlandırma yöntemi sayesinde MRG versinin SGO değeri düşükken gözlemlenen yanlılık, tomoelastografide tamamen giderildi ve Helmholtz geriçatımında azaltıldı.

Benzer şekilde, MRE geriçatımı için gerinime bağlı bir ağırlıklandırma

önerilmiştir. Deneysel sonuçlar, gerinim ağırlıklandırmalı MRE geriçatımının, elastiklik haritasında kapsüllü tümörlerin veya membranlı dokuların sınırlarında oluşabilecek artefaktları önleyebileceğini gösterdi; ancak, bu konu daha detaylı incelenmelidir.

Bu tezde manyetik rezonans elastografi alanına iki bağımsız katkı yapılmıştır. Dokudaki makaslama dalgalarının modlarının varlığı gösterilerek, MRE uyarma yöntemlerinde ve MRE'nin güvenliği konularında yeni araştırma alanları açılmaktadır. Elastiklik haritası geriçatımındaki iyileştirmeler, klinik uygulamada MRE'nin rutin kullanımına faydası olabilir.

Anahtar sözcükler: manyetik rezonans elastografi, makaslama dalgalarının modları, sinyal-gürültü oranı, sekizyüzlü makaslama gerinimi, makaslama dalga hızı, elastiklik, sonlu elemanlar metodu benzetimleri, Monte Carlo benzetimleri.

Acknowledgement

Foremost, I would like to express my sincere appreciation to my advisor Prof. Ergin Atalar for his wise supervision, endless support and always encouraging me. He has taught me how to build a research project rather than giving a ready-project to work on. Hence, I owe my genuine thanks to him for my development as a researcher. Besides being a decent research advisor, he has been sincerely very supportive in my good and bad days throughout my graduate years. Also, I would like to thank him for providing us a great research environment at UMRAM.

I would like to state my deep gratitude to my co-advisor Prof. Yusuf Ziya İder for his supervision, enthusiastic encouragement and useful critiques of this research work.

Additionally, I am thankful to Assoc. Prof. Emine Ülkü Sarıtaş for her valuable feedbacks for my research in thesis committee meetings. I was very lucky to benefit from her expertise on MRI sequences and reconstruction.

I am grateful to Prof. Hatice Kader Karlı Oğuz for our discussions on MR elastography, accepting to be in the jury and her useful feedbacks on the this thesis.

I would like to express my special thanks to Prof. Behçet Murat Eyüboğlu and Assoc. Prof. Esin Öztürk Işık for showing interest in my work and allocating their precious time to read and giving critical comments on this thesis.

I am indebted to Assoc. Prof. Dr. Arif Sanlı Ergün for his beneficial feedbacks on my research at the thesis committee meetings.

Furthermore, I would like to express my gratitude to UMRAM Atalar lab and administrative members, namely Bilal, Ehsan, Süheyl, Reza, Manouchehr, Erkan Dorken, Said, Mert, Fatih, Ziba, Aydan Ercingöz and Elif Ünal, and former members, namely Koray, Alireza, Uğur, Berk, Umut, Taner, Mustafa Can, Safa, Redi, Volkan, Esra, Ali Çağlar, Emre. I acknowledge Bilal Taşdelen for his contributions to my research. In addition, I was very lucky to be working in the same group with Dr. Koray Ertan that he enhanced the bliss of my graduate years. Also, I thank to Dr. Alireza Sadeghi-Tarakameh for his friendship. I acknowledge my gratitude to Dr. Esra Abacı Türk for her guidance and friendliness. It was a great pleasure having the oppurtunity to work with her at the beginning of my

graduate studies. Moreover, I am thankful to Safa Özdemir for his contributions on the detector coil implementation.

Additionally, I am very grateful to my friends and colleagues at UMRAM, for their support and friendship. Especially, I would like to acknowledge Mustafa Ütkür for his help with the design of the 3D printed bite actuator. I would like to express my gratitude to Sevgi Gökçe Kafalı and Gülşah Yıldız for their friendships and being perfect roommates at the past ISMRM conferences.

I am thankful to Mürüvet Parlakay, Aydan Gencel and Aslı Tosuner for their helps with the administrative issues for all my years at Bilkent University.

Finally, I am grateful to my husband (Yalım İşleyici) for his accompaniment, endless support and motivating me at every step of this work. I owe gratitude to my brother (Sinan Arıyürek), my mother (Sezin Arıyürek) and my father (Macit Arıyürek) for their unconditional supports. I would like to thank to my cat Nala for accompanying me at late night studies. I am thankful to Simin İşleyici, Meltem İşleyici, Hasan İşleyici and Bengü Kevinç Arıyürek for their supports during my graduate studies.

I would also like to thank to the faculty members, my relatives and friends who have supported and encouraged me during my graduate years.

This research was supported and funded by the TÜBİTAK1001 (Award Number: 117E817).

Contents

1 Introduction **1**
1.1 Motivation . . . 1
1.2 Background . . . 2
1.3 Outline . . . 7

2 Modes of Shear Waves in MRE **9**
2.1 Introduction . . . 9
2.2 Methods . . . 10
2.2.1 Phantom Simulations and Experiments . . . 10
2.2.2 Human Brain Simulations and Experiments . . . 15
2.3 Results . . . 18
2.3.1 Phantom Simulations and Experiments . . . 18
2.3.2 Human Brain Simulations and Experiments . . . 20
2.4 Discussion and Conclusion . . . 21

3 SNR Weighting for Shear Wave Speed Reconstruction in Tomoelastography **31**
3.1 Introduction . . . 31
3.2 Theory . . . 33
3.3 Methods . . . 41
3.3.1 Reconstructions . . . 41
3.3.2 Simulations . . . 42
3.3.3 Validation of analytical SNR derivations and performance analyses . . . 46
3.3.4 MRI experiments . . . 47

3.4 Results 49
3.4.1 Simulation results 49
3.4.2 Experimental results 51
3.5 Discussion 52
3.6 Conclusion 58

4 Improving the SNR and Correcting the Bias in Elastograms in Helmholtz Inversion for MRE 67
4.1 Introduction 67
4.2 Theory 68
4.3 Methods 69
4.4 Results 70
4.5 Discussion and Conclusion 71

5 Use of Octahedral Shear Strain in the MRE Inversion 75
5.1 Introduction 75
5.2 Theory 76
5.3 Methods 77
5.4 Results 77
5.4.1 Experimental results 79
5.5 Discussion and Conclusion 81

6 Discussion and Conclusion 88

List of Figures

1.1 Electromechanical actuator 3
1.2 MRE experiment with two phase offsets 5

2.1 Two excitation setups for spherical flask phantoms. (a) Back rotation, (b) center rotation 11
2.2 MRE experimental setup 12
2.3 Three spherical flask phantoms having different Young's modulus values 12
2.4 Two acquisitions were made in each scan by switching polarity of the zeroth and first moment nulled MEG, in an interleaved fashion. The shear wave displacement images were formed by taking RSS of in and quadrature phase images obtained from two scans for each excitation frequency. 13
2.5 Illustration of back rotation experimental setup demonstrating the detector coil, phantom, actuator coil for two different view angles. The actuator's rotation under B_0 field while sinusoidal current is applied to the actuator coil is depicted in (b). As the applied current changes its polarity between negative and positive current values sinusoidally, the rotation directions switch between to rotation directions shown by orange and green arrows. 14
2.6 Young's modulus maps for (a) three transverse slices (b) the central transverse slice 16

2.7 Total displacement ($\sqrt{x^2 + y^2 + z^2}$) measured on the surface of the head for three motion directions. Orientation of the head is given on the upper left corner. Note that colorbar scale is in arbitrary units (a.u.). 17
2.8 EPI-SE sequence with MEG used in the brain experiments 18
2.9 Measured displacements for the simulated MRE for three spherical flask phantoms having different Young's Moduli and two types of excitation 19
2.10 Results for back rotation experiment, conducted on phantom with agar-agar concentration of 0.85%. Peak shear wave displacement in phantom, induced voltage on the detector coil, peak displacement of the actuator computed from measured induced voltage on the detector coil, displacement ratio obtained by dividing displacement in the phantom by applied displacement, with respect to excitation frequency 20
2.11 Displacement ratio images for each excitation frequency for the same experiment shown in Figure 2.10. Mode frequency is 34 Hz since maximum displacement ratio is observed. 21
2.12 Experimental results for displacement ratio versus frequency plots for three phantoms, each repeated three times. Note that mode frequencies are indicated by vertical grids on the plot. 22
2.13 Results for center rotation experiment, conducted on phantom with agar-agar concentration of 0.65%. Peak shear wave displacement in phantom, induced voltage on the detector coil, peak displacement of the actuator computed from measured induced voltage on the detector coil, displacement ratio obtained by dividing displacement in the phantom by applied displacement, with respect to excitation frequency 23

2.14 Results for center rotation experiment, conducted on phantom with agar-agar concentration of 0.75%. Peak shear wave displacement in phantom, induced voltage on the detector coil, peak displacement of the actuator computed from measured induced voltage on the detector coil, displacement ratio obtained by dividing displacement in the phantom by applied displacement, with respect to excitation frequency 24
2.15 Results for center rotation experiment, conducted on phantom with agar-agar concentration of 0.85%. Peak shear wave displacement in phantom, induced voltage on the detector coil, peak displacement of the actuator computed from measured induced voltage on the detector coil, displacement ratio obtained by dividing displacement in the phantom by applied displacement, with respect to excitation frequency 25
2.16 Displacement ratio images for each excitation frequency for the same experiment shown in Figure 2.13. Mode frequency is 31.5 Hz since maximum displacement ratio is observed. 26
2.17 Frequency response analysis of the brain model by sweeping excitation frequency for three motions of the head. 27
2.18 Photo showing the bite actuator used in the volunteer experiments 27
2.19 Images demonstrating displacement encoded in z-direction acquired for eight phase offsets 28
2.20 Images demonstrating displacement encoded in x-direction acquired for eight phase offsets 28
2.21 Images demonstrating displacement encoded in y-direction acquired for eight phase offsets 29
2.22 Maximum total displacement measured in the brain, actuator displacement and displacement ratio with respect to excitation frequencies depicted for three volunteer experiments 30

3.1 Block diagram of the original tomoelastography reconstruction. Amplitude-normalized complex-difference MRE images are the inputs of the reconstruction. In the last step of the reconstruction, weighted averaging is used to combine multiple estimations of the wave speed maps. The weights, W_{lmn}, in the original tomoelastography inversion are $\hat{u}^4_{0lmn}$. 35

3.2 (a) Simulation phantoms depicting ground truth values for the real part of their wave speeds. (b) Experimental phantoms showing the agar-agar powder concentrations for the background and inclusions. 43

3.3 (a) Solidifying the background around the rods where inclusions will be poured. (b) Agar-agar solutions are poured after removal of the rods, one by one. (c) Identical box having a cut surface to be used in the experiment. (d) Phantom in B is placed inside the cut box, on the patient table horizontally, excitation is applied by a plate placed through the window opening of the box, driven mechanically. 49

3.4 Validation of analytical approximations for the SNR by comparing it to the computed SNR using Monte Carlo simulations. (a) The SNR of the wave speed versus the SNR of the complex MRI signal for analytical and computed SNR values. (b) (Top) Ratio of the 2D-averaged mean of the wave speed reconstructed over 100 repetitions to the analytical mean wave speed at each image SNR. (Bottom) Ratio of the 2D-averaged SD of the wave speed reconstructed over 100 repetitions to the analytical SD of the wave speed at each image SNR. It can be observed that analytical derivations hold for ${}^i\Psi_{mn}(\vec{r}) \geq 3$ since the ratio of SDs becomes steady. (c) Comparison of analytical and MCS computed SNR, where the x-axis indicates the angle of the plane propagating in the x-y plane (i.e., $\arg\{\vec{k}\}$) when SNR=5, and 12 directional filters are present. 59

3.5 (A) Wave speed maps (B) line profiles for center horizontal line (C) mean±SD plots for each region for the two weighting schemes for SP#4. Assigned shear wave speed values are 2.2, 2.5, 3 and 2 m/s for background, inclusion #1-4, respectively. 60
3.6 Wave speed values plotted for a cross-sectional line near the step between two mediums to analyze edge response for the two weighting schemes for (a) SP#2 and (b) SP#3. 60
3.7 SNR performances computed by Monte Carlo simulations. 2D-averaged mean and standard deviation of wave speed maps, normalized to the ground truth wave speed, versus the image SNR. . 61
3.8 Reconstructed wave speed maps for the 3D healthy human abdomen model for the no-noise and noise-added case. The ground truth is also given, demonstrating the magnitude of the assigned wave speed distribution for the simulations. 61
3.9 For EP#1 (a) Reconstructed wave speed maps (b) Selected ROIs for measuring wave speed values, depicted on the MRE magnitude image. The ROI for the background is selected as the region between the green curves. (c) Mean and SD values over the ROI, shown by squares and bars, respectively. 62
3.10 Reconstructed wave speed maps and weights for the two weighting schemes at each frequency in addition to the combined wave speed maps for EP#2. 63
3.11 For EP#2 (a) Selected ROIs for measuring wave speed values, depicted on the MRE magnitude image. The ROI for the background is selected as the region between the blue curves. (b) Mean and SD values over the ROI, shown by squares and bars, respectively. 64
3.12 (a) Single frequency and combined multifrequency results for wave speed maps for MRE abdomen data. (b) Anatomical ROIs (liver (red) and spleen (blue)), selected on the MRE magnitude image, for measuring the mean and SD of the estimated shear wave speeds. 65

3.13 Reconstructed wave speed maps using SNR weights with and without thresholding for the 3D healthy human abdomen model noise-added case. The ground truth isalso given, demonstrating the magnitude of the assigned wave speed distribution for the simulations. 66

4.1 Validation of analytical approximations by Monte Carlo simulations are demonstrated by mean, standard devitation (SD) and SNR of magnitude of complex shear modulus versus image SNR. The minimum image SNR value that analytical approximations hold is determined as 10. 70
4.2 (a) Magnitude of complex shear modulus ($|G^*|$) maps for simulation phantom for no-noise and noise added case. (b) Ground truth for $|G^*|$ map for the simulation phantom. (c) Horizontal profiles of $|G^*|$ maps in (a) and (b). 71
4.3 Estimated magnitude of mean complex shear modulus ($|G^*|$) normalized to the ground truth and SNR of $|G^*|$ versus mean image SNR. Hence, mean $|G^*|$ normalized to the ground truth is desired to be equal to 1. 72
4.4 $|G^*|$ maps for the simulated brain MRE data for the no-noise and noise added cases, compared with the ground truth $|G^*|$. 73
4.5 Reconstructed $|G^*|$ maps for in-vivo human brain. 74

5.1 (a) Wave speed maps (b) line profiles for center horizontal line (c) mean±SD plots for each region for the two weighting schemes for SP#4. Assigned shear wave speed values are 2.2, 2.5, 3 and 2 m/s for background, inclusion #1-4, respectively. 78
5.2 Wave speed values plotted for a cross-sectional line near the step between two mediums to analyze edge response for the two weighting schemes for (a) SP#2 and (b) SP#3. 79
5.3 SNR performances computed by Monte Carlo simulations. 2D-averaged mean and standard deviation of wave speed maps, normalized to the ground truth wave speed, versus the image SNR. . 80

5.4 Reconstructed wave speed maps for the 3D healthy human abdomen model for the no-noise and noise-added case. The ground truth is also given, demonstrating the magnitude of the assigned wave speed distribution for the simulations. 81
5.5 Ground truth, conventional multifrequency Helmholtz inversion (no-weighting) and OSS-weighted Helmholtz inversion for the brain simulation data. Differences between no-weighting and OSS-weighted inversions are observed mainly in sulci of the brain. . . . 82
5.6 For EP#1 (a) Reconstructed wave speed maps (b) Selected ROIs for measuring wave speed values, depicted on the MRE magnitude image. The ROI for the background is selected as the region between the green curves. (c) Mean and SD values over the ROI, shown by squares and bars, respectively. 83
5.7 Reconstructed wave speed maps and weights for the two weighting schemes at each frequency in addition to the combined wave speed maps for EP#2. 85
5.8 For EP#2 (a) Selected ROIs for measuring wave speed values, depicted on the MRE magnitude image. The ROI for the background is selected as the region between the blue curves. (b) Mean and SD values over the ROI, shown by squares and bars, respectively. 86
5.9 (a) Single frequency and combined multifrequency results for wave speed maps for MRE abdomen data. (b) Anatomical ROIs (liver (red) and spleen (blue)), selected on the MRE magnitude image, for measuring the mean and SD of the estimated shear wave speeds. 86
5.10 Conventional multifrequency Helmholtz inversion (no-weighting) and OSS-weighted Helmholtz inversion for healthy human experiment data. Differences between two images can be observed mainly in splenium of the corpus collosum and sulci, shown by the white arrows and the purple arrow, respectively. Stiff and anisotropic splenium of corpus callosum can be observed in OSS-weighted averaging inversion but it cannot be observed clearly in the inversion without weighting. 87

List of Tables

2.1 Material properties of the segmented parts of the brain 15

3.1 Material properties of the segmented parts of human abdomen . . 45

Chapter 1

Introduction

1.1 Motivation

Mechanical properties of the tissues change due to their physiological changes and pathological states. To detect the alteration in the elasticity of the tissue, manual palpation examination is conducted on various tissues. Unfortunately, this examination sometimes may be followed by biopsy.

The elasticity map of the organ/tissuse can be imaged by magnetic resonance elastography (MRE), which is known as "palpation by magnetic resonance imaging (MRI)". MRE quantitatively and non-invasively assesses the elasticity of in-vivo tissue [1]. MRE can measure the elasticity of tissues in deeper parts of the body or enclosed by bone. Hence, MRE can investigate elasticity of various tissues such as heart [2, 3], liver [4, 5], skeletal [6–8], breast [9, 10], brain [11–14].

In MRE, shear waves are induced to the tissue by an actuator while shear wave displacement information is encoded to the phase of MRI signal. Elasticity maps are generated by reconstructing phase difference images.

Research groups use different actuator systems and excitation frequencies for

the same tissue of interest. Displacement response of the tissue depends on excitation frequency and direction. In the brain, modes of shear waves can be formed during MRE since it is enclosed by bone, demonstrated by brain simulations in the M.Sc.'s thesis work [15] and later by McGrath et al. [16]. However, modes of shear waves have not been investigated by phantom or in-vivo brain experiments.

Shear wave displacement data can be collected for three directions of motion and various excitation frequencies. To achieve a final elasticity map by combining reconstructions obtained from all spatial directions and excitation frequencies, the use of weights is inevitable. The quality metrics, such as accuracy, resolution and SNR, of the elastogram are essential for clinical use of MRE. To increase the quality of the elasticity map, weighting schemes for combining multiple elastograms can be developed.

1.2 Background

The first step of MRE is inducing shear waves into the tissue by an actuator system. As an example, schematic of an electromechanical is depicted in Figure 1.1. A sinusoidal current is applied to the actuator coil. Under B_0 field, due to Lorentz force [1], actuator rotates to +z and -z directions with the positive and negative cycles of the sinusoidal current. Hence, the plate touching the surface of the phantom moves sinusoidally in z- direction, inducing shear waves into the phantom.

Placing the actuator in different orientations results in different propagation directions of shear waves. Also, different actuator systems induce shear waves into the tissue in different propagation directions. For instance, head cradle, actuator results in nodding motion of the head in MRE [14]. Depending on the placement and design of the pneumatic pillow actuator may result in nodding or naying of the head [12]. The bite actuator systems result in head bobble motion [13]. Moreover, the excitation frequencies used in MRE experiments are commonly in the range of 25-65 Hz [17]. The frequency dependence of brain elasticity has been

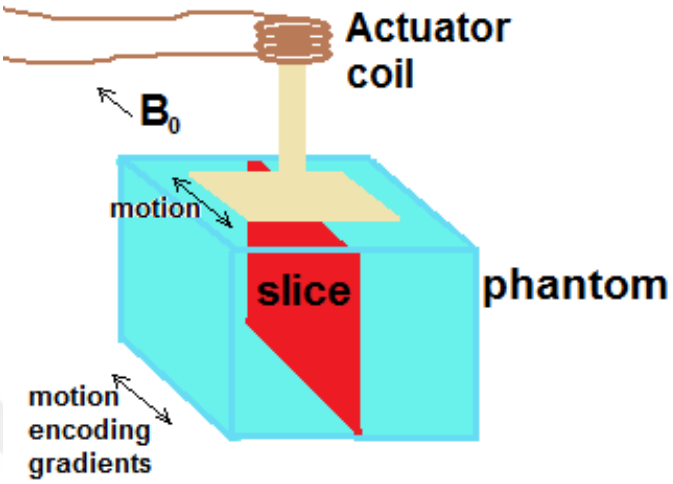


Figure 1.1: Electromechanical actuator

studied; however, frequency dependence of shear wave displacement and modes of shear waves have not been investigated in depth [15, 16, 18].

In the brain MRE simulations, eigenmodes of the brain models were observed at eigenfrequencies [15, 16, 18]. If modes of shear waves can be formed during brain MRE scans, there are a few outcomes of this finding. First, safety limits for the brain MRE should be investigated further [19]. Second, skull-brain motion transfer analysis investigated by modes of shear waves could contribute to examine traumatic brain injury (TBI) studies. Note that using MRE to understand skull-brain motion dynamics is common recently [20–22]. Third, detecting mode frequencies could be important for determining change in elasticities since it has been shown that alteration in elasticity results in shift in mode frequency [15, 18]. Furthermore, there could be a few more outcomes such as increase in motion sensitivity, design of actuator systems and effect of modes in the inversions [16, 23].

While inducing shear waves into the tissue by an actuator, shear wave motion is encoded in the phase of the complex MRI signal using motion encoding gradients (MEGs). Motion encoding can be done in all three directions.

In the presence of a magnetic field gradient $\vec{G}_r(t)$, transverse magnetization

phase of a moving spin is

$$\phi(\tau) = \gamma \int_0^\tau \vec{G}_r(t) \cdot \vec{r}(t) dt, \tag{1.1}$$

where γ is the gyromagnetic ratio, $\vec{r}(t)$ is the position vector of the moving spin and τ is the total duration of the gradient field.

For a sinusoidally moving spin with initial position $\vec{r_0}$, wavenumber k, frequency ω, phase shift with respect to the gradient waveform α and displacement vector ξ_0, the position vector is given as:

$$\vec{r}(t) = \vec{r_0} + \vec{\xi_0} e^{j(\vec{k} \cdot \vec{r} - \omega t + \alpha)}. \tag{1.2}$$

Exploiting MEGs, MRI sensitizes the displacement of the shear waves in the tissue. Two acquisitions are made in each scan by switching polarity of MEG. Phase difference of the two acquisitions is computed to obtain displacement of shear waves.

Typically, period of the MEGs are matched with period of the applied mechanical vibration. Thus, for a trapezoidal MEG having a period of $T = 2\pi/w$, substituting Equation 1.2 into Equation 1.1 and ignoring rise times, the phase difference is formulated as:

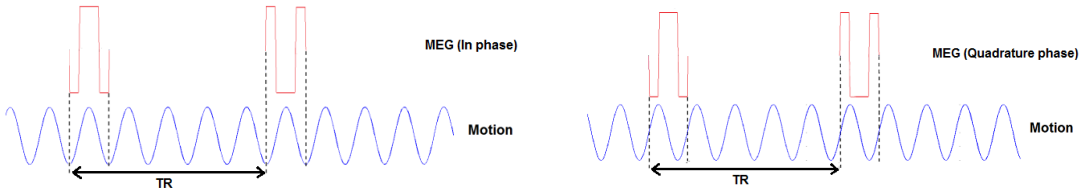
$$\phi(\vec{r}, \alpha) = \frac{2\gamma NT(\vec{G} \cdot \xi_0)}{\pi} sin(\vec{k} \cdot \vec{r} + \alpha), \tag{1.3}$$

where G is amplitude of the MEG ($\vec{G}_r(t)$), N is the number of MEGs.

If sinusoidal MEGs with a period of $T = 2\pi/w$ are utilized, then the phase difference is formulated as:

$$\phi(\vec{r}, \alpha) = \frac{\gamma NT(\vec{G} \cdot \xi_0)}{2} cos(\vec{k} \cdot \vec{r} + \alpha). \tag{1.4}$$

Ideally, acquiring MRE data at two orthogonal phase offsets should be sufficient to fully cover the shear wave propagation; however, due to nonlinearities,



(a) In-phase (b) Quadrature-phase

Figure 1.2: MRE experiment with two phase offsets

harmonics of the applied displacement are also observed [24]. Therefore, it is common to acquire more than two phase offsets. Thus, discrete Fourier transform (DFT) is computed, and only the first harmonic is selected while filtering other frequency components. As an example, relative timings of MEG and motion are depicted for two phase offsets in Figure 1.2. Two acquisitions were made in each scan using MEG, by switching polarity of the zeroth and first moment nulled MEG, having same frequency with excitation frequency, in an interleaved fashion. Hence, from these two acquisitions, phase difference image, related to shear wave displacement, is obtained. MRE data can be collected at multiple phase offsets, which is the phase difference between MEG and motion. In Figure 1.2, data are collected for two phase offsets, namely in-phase and quadrature-phase.

The last step of MRE is to compute elasticity maps from the phase difference images. To generate elastograms from shear wave displacement images, various inversion algorithms are proposed, such as local frequency estimation (LFE) [25], nonlinear inversion [26, 27], Helmholtz inversion [28–30], Multifrequency Dual Elasto-Visco (MDEV) inversion [31], tomoelastography [32], multimodel direct inversion (MMDI) [33], artificial neural networks (ANN) based inversion [34] and heteregeneous multifrequency direct inversion (HMDI) [35].

Complex shear modulus is usually reported in MRE, where the real part is the storage modulus related to elastic properties of the tissue and the imaginary part is the loss modulus related to viscous properties of the tissue. Since in the body, the density of the tissue, ρ_0, is relatively constant and the shear modulus, G, is related to the wave speed, c, by $G = c^2\rho_0$, while neglecting the viscous damping, the wave speed map can also be viewed as the elasticity map of the

body. Hence, both shear modulus and wave speed maps are used as elastograms in MRE. Some common MRE inversion techniques, tomoelastography [32] and Helmholtz inversion [29], will be covered in more detail in the following Chapters.

In MR elastography inversion, to achieve a final elasticity map by combining reconstructions obtained from all spatial directions and excitation frequencies, use of weights is necessary. In the literature, all of the weighting schemes are essentially based on amplitude of displacements. Conversely, some of the multi-inversion techniques do not use any weighting, such as Helmholtz inversion [29].

In tomoelastography, wave speed distribution in the body is computed for each of the directions and frequencies. Then, the computed wave-speed distributions are weighted averaged with the fourth power of amplitude of the displacement in each direction and frequency. This amplitude-weighting allows only the wave-speed distributions that are computed from high wave amplitudes contribute to the averaging. It should be noted that for single frequency studies, there are similar weighting schemes based essentially on amplitude, to combine reconstructions from multi-directions. However, amount of strain, which is the more relevant quantity for shear modulus [36], is not sufficiently prioritized in aforementioned techniques. The strain is directly related to the shear, hence the magnitude of the shear strain produced by motion is more essential than the magnitude of the shear wave displacement. In fact, it has been shown by McGarry et al. [36] in their nonlinear inversion method for elasticity reconstruction that strain-SNR measured by the octahedral shear strain (OSS) SNR is more useful than motion-SNR to determine the reliability of the reconstructed elastogram from the displacement data.

Another idea is combining multi-inversion results in a way that will yield the elastogram with the maximum possible SNR [37]. This can be achieved by combining multi-inversion results by weighting with the SNR of the wave-speed maps obtained for different directions and frequencies. Although SNR of the wave speed map is critical for diagnostic purposes, there are only a few studies on the SNR in MR elastography, focusing on SNR analyses of the acquired displacement

data and its relation to the reliability of the elastogram generated [36, 38]. Additionally, acquisition techniques have been developed to increase the SNR of the recorded MRE data [39, 40]. However, SNR of the elasticity map has not been investigated yet. Considering the noise on the complex MRI signal, SNR of the reconstructed elasticity map can be formulated analytically. The findings can be beneficial for combining multi-directional, multifrequency MRE data to obtain high quality elasticity maps.

1.3 Outline

Previously in the M.Sc.'s thesis work of the author of this thesis [15], modes of shear waves in the brain model have been validated by MRE simulations [18]. However, they could not have been verified by experiments. In the brain MRE experiments, it has been observed that falx cerebri significantly affects the propagation of shear waves in the brain. Hence, it is proposed to update the brain model by including the falx cerebri in the model. Furthermore, experiments on head-mimicking phantoms are followed by in-vivo brain experiments. Additionally, to measure the displacement applied by the actuator, a more reliable methodology than optical method [1] is used, such as detector coils [24]. Note that measuring applied displacement is required to compute displacement ratio of the displacement in the phantom or tissue to the applied displacement, thus mode frequencies could be determined from the frequency response of the phantom or tissue (i.e., displacement ratio).

In Chapter 2, modes of shear waves observed in MR elastography are investigated by phantom simulations and experiments, followed by human brain simulations and experiments.

The second part of the thesis focuses on weighting schemes to combine multiple elasticity maps obtained for different excitation frequency and directions of motion. Tomoelastography [32] and Helmholtz inversion [31] are common inversion techniques that combine elasticity results for multifrequency and multidirection

data, to obtain a single elastogram.

One idea could be to maximize signal-to-noise ratio (SNR) of the final elastogram. Hence, each elasticity map should be weighted by its SNR in the combination. Hence, SNR derivation of the elastogram is required. Assuming high SNR, the noise characteristics of each elasticity map by considering the Gaussian noise on the MRI signal are derived. In other words, it is assumed that Gaussian noise on the MRI signal remains as Gaussian on the elastogram despite the nonlinear operations. By Monte Carlo simulations, the SNR threshold for high SNR assumption is determined. In the SNR weighting scheme, it is proposed to use SNR weights to combine the elasticity maps and discard the data that does not satisfy the SNR threshold.

For tomoelastography, derived weighting scheme was compared to the conventional weighting scheme, which uses fourth power of the amplitude of the filtered displacement, for three performance metrics, namely estimation accuracy, resolution and SNR. In addition, results are provided for simulation and experiment data acquired for phantoms and human abdomen in Chapter 3.

For Helmholtz inversion, conventional and SNR-weighted reconstruction results for simulation phantoms, brain simulation and in-vivo brain data are given in Chapter 4.

As a second weighting scheme, octahedral shear strain (OSS) weighting has been proposed. It has been demonstrated that strain is a more reliable quantitiy that amplitude of the displacement to decide on the quaility of the MRE data for the inversion [36]. Reconstruction results for simulation and experiments for phantoms, human abdomen and brain are presented in Chapter 5.

Finally, findings of this thesis are discussed and concluded in Chapter 6.

Chapter 2

Modes of Shear Waves in MRE

2.1 Introduction

Most of the MRE studies, focused on post-processing of phase-contrast shear wave images to estimate stiffness of the tissue. In other words, several groups have worked on developing image processing algorithms for elastography mapping. In addition to wavelength information, dependence of shear wave displacement amplitude to the frequency and excitation direction carry important information about material properties of the tissue.

Modes of shear waves have not been recognized and investigated before. There are various outcomes of existence of modes. One of them is motion sensitivity can be increased since greater output motion (i.e., motion in the brain) can be obtained with small input motion (i.e., motion of the actuator) at mode frequencies. Another outcome is that safety issues in MRE should be reconsidered. Also, since TBI studies skull-brain motion dynamics, analyzing modes of shear waves in MRE, which examines transferred motion from skull to brain, could be beneficial for them as well. Furthermore, modes of vibration of an object are related with its material properties. In addition, modes of shear waves formed in tissues may provide insight on the excitation frequency and direction to be used in MRE for

higher shear wave displacement. Although various actuator systems are implemented for inducing shear waves into a tissue, displacement response of tissues to excitation direction or frequency has not been studied. Use of MRE data acquired at the eigenfrequency in the inversion is another discussion point [16, 23].

In my M.Sc.'s thesis work [15], it has been demonstrated that modes of shear waves of the brain can be excited in MR elastography by eigenfrequency and frequency domain analysis simulations. Here, frequency analysis of the brain model was re-performed by including falx cerebri, which significantly affects the propagation of shear waves. Additionally, before proceeding with in-vivo experiments, MRE experiments on head-mimicking spherical flask phantoms were performed. The displacement of the actuator was measured by detector coil [24] instead of the optical method [1]. To reduce the scan time in volunteer experiments EPI-SE with MEG was used for brain MRE experiments.

2.2 Methods

2.2.1 Phantom Simulations and Experiments

To investigate modes of shear waves on spherical flask phantoms, the phantoms were excited by center rotation and by back rotation. In COMSOL Multiphysics (COMSOL, Sweden), solid mechanics under structural mechanics module is used for all FE simulations. Frequency domain analysis was performed for two cases. In the first case (i.e., back rotation), spherical phantom enclosed by glass was excited by inducing rotation to the head by predefined sinusoidal displacement, having 2 cm peak to peak displacement, to two pistons with a phase difference of π. Note that rotation of phantom was about z-axis. Simulations were repeated for three phantoms having different agar-agar powder concentrations resulting in different shear moduli. Agar-agar powder concentrations were 0.65%, 0.75% and 0.85% and corresponding shear moduli were 6, 7.7, 10 kPa, respectively. Poison ratio and density were assigned as 0.499 and 1040 kg/m^3, respectively.

In the second case (i.e., center rotation), the same three phantoms were rotated at their center about z-axis by predefined displacement having 2 cm peak to peak displacement.

For the experiments, implemented setups for back and center rotation are shown in Figure 2.1. For the back rotation, phantom was rotated by two pushing-pulling rods attached at the back of the phantom. For the center rotation, phantom was directly rotated by a rod attached to the center of phantom.

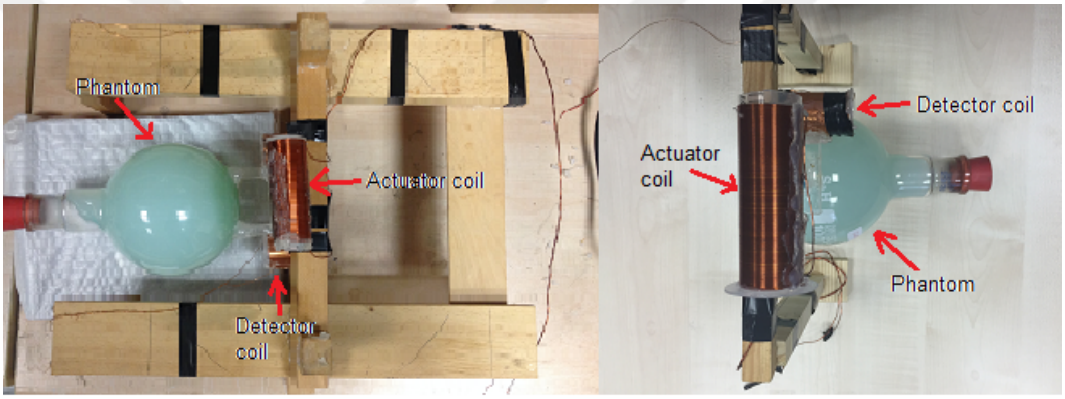


Figure 2.1: Two excitation setups for spherical flask phantoms. (a) Back rotation, (b) center rotation

A schematic of the experimental setup is shown in Figure 2.2. Optical trigger event is set in the beginning of the sequence. As the sequence starts optical trigger is read by the sensor and its output signal triggers the signal generator to generate sinusoidal signal continuously. Finally, the sinusoidal current is amplified and fed to the actuator which is connected in series with a resistor.

Phantoms were prepared using agar-agar powder (Agar Agar Kobe I pulv., Roth, Karlsruhe, Germany). For the phantom preparation, recipe explained in Hamhaber et al. [41] was followed. The mixture of agar-agar powder and boiled water was boiled for about 2 min. Phantoms with different shear modulus values were prepared by using varying amounts of agar-agar powder.

MRE experiment was conducted on three spherical flask phantoms with agar-agar powder concentrations (shear moduli) of 0.65% (6kPa), 0.75% (7.7kPa) and

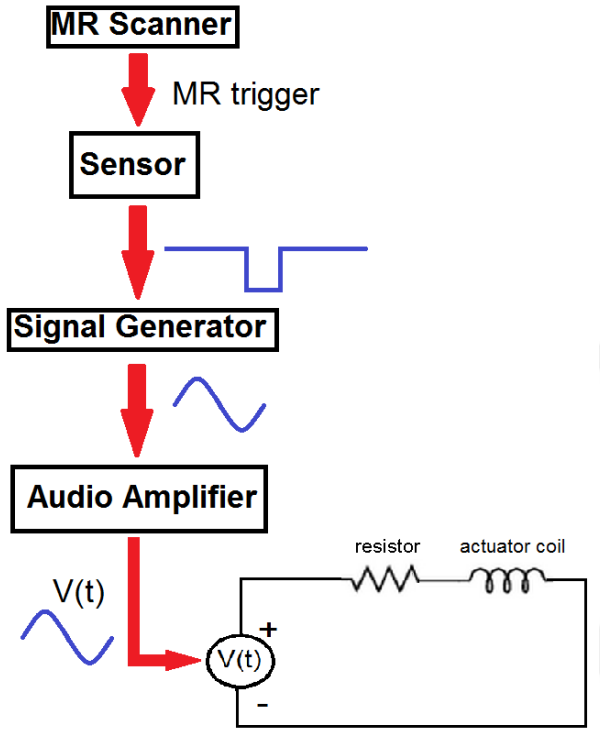


Figure 2.2: MRE experimental setup

0.85% (10kPa) (Figure 2.3).

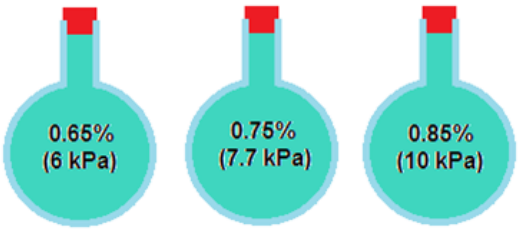


Figure 2.3: Three spherical flask phantoms having different Young's modulus values

Phantoms were rotated about y-axis (anterior-posterior) using the actuator setup shown in Figure 2.1a. The motion was induced continuously and the frequency of excitation was swept from 25 to 45.5 Hz, with 0.5 Hz steps. Peak-to-peak current applied to the actuator coil was kept constant during all experiments in the range of 1.75-1.85 A. Two acquisitions were made in each scan using a GRE pulse with motion encoding gradient, by switching polarity of the zeroth and first

moment nulled MEG, having same frequency with excitation frequency, in an interleaved fashion. The shear wave displacement images were formed by taking root of sum of squares (RSS) of two phase difference images at steady state of shear waves having $\pi/2$ phase difference obtained from two scans for each frequency (Figure 2.4). Peak of the RSS image was used as a measure of shear wave displacement magnitude. Note that Goldstein method [42] was used for 2D unwrapping of phase difference images.

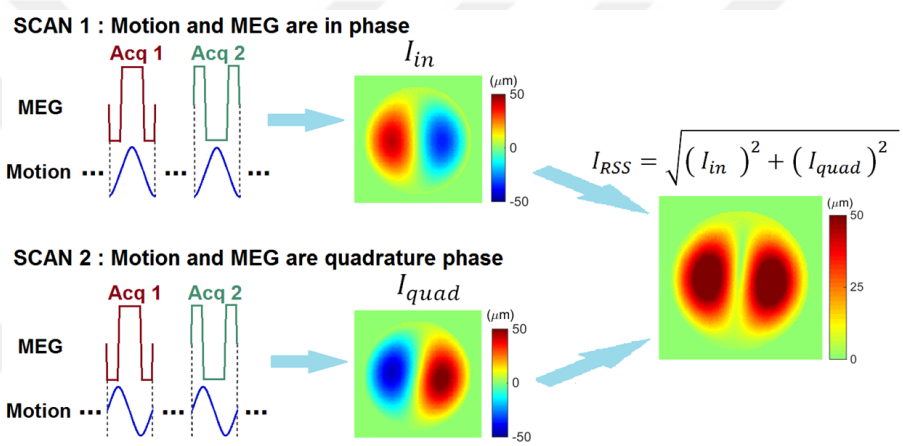
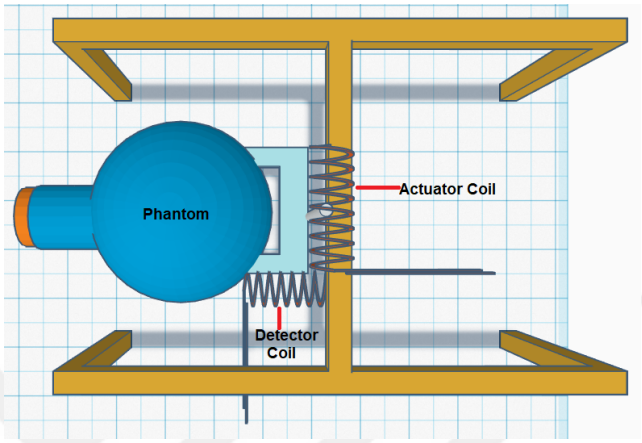


Figure 2.4: Two acquisitions were made in each scan by switching polarity of the zeroth and first moment nulled MEG, in an interleaved fashion. The shear wave displacement images were formed by taking RSS of in and quadrature phase images obtained from two scans for each excitation frequency.

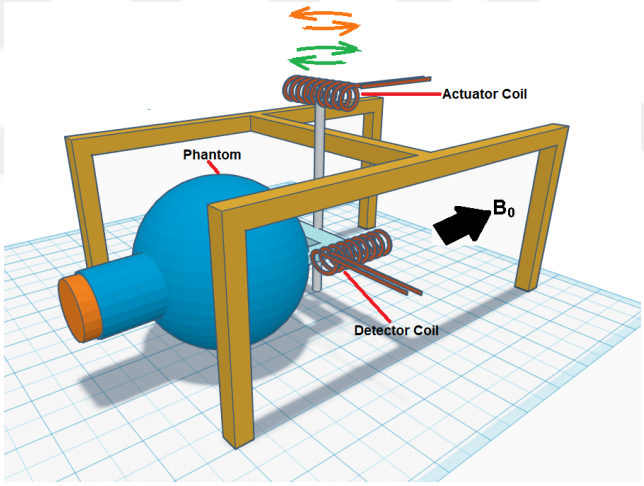
Detector coils were mounted on the actuator system to measure the amount of displacement applied by the actuator to the phantoms [24]. Illustration of the back rotation experimental setup depicting actuator coil, rotation direction of the actuator coil, detector coil and phantom is given in Figure 2.5. In the experiments, a spherical flask phantom (1L), an actuator coil (radius=1.5 cm, number of turns=91), a detector coil (radius=1.5 cm, number of turns=72) are used. The setup was placed on the patient table approximately 30° tilted with respect to B_0 direction to measure the induced voltage on the detector coil properly.

Displacement ratio is defined as dividing shear wave displacement to actuator displacement, which has been obtained from the measured induced voltage on the detector coil. Central transversal slices of the phantoms were selected for imaging and MEG was in the slice selection direction. All experiments were repeated three

times in 1-6 weeks to test the repeatability.



(a) Top view



(b) Side corner view

Figure 2.5: Illustration of back rotation experimental setup demonstrating the detector coil, phantom, actuator coil for two different view angles. The actuator's rotation under B_0 field while sinusoidal current is applied to the actuator coil is depicted in (b). As the applied current changes its polarity between negative and positive current values sinusoidally, the rotation directions switch between to rotation directions shown by orange and green arrows.

Using the actuator setup shown in Figure 2.1b, MRE experiments were conducted on three spherical flask phantoms with agar-agar powder concentrations of 0.65% (6kPa), 0.75% (7.7kPa) and 0.85% (10kPa), hence three phantoms had different shear moduli. Same methods with the back rotation experiments were followed, except that the actuator system was different.

2.2.2 Human Brain Simulations and Experiments

For the M.Sc.'s thesis work, MRE simulations were performed on a brain model, which is pre-segmented into scalp, skull, gray matter (GM), white matter (WM) and cerebrospinal fluid (CSF), using COMSOL Multiphysics (COMSOL, Stockholm, Sweden) [15, 18].

Performing eigenfrequency simulations and frequency response simulations, it was demonstrated that modes of the brain can be excited by conventional actuator systems exciting nodding, naying and head bobble motions of the head.

In the volunteer experiments, it was observed that falx cerebri (FC) significantly affects propagation of shear waves in the brain, hence it was decided to include falx cerebri in the brain model as well and repeat frequency response simulations.

Young's modulus, density, Poisson's ratio and stiffness damping parameters were assigned to the segmented tissues. Assigned material parameters are given in Table 2.1. In Figure 2.6, Young's modulus maps for transverse slices are depicted.

Tissue Name	Young's Modulus(Pa)	Density (kg/m^3)	Poisson's ratio	Stiffness Damping (s)
Scalp	16.7×10^6	1130	0.420	0
Skull	6.5×10^9	1412	0.220	0
CSF	1.2×10^4	1000	0.499	0
GM	1.33×10^4	1040	0.499	2.22×10^{-4}
WM	2.68×10^4	1040	0.499	2.93×10^{-4}
FC	3.15×10^7	1040	0.499	2.55×10^{-4}

Table 2.1: Material properties of the segmented parts of the brain

The brain model was excited in nodding, naying and head bobble motions of the head as depicted in Figure 2.7. The excitation frequency was swept from 20 to 50 Hz with 1 Hz increments. Total displacements with respect to excitation frequency are shown in the Figure 2.17 for nodding, naying and head bobble motion of the brain model. Note that total displacements are plotted for volume

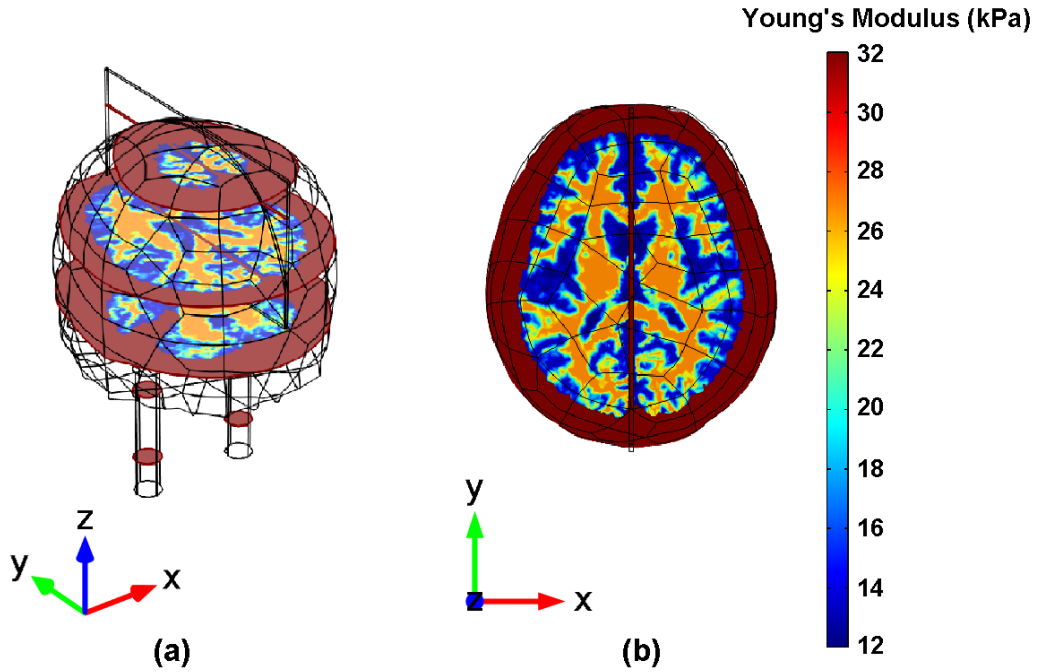


Figure 2.6: Young's modulus maps for (a) three transverse slices (b) the central transverse slice

maximum and input displacement for excitation is 20 μm.

All MRI experiments were conducted in a 3 Tesla Siemens Tim Trio scanner. Human experiments were conducted on healthy volunteers, with permission from local board of ethics. In brain MRE experiments, bite actuator was used to induce shear waves into the brain.

In the M.Sc. thesis [15], a GRE pulse with MEG was used for MRE experiments. Then, to reduce scan time, an SE-EPI pulse was developed for MRE experiments by adding zeroth and first moment nulled MEG. Scan time was accelerated by approximately 30 times compared to GRE pulse that was previously used. As an example, diagram for SE-EPI sequence with MEG is shown in Figure 2.8 for 5 transversal slices each having 5 mm thickness, 64x48 pixels, FOV = 300x225 mm, MEG in three directions. There are 25 preparation scans without any data acquisition. Number of scans is 10 in each MEG direction because 5 slices were images and 2 measurements were made by switching polarity of MEG. Motion encoded phase difference images were computed by subtracting

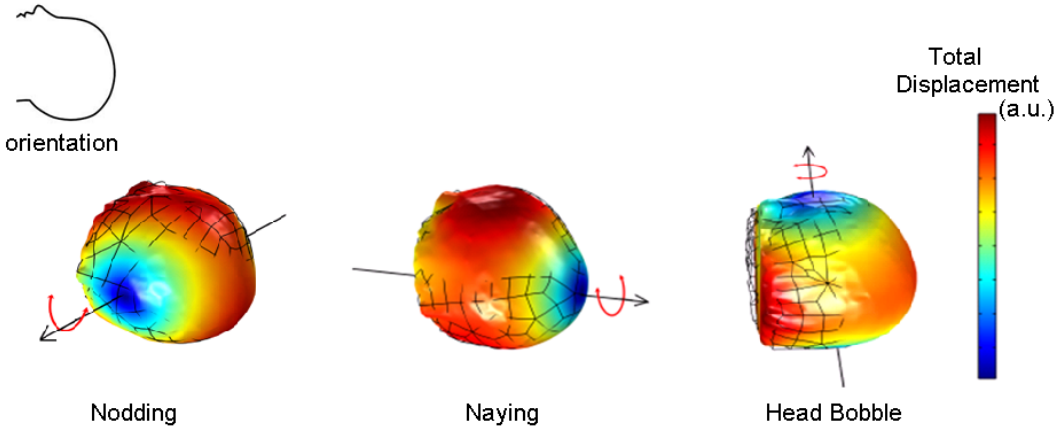


Figure 2.7: Total displacement ($\sqrt{x^2+y^2+z^2}$) measured on the surface of the head for three motion directions. Orientation of the head is given on the upper left corner. Note that colorbar scale is in arbitrary units (a.u.).

two phase images obtained from interleaved sequence having opposite polarity of MEG. Total duration for sequence shown in Figure 2.8 is 6.8 s.

Furthermore, sub-pixel shift correction is used for k-space data in order to avoid N/2 ghost artifacts in phase encoding direction caused by delay between gradient and readout, for SE-EPI sequence.

As an example, photo for volunteer experiment demonstrating bite actuator is shown in Figure 2.18. For volunteer experiments, a bite actuator has been implemented. Except the coil and bite bar parts, the actuator was 3D printed.

Shear wave displacements in z-direction (head-foot direction) are depicted for eight phase offsets at an excitation frequency of 40 Hz in Figure 2.19. Displacements in x- and y- directions are given in Figures 2.20- 2.21, respectively. Amplitudes of shear wave displacements are significantly higher in x- and z-directions compared to y-direction, which is expected since bite actuator vibrates the head similar to the head bobble.

For frequency response analysis of the brain, excitation frequency was swept with 1 Hz increments in the range of 20-40 Hz.

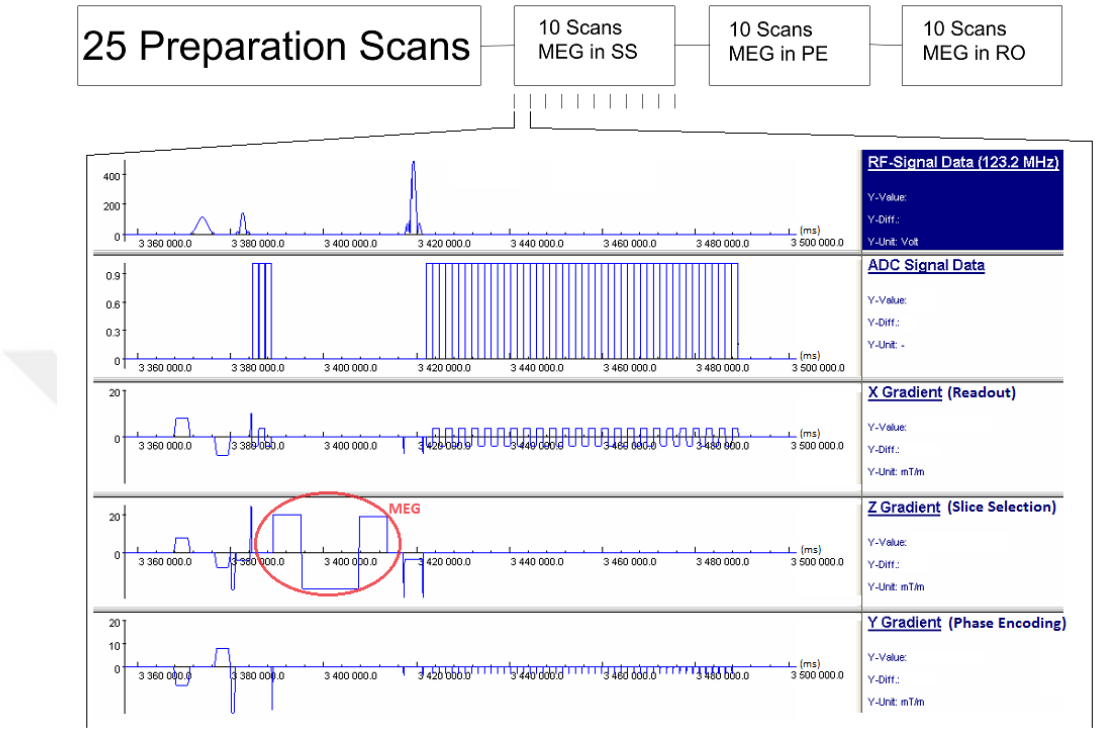


Figure 2.8: EPI-SE sequence with MEG used in the brain experiments

2.3 Results

2.3.1 Phantom Simulations and Experiments

The frequency domain analysis results for two different excitation types are given in Figure 2.9. For the back rotation, volume maximum of displacement in each direction and total displacement are shown in the top figure, where total displacement is defined as $\sqrt{x^2 + y^2 + z^2}$. For the center rotation, volume maximum displacement plots are shown in the bottom figure. Note that displacement in x, y and total displacement plots are the same for each case, hence only displacement in y direction (green curve) is visible. Displacement in z direction is almost zero as expected. There is a slight difference between results of back rotation and center rotation, and mode frequencies for each phantom are almost the same for two cases.

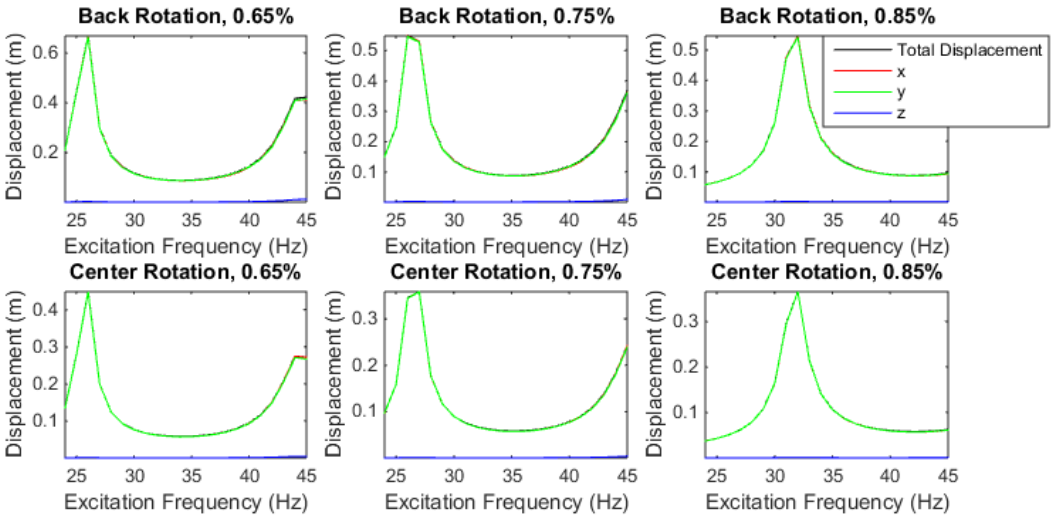


Figure 2.9: Measured displacements for the simulated MRE for three spherical flask phantoms having different Young's Moduli and two types of excitation

To demonstrate an example, results for measurements of shear wave displacement in the phantom with 0.85% agar-agar concentration, induced voltage on detector coil, computed displacement of actuator and normalized shear wave displacement are shown in Figure 2.10. The displacement ratio images are depicted in Figure 2.11.

In Figure 2.12, normalized displacement plots for all phantoms are depicted. Peak displacements are observed at mode frequencies, which were found to be 27.5, 29.5 and 34 Hz for 0.65%, 0.75% and 0.85%, respectively. Thus, a relation between stiffness and mode frequency has been observed. It is demonstrated that 10-20 times greater shear wave displacement than applied displacement by the actuator can be obtained at resonance.

According to Figure 2.13- 2.15, mode frequencies of phantoms with agar-agar concentrations 0.65%, 0.75% and 0.85% are found to be 31, 33.5 and 39 Hz, respectively, for center rotation. In contrast, mode frequencies are found to be 27.5, 29.5 and 34 Hz, respectively, for back rotation. In addition, displacement in phantom is noisy version of applied displacement. Hence, only noise is observed in displacement ratio plots for Figure 2.13- 2.15. The frequency response of the shear wave displacement measured in the phantom and actuator are the same.

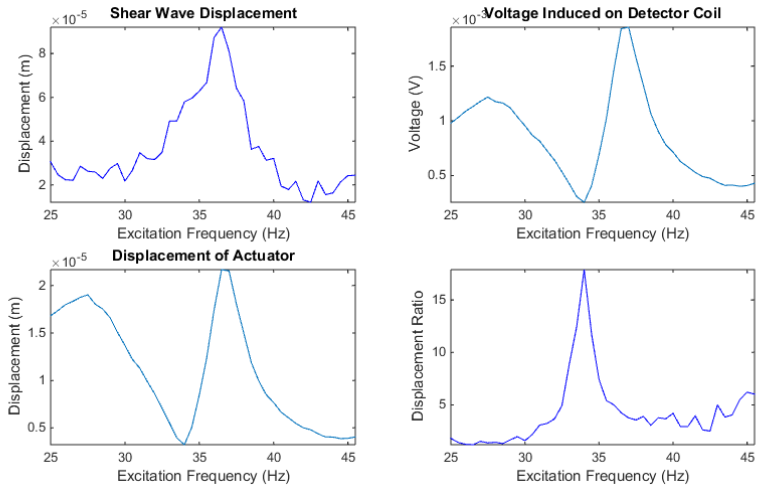


Figure 2.10: Results for back rotation experiment, conducted on phantom with agar-agar concentration of 0.85%. Peak shear wave displacement in phantom, induced voltage on the detector coil, peak displacement of the actuator computed from measured induced voltage on the detector coil, displacement ratio obtained by dividing displacement in the phantom by applied displacement, with respect to excitation frequency

Consequently, only measuring frequency response of the actuator is enough to analyze modes of the phantom for this actuation system.

First three modes of agar-agar phantom with concentration 0.65% are found to be 31, 50.5 and 69 Hz, respectively. Displacement RSS images for each excitation frequency are demonstrated in Figure 2.16.

2.3.2 Human Brain Simulations and Experiments

As depicted in Figure 2.17, peak displacement was observed at 35 Hz for nodding. For naying, the peak displacements were observed at 27 and 45 Hz. For head bobble, the peak displacements were observed around 28 and 30 Hz. Peak displacements were measured as 300-400 μm approximately, thus 15-20 times of the applied displacements were observed at the mode frequencies.

Including falx cerebri, high shear wave displacements can be still observed at

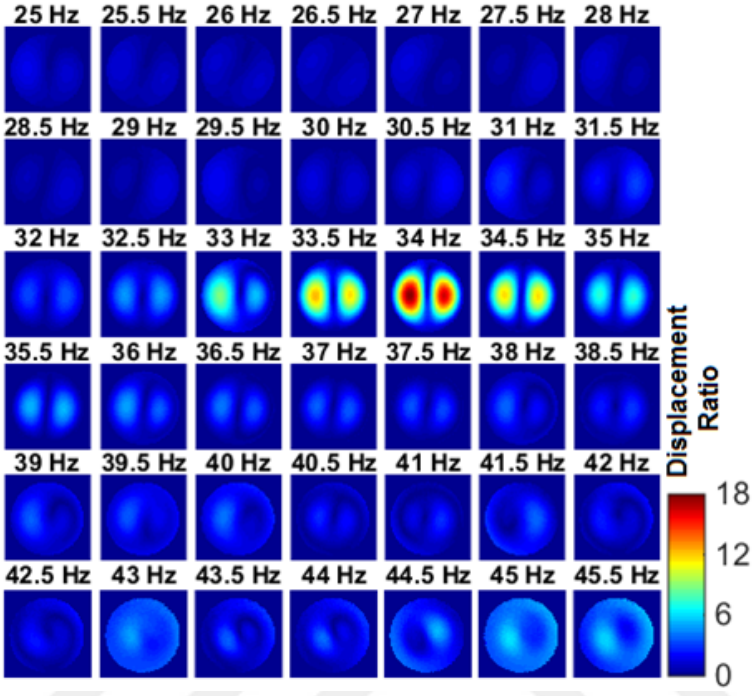


Figure 2.11: Displacement ratio images for each excitation frequency for the same experiment shown in Figure 2.10. Mode frequency is 34 Hz since maximum displacement ratio is observed.

mode frequencies. However, mode frequencies changed compared to the brain model without falx cerebri [15, 18], as expected.

For three volunteer experiments maximum total displacements measured in the brain, displacements of the actuator and displacement ratios with respect to excitation frequency are depicted in Figure 2.22.

2.4 Discussion and Conclusion

In this study, it has been demonstrated that 10-20 times greater shear wave displacement than applied displacement by the actuator can be observed at resonance, validated by phantom simulations, experiments, and the brain simulations. However, further investigation is required to validate modes of shear waves by in-vivo brain experiments.

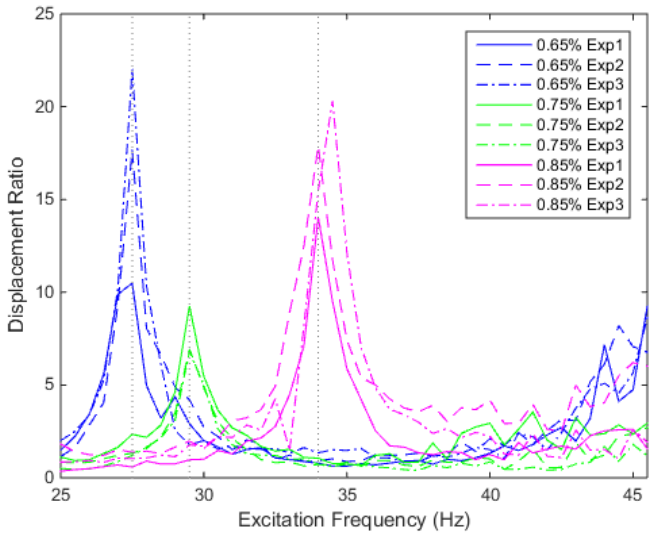


Figure 2.12: Experimental results for displacement ratio versus frequency plots for three phantoms, each repeated three times. Note that mode frequencies are indicated by vertical grids on the plot.

No patterns or peaks are observed in displacement ratio plots for modes of shear waves in Figure 2.22. One of the major problems could be due to measuring the displacement of the actuator which is not exactly the same as measuring the applied displacement. In the experiments of measuring the actuator displacement, detector coil has been used as described previously. By using detector coil attached to the bite actuator, the displacement of the actuator is measured but not amount of displacement applied to the brain. The amount of applied displacement depends on the displacement of the actuator and how much the motion transferred to the head by the mouth guard. Furthermore, it is not possible to know whether the volunteer bites the mouth guard constantly through the whole experiments when the excitation frequency is swept. In addition, measuring the induced voltage on the detector coil is a separate experiment performed inside MRI scanner after the brain MRE scan. Hence, the volunteer might not bite the actuator in the same way than he/she did in the brain MRE scan.

Recently, new methodologies proposed to measure the displacement of the head in the range of micrometers and how the motion transferred into the brain [21,22].

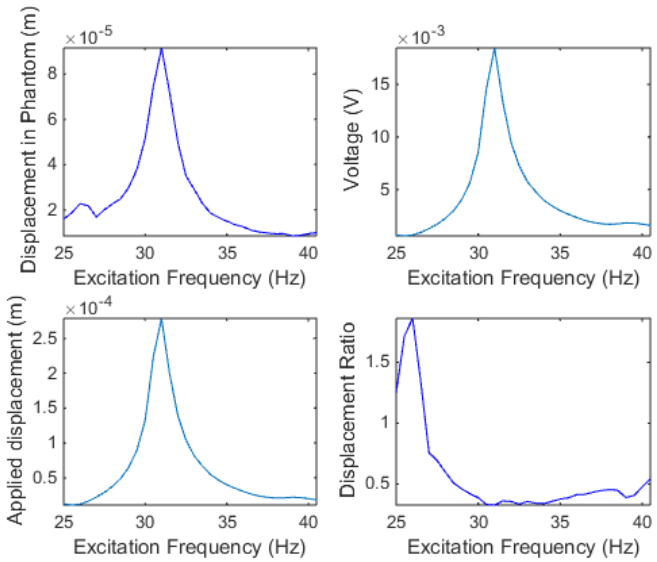


Figure 2.13: Results for center rotation experiment, conducted on phantom with agar-agar concentration of 0.65%. Peak shear wave displacement in phantom, induced voltage on the detector coil, peak displacement of the actuator computed from measured induced voltage on the detector coil, displacement ratio obtained by dividing displacement in the phantom by applied displacement, with respect to excitation frequency

Badachhape et al. [21] measures the motion of the head by attaching three tri-axial accelerometers to the bite bar and uses a pneumatic actuator to induce shear waves into the brain. Although the movement of the head could be directly measured by this methodology, the volunteer should be biting the bite bar constantly. Yin et al. [22] uses dual-saturation and dual-sensitivity motion encoding MRE to measure in-vivo skull–brain motion. This methodology requires separate scans to measure motion of the skull and brain. Hence, it is assumed that the skull-brain motion does not differ between these two scans. Very recently, using distortion-free imaging: a double encoding method (DIADEM), Yin et al. [43] managed to measure fat-water MR elastography simultaneously.

Moreover, in human brain experiments, only head bobble excitation was used but nodding or naying excitation has not been performed due to unavailability of necessary actuators in the lab for these excitation modalities.

On the other hand, the brain model used in FEM simulations may lack some

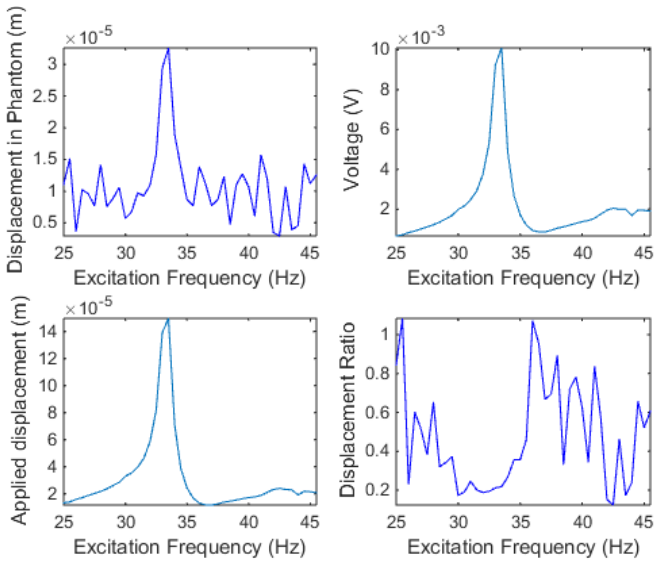


Figure 2.14: Results for center rotation experiment, conducted on phantom with agar-agar concentration of 0.75%. Peak shear wave displacement in phantom, induced voltage on the detector coil, peak displacement of the actuator computed from measured induced voltage on the detector coil, displacement ratio obtained by dividing displacement in the phantom by applied displacement, with respect to excitation frequency

property of in-vivo brain that prevents the formation of modes of shear waves. For instance, it is assumed that the brain is isotropic in terms of elastic properties, which is not accurate [44–47].

In conclusion, high shear wave displacement, 10-20 times of the applied displacement, can be observed at mode frequencies of the tissue during MR elastography. In the brain experiments, modes of shear waves could not have been observed.

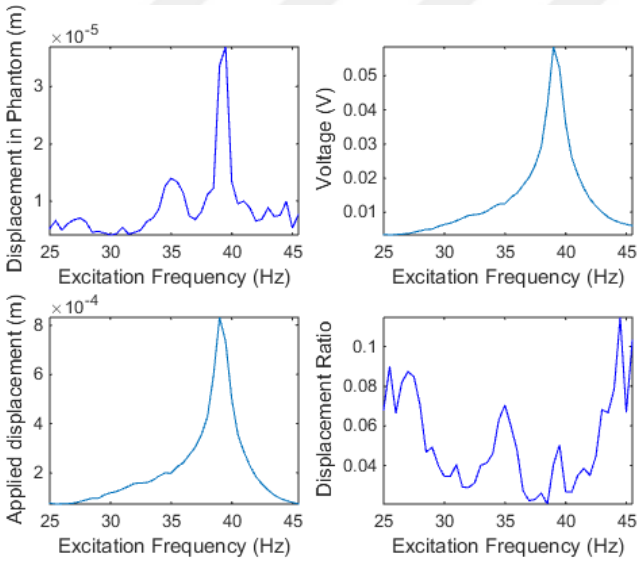


Figure 2.15: Results for center rotation experiment, conducted on phantom with agar-agar concentration of 0.85%. Peak shear wave displacement in phantom, induced voltage on the detector coil, peak displacement of the actuator computed from measured induced voltage on the detector coil, displacement ratio obtained by dividing displacement in the phantom by applied displacement, with respect to excitation frequency

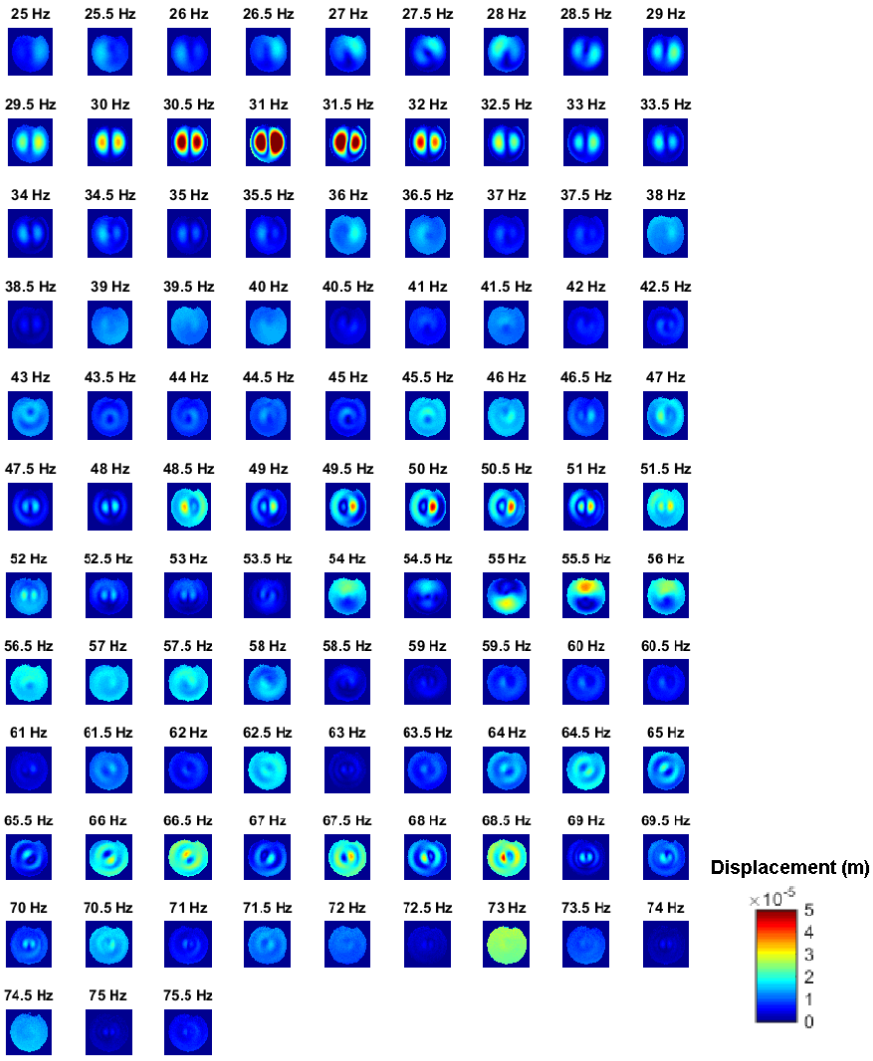


Figure 2.16: Displacement ratio images for each excitation frequency for the same experiment shown in Figure 2.13. Mode frequency is 31.5 Hz since maximum displacement ratio is observed.

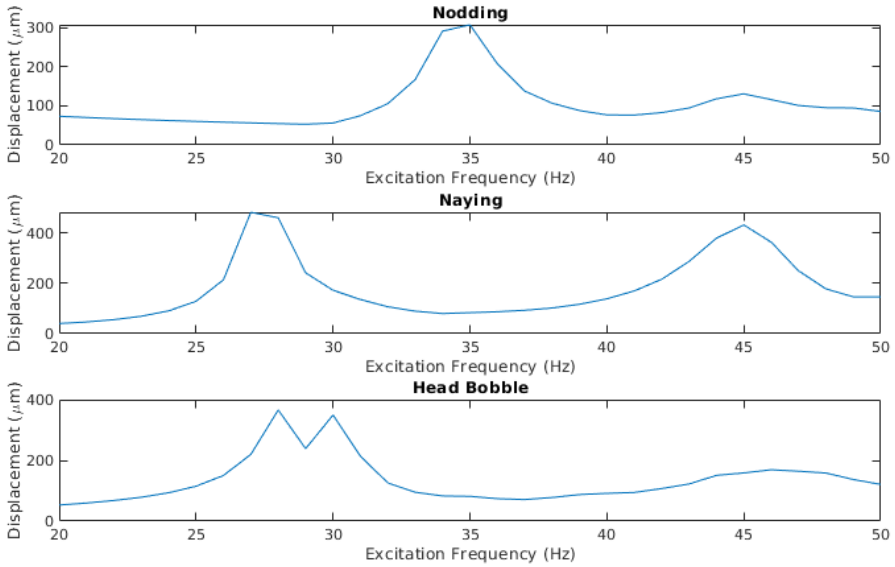


Figure 2.17: Frequency response analysis of the brain model by sweeping excitation frequency for three motions of the head.

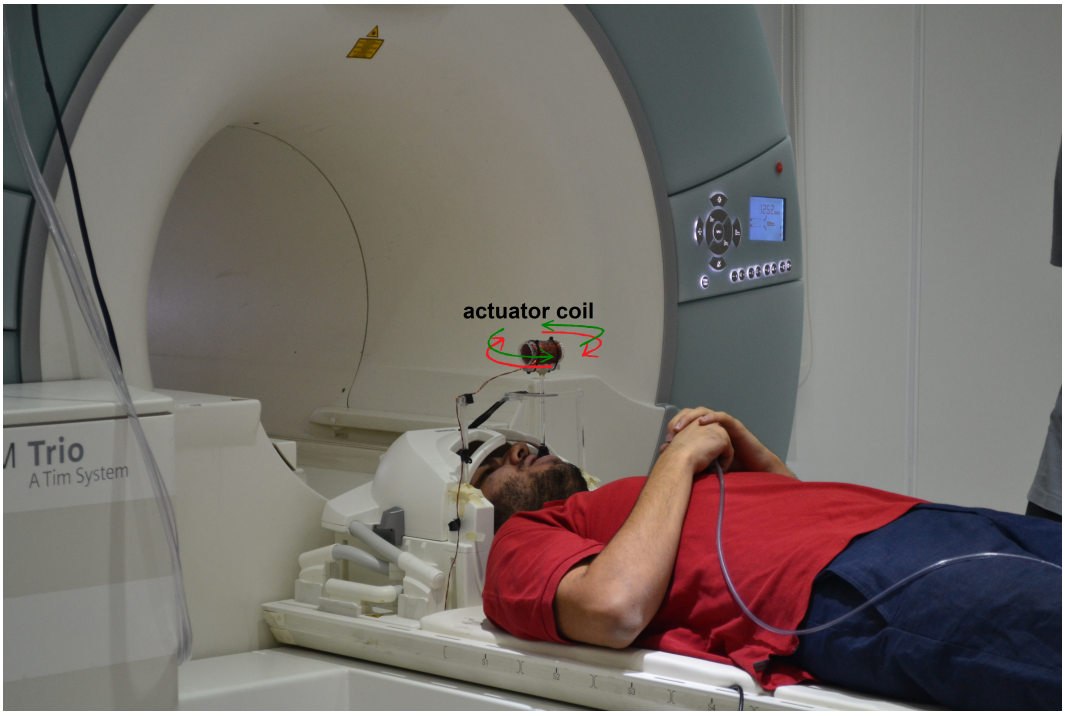


Figure 2.18: Photo showing the bite actuator used in the volunteer experiments

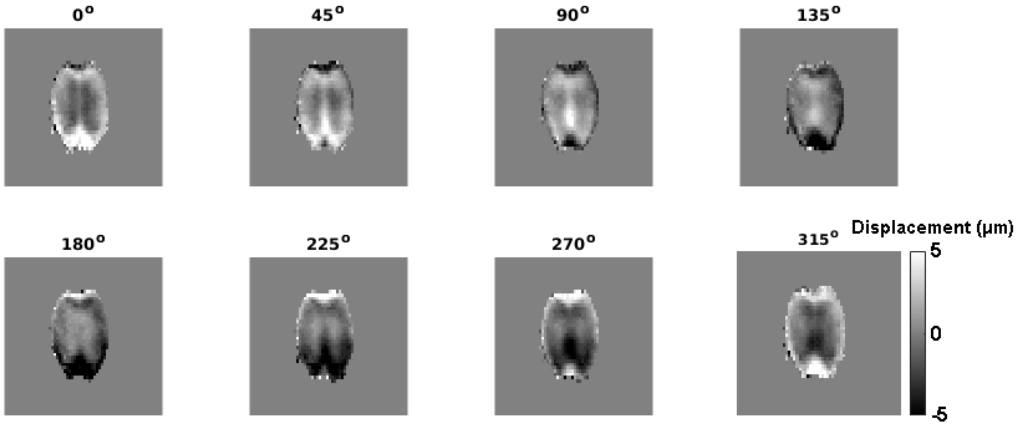


Figure 2.19: Images demonstrating displacement encoded in z-direction acquired for eight phase offsets

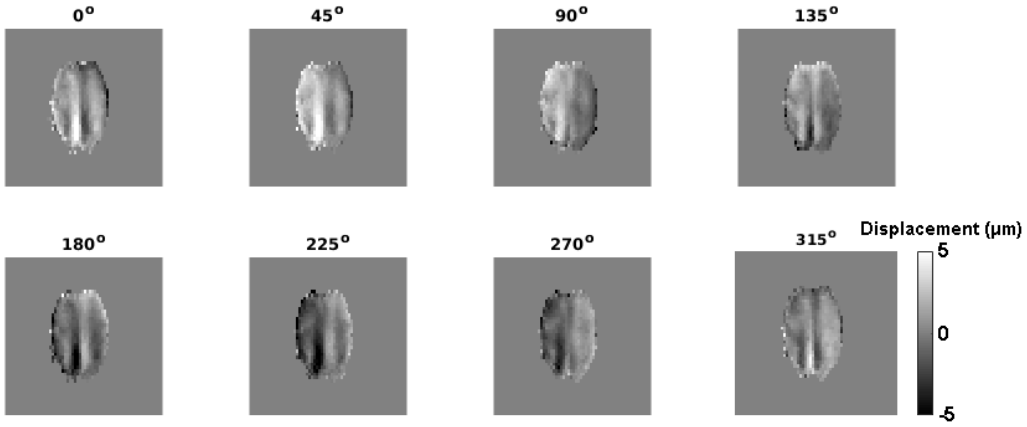


Figure 2.20: Images demonstrating displacement encoded in x-direction acquired for eight phase offsets

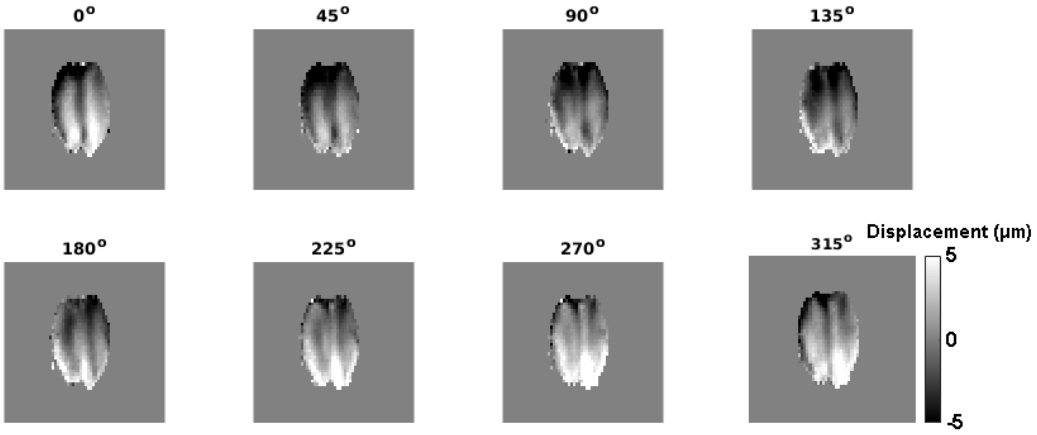
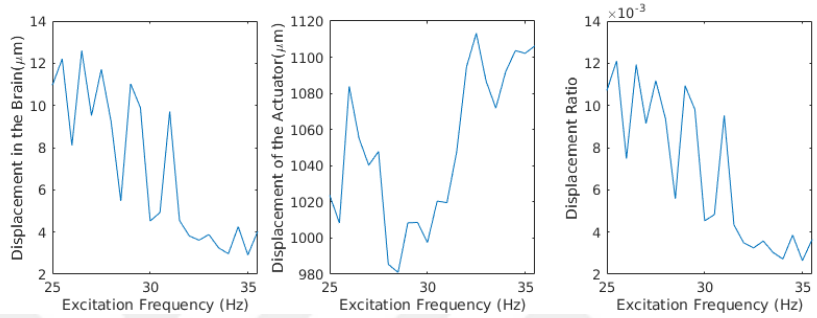
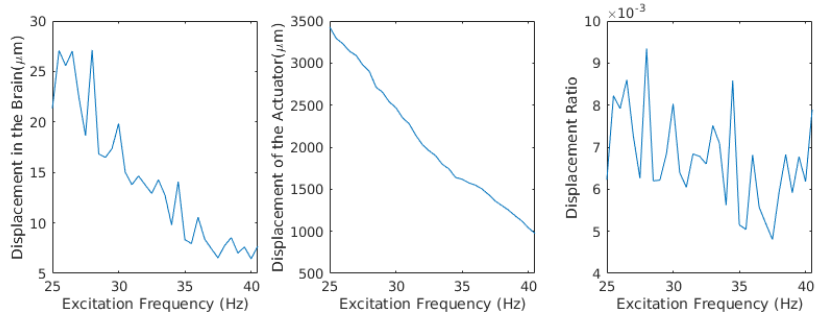


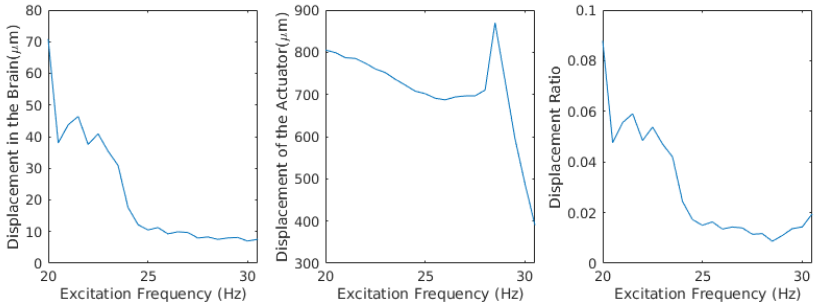
Figure 2.21: Images demonstrating displacement encoded in y-direction acquired for eight phase offsets



(a) Volunteer #1



(b) Volunteer #2



(c) Volunteer #3

Figure 2.22: Maximum total displacement measured in the brain, actuator displacement and displacement ratio with respect to excitation frequencies depicted for three volunteer experiments

Chapter 3

SNR Weighting for Shear Wave Speed Reconstruction in Tomoelastography

3.1 Introduction

Magnetic resonance elastography (MRE) is a noninvasive technique to measure the mechanical properties of tissues for detecting elasticity alterations due to a pathological state [1]. In MRE, shear waves are induced into the tissue by periodic sinusoidal displacement using a mechanical actuator. Using the shear wave displacement information obtained by the motion encoded phase difference images, the elastography map is reconstructed. There are a number of reconstruction techniques for generating elastography maps from shear wave displacement data [25–35].

Tomoelastography [32], also known as k-MDEV, reconstruction has been shown to be quite successful for the liver, spleen, and mouse brain [48]. Moreover, tomoelastography is a multifrequency MRE technique (MMRE), in which

MR elastography data are collected and processed for multiple excitation frequencies to generate the elasticity map. With single frequency excitation, amplitude nulls of the shear wave displacement can be observed in some regions of the tissue being imaged, which may result in an inaccurate estimation of the elasticity of that region [31,32]. Fortunately, using MMRE, the error due to low elastic strain in one frequency at a given location is compensated for by high elastic strain in another frequency. Consequently, the influence of the amplitude nulls on the elastogram is reduced. Here, it should be emphasized that in multifrequency inversion techniques, the frequency dependence of the wave speed (or complex shear modulus) [49, 50] is ignored, and its value is averaged in the range of examined excitation frequencies along with direction components [30, 32].

In tomoelastography, the wave speed distribution in the body is computed for each of the directions and frequencies. Then, the computed wave speed distributions are weighted averaged with the fourth power of amplitude of the displacement in each direction and frequency. This amplitude weighting allows only the wave speed distributions that are computed from waves with amplitudes to contribute to the averaging. It should be noted that for single frequency studies, there are similar weighting schemes based essentially on amplitude to combine reconstructions from multiple directions [28, 51].

The type of weighting can and should be designed according to which elastography map feature is desired to be optimized. One idea can be combining multi-inversion results in a way that will yield the elastogram with the maximum possible signal-to-noise ratio (SNR) [37]. This aim can be achieved by combining multi-inversion results by weighting with the SNR of the wave speed maps obtained for different directions and frequencies.

To use SNR weighting, SNR distributions of individual wave speed maps for each of the directions and frequencies are required. SNR of the wave-speed maps cannot be estimated directly from the wave-speed maps because of the nonlinear operations in the tomoelastography inversion technique. However, considering the noise on the complex MRI signal, the SNR of the reconstructed elasticity

map can be formulated analytically. The findings can be beneficial for combining multidirectional, multifrequency MRE data to obtain high-quality elasticity maps. Unfortunately, there are only a few studies on the SNR in MR elastography (MRE) [36,52], which are designed to understand the quality of the acquired data. Moreover, the SNR of the elasticity map has not yet been investigated. There are acquisition techniques developed for increasing the SNR of the recorded MR data, as proposed in Johnson et al. [39] and summarised in Guenthner et al. [40].

In this study, the SNR of wave speed maps obtained with tomoelastography inversion is analyzed by analytically deriving the SNR at each step of the algorithm, with the assumption of a high SNR. Then, the minimum SNR value that the analytical derivation holds for is determined by Monte Carlo simulations (MCSs). Later, optimum weights to maximize the SNR of the wave speed map are determined. For comparison, the original weighting in tomoelastography, i.e., amplitude weighting, is also implemented. These two weighting schemes are evaluated in terms of three quality metrics, namely, estimation accuracy, SNR, and spatial resolution of the reconstructed wave speed maps. The simulation and experimental results for phantoms and a healthy human abdomen are provided.

3.2 Theory

In the multifrequency MRE technique, displacement fields of the tissues, u, are recorded by the aid of a dedicated MRI pulse sequence in each of the three Cartesian coordinates (index m) for different vibration frequencies (index n). This information is used for estimating elasticity distribution in the tissue of interest. Since in the body, the density of the tissue, ρ_0, is relatively constant and the shear modulus, μ, is related to the wave speed, c, by $\mu = c^2\rho_0$, while neglecting the viscous damping, the wave speed map can also be viewed as the elasticity map of the body [53]. Thus, in the tomoelastography technique, as a wave speed distribution of the tissue, $c(\vec{r})$ is reconstructed and reported as one form of elasticity distribution assuming local homogeneity of the medium.

Considering the sum of plane waves in a local area, the displacement of the isochromat at position $\vec{r}$ can be expressed as:

$$u_{mn}(\vec{r}) = \sum_{l} u_{lmn}(\vec{r}). \tag{3.1}$$

Here, $\vec{r} = [x \quad y]^T$ is the 2D position vector because implementation of tomoelastography is entirely slice-wise [32], hence wave speed map for each slice is reconstructed separately. u_{lmn} represents a plane wave due to the actuator vibrating at frequency ω_n, recorded for the motion encoding direction, m (m =1,2 and 3 correspond to the x, y and z-directions, respectively), and in the propagation direction, l. Each of these plane waves can be written in phasor form as:

$$u_{lmn}(\vec{r}) = u_{0lmn}(\vec{r}) \exp\left(i(\vec{k}_{lmn}(\vec{r}) \cdot \vec{r} + \phi_{lmn}(\vec{r}))\right), \tag{3.2}$$

where u_0 is the amplitude and ϕ is the phase of the plane wave.

Wavenumber $\vec{k}_{lmn}(\vec{r})$ is a 2D vector at the spatial position $\vec{r}$. Its amplitude, $\|\vec{k}_{lmn}(\vec{r})\| = k_{lmn}(\vec{r})$, is equal to $\omega_n / c_{lmn}(\vec{r})$, where $c_{lmn}(\vec{r})$ is the wave speed. Note that $\vec{k}_{lmn}(\vec{r})$ can be defined as a complex vector when considering the viscous damping.

The block diagram demonstrating the steps of tomoelastography inversion is depicted in Figure 3.1, and the details of the algorithm are explained in Tzschatzsch et al. [32].

As illustrated in the diagram, the input to this reconstruction technique is the amplitude-normalized complex-difference MRI signal $\exp(i\theta_{mn}(\vec{r}, t))$. The first step is smoothing the complex signal by a 2D Gaussian kernel, $h_{GK}(\vec{r})$, constructed in the image domain, followed by Laplacian based unwrapping [17] and harmonic selection using discrete Fourier transform (DFT) with N_t-points, which is equivalently the number of phase offsets acquired in the MRE experiment. To decompose superposed plane waves into plane waves propagating in different directions, directional filtering, $Z_l(\vec{k})$, is used. Directional filters are constructed in k-space, where $\vec{k} = [k_x \quad k_y]^T$ and k_x and k_y are the principal axes. Wavenumbers are obtained by computing the L_2-norm of the in-plane gradients of normalized

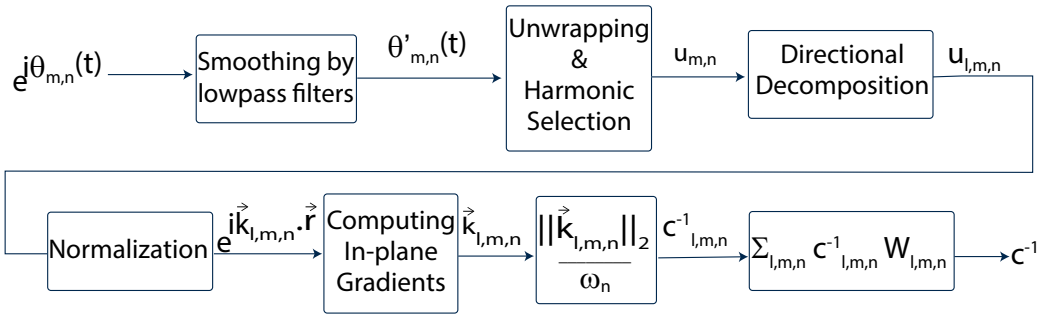


Figure 3.1: Block diagram of the original tomoelastography reconstruction. Amplitude-normalized complex-difference MRE images are the inputs of the reconstruction. In the last step of the reconstruction, weighted averaging is used to combine multiple estimations of the wave speed maps. The weights, W_{lmn}, in the original tomoelastography inversion are $\hat{u}^4_{0lmn}$.

displacement. Dividing the wavenumber by ω_n yields the inverse of the wave speed, $\hat{c}^{-1}$. In the final step, estimates of the inverse of wave speed for each wave direction (l), measurement direction (m), and frequency (n) as $\hat{c}^{-1}_{lmn}$ are combined using weighted summation as follows:

$$\hat{c}^{-1}(\vec{r}) = \sum_{lmn} \hat{c}^{-1}_{lmn}(\vec{r}) W_{lmn}(\vec{r}), \tag{3.3}$$

where

$$\hat{c}^{-1}_{lmn}(\vec{r}) = \frac{\hat{k}_{lmn}(\vec{r})}{\omega_n}. \tag{3.4}$$

Here, the hat symbol ($\hat{}$) indicates estimated values and that they are prone to errors due to incorrect measurements or approximations used in the mentioned algorithm.

In the original tomoelastography reconstruction technique [32], the multiple wave speed estimations, $\hat{c}_{lmn}$, are weight-averaged using:

$$W_{lmn}(\vec{r}) = \frac{\hat{u}^4_{0lmn}(r)}{\sum_{lmn} \hat{u}^4_{0lmn}(r)}. \tag{3.5}$$

In this method, using the fourth power of the local amplitude of the plane wave ensures that only wavenumbers constructed from high wave amplitudes will be averaged to compute the wave speed map.

The alternative technique proposed here is SNR weighting. It can be shown that to maximize the SNR of the wave speed estimation, the square of individual SNRs of $\hat{c}_{lmn}^{-1}$, ${}^{c}\Psi_{lmn}$, should be used [54]. Here, it is assumed that the primary noise source on a complex MRI signal is thermal and modeled as additive white Gaussian noise (AWGN). With the high SNR assumption, the noise probability distribution remains Gaussian despite some nonlinear operations in the wave speed reconstruction algorithm. Thus, the mean and standard deviation (SD) of the noise probability distribution can be derived analytically from the tomoelastography inversion.

The actual complex-difference MRI signal is $S_{mn}(\vec{r},t) = A_{mn}(\vec{r})\exp(i\theta_{mn}(\vec{r},t))$, obtained from two measurements with opposite motion encoding gradient (MEG) polarity, where A is the magnitude and θ is the phase of the noiseless complex signal. The primary noise source on a complex MRI signal is thermal and is modeled as additive white Gaussian noise (AWGN), and the same applies to a complex-difference MRI signal [55]; hence, let the measured complex-difference MRI signal be denoted as $\hat{S}$ and the SNR of $|\hat{S}|$ be ${}^{i}\Psi$. Complex MR images are reconstructed by taking the 2D Fourier transform of the complex MRI signal.

In MRE, the phase is taken into consideration since motion is encoded in the phase, equivalent to:

$$\theta_{mn}(\vec{r},t) = \sum_{l} u_{0lmn}(\vec{r}) cos\left(\vec{k}_{mn}(\vec{r})\cdot\vec{r} - \omega_n t + \phi_{mn}(\vec{r})\right) \tag{3.6}$$

For a high SNR (i.e. ${}^{i}\Psi >> 1$), noise distribution in the phase can be approximated to be equal to noise distribution in the real or imaginary part of the complex MRI signal, hence expected value (E[]), and standard deviation (SD[]) of the phase are given as:

$$E[\arg\{S_{mn}(\vec{r},t)\}] = \theta_{mn}(\vec{r},t) \tag{3.7}$$

and

$$SD[\arg\{S_{mn}(\vec{r},t)\}] = \frac{1}{{}^{i}\Psi_{mn}(\vec{r})}, \tag{3.8}$$

respectively. Here, arg returns angle of the complex number.

Now, tomoelastography inversion is followed step by step, as described in Tzschatzsch et al. [32]. The first step of the inversion is smoothing the complex signal $\exp(i(\hat{\theta}))$ by lowpass filtering using a 2D Gaussian kernel, $h_{GK}(\vec{r})$, having a standard deviation of $\sigma_{GK} = 0.8$ pixels and size 5×5 pixels, constructed in the image domain as:

$$h_{GK}(\vec{r}) = \frac{\exp(-r^2/2\sigma_{GK}^2)}{\sum_{x=-2}^{2}\sum_{y=-2}^{2}\exp(-r^2/2\sigma_{GK}^2)}, \tag{3.9}$$

which does not alter the mean since it has unit DC gain (i.e., $\sum_{x=-\infty}^{\infty}\sum_{y=-\infty}^{\infty} h_{GK}(\vec{r}) = 1$). Hence, $E[\hat{\theta}'_{mn}(\vec{r},t)] = E[\arg\{S_{mn}(\vec{r},t)\}]$, and the SD of the smoothed phase becomes:

$$SD[\hat{\theta}'_{mn}(\vec{r},t)] = \frac{1}{i\Psi_{mn}(\vec{r})} \underbrace{\sqrt{\sum_{x=-2}^{2}\sum_{y=-2}^{2}(h_{GK}(\vec{r}))^2}}_{\text{Smoothing}} \tag{3.10}$$

It is assumed that the Gaussian kernel Eq. 3.9, used in smoothing, is a very light filter, which has an effect only on the noise characteristics. Additionally, $A_{mn}(\vec{r})$ is assumed to be locally homogeneous, which is not true at the edges of the tissue.

Smoothing is followed by unwrapping and harmonic frequency selection:

$$\begin{aligned} &E[Re\{\hat{u}_{mn}(\vec{r})\}] \\ &\quad = \sum_{l} u_{0lmn}(\vec{r}) \underbrace{\frac{N_t}{2} Re\{\exp(-i(\vec{k}_{mn}(\vec{r})\cdot\vec{r} + \phi_{mn}(\vec{r})))\}}_{\substack{\text{Harmonic}\\ \text{Frequency}\\ \text{Selection}}} \end{aligned} \tag{3.11}$$

$$\begin{aligned} &E[Im\{\hat{u}_{mn}(\vec{r})\}] \\ &\quad = \sum_{l} u_{0lmn}(\vec{r}) \underbrace{\frac{N_t}{2} Im\{\exp(-i(\vec{k}_{mn}(\vec{r})\cdot\vec{r} + \phi_{mn}(\vec{r})))\}}_{\substack{\text{Harmonic}\\ \text{Frequency}\\ \text{Selection}}} \end{aligned} \tag{3.12}$$

$$SD[Re\{\hat{u}_{mn}(\vec{r})\}] = SD[Im\{\hat{u}_{mn}(\vec{r})\}]$$
$$= \frac{1}{{}^{i}\Psi_{mn}(\vec{r})} \underbrace{\sqrt{\frac{N_t}{2}}}_{\substack{\text{Harmonic}\\ \text{Frequency}\\ \text{Selection}}} \underbrace{\sqrt{\sum_{x=-2}^{2}\sum_{y=-2}^{2}(h_{GK}(\vec{r}))^2}}_{\text{Smoothing}} \tag{3.13}$$

where N_t is the number of discrete Fourier transform (DFT) points used in harmonic frequency selection, equivalently, the number of phase offsets. Note that for a high SNR, the effect of unwrapping on the SNR is absent. The unwrapping algorithm is Laplacian based [17].

Then, directional filtering by $Z_l(\vec{k})$ takes place, which is given as:

$$Z_l(\vec{k}) = \beta(\vec{k}) \exp\Big(- \frac{\big(\arg\{\vec{k}\} - \phi_{Z_l}\big)^2}{2\sigma_Z^2}\Big), \tag{3.14}$$

where

$$\beta(\vec{k}) = \frac{1}{1 + \big(\frac{k}{k_{up}}\big)^{2N}} - \frac{1}{1 + \big(\frac{k}{k_{low}}\big)^{2N}}. \tag{3.15}$$

and $\sigma_Z = 2\pi/N_l$. In equation Eq. 3.14, arg returns angle of the vector. Note that ϕ_{Z_l} is the direction of the lth directional filter, N_l is the number of directional filters, N is the filter order, and k_{low} and k_{up} are lower and upper cut-off values in the k-space, respectively. In the simulations and experiments the directional filter parameters are selected as: N=10, $k_{low} = 0.02\Delta^{-1}$ and $k_{up} = 0.5\Delta^{-1}$, where Δ is the in-plane voxel size, which is assumed to be isotropic here. After the directional filtering, the statistics of the noise become:

$$E[Re\{\hat{u}_{lmn}(\vec{r})\}] = u_{0lmn}(\vec{r}) \underbrace{\frac{N_t}{2} Re\{\exp(-i(\vec{k}_{lmn}(\vec{r})\cdot\vec{r} + \phi_{lmn}(\vec{r})))\}}_{\substack{\text{Harmonic}\\ \text{Frequency}\\ \text{Selection}}} \underbrace{Z_l(\vec{k}_{lmn})}_{\substack{\text{Directional}\\ \text{Filter}}} \tag{3.16}$$

$$E[Im\{\hat{u}_{lmn}(\vec{r})\}] = u_{0lmn}(\vec{r}) \underbrace{\frac{N_t}{2} Im\{\exp(-i(\vec{k}_{lmn}(\vec{r})\cdot\vec{r} + \phi_{lmn}(\vec{r})))\}}_{\substack{\text{Harmonic}\\ \text{Frequency}\\ \text{Selection}}} \underbrace{Z_l(\vec{k}_{lmn})}_{\substack{\text{Directional}\\ \text{Filter}}}, \tag{3.17}$$

$$SD[Re\{\hat{u}_{lmn}(\vec{r})\}] = SD[Im\{\hat{u}_{lmn}(\vec{r})\}] = \frac{1}{{}^{i}\Psi_{mn}(\vec{r})} \underbrace{\sqrt{\frac{N_t}{2}}}_{\substack{\text{Harmonic}\\ \text{Frequency}\\ \text{Selection}}} \underbrace{\alpha}_{\substack{\text{Smoothing}\\ \text{and}\\ \text{Directional}\\ \text{Filter}}} \tag{3.18}$$

where $Z_l(\vec{k}_{lmn})$ is the response of the lth directional filter at $\vec{k}_{lmn}$ and α is given as:

$$\alpha = \sqrt{\sum_{x=-N_x/2}^{N_x/2-1} \sum_{y=-N_y/2}^{N_y/2-1} \left(h_{GK}(\vec{r}) * *\zeta_l(\vec{r})\right)^2}, \tag{3.19}$$

where $\zeta_l(\vec{r}) = F_{2D}^{-1}\{Z_l(\vec{k})\}$, and $**$ is the 2D convolution operator.

Here, it is assumed that $Z_l(\vec{k}_{lmn}) = 1$ if the $\mathrm{l}^t h$ direction is the propagation direction of the plane wave, which may not always be true but is very close to 1 for most of the cases; otherwise, it is zero. Thus, the term $Z_l(\vec{k}_{lmn})$ is dropped for the rest of the derivation. Therefore, the magnitude of SNR of directionally filtered displacement in the direction of the plane wave propagation, ${}^{u}\Psi$, can be expressed as:

$${}^{u}\Psi_{lmn}(\vec{r}) = {}^{i}\Psi_{mn}(\vec{r}) \frac{u_{0lmn}(\vec{r})\sqrt{N_t}}{\sqrt{2}\alpha} \tag{3.20}$$

Then, directionally filtered displacement is normalized by its magnitude $\hat{u}_{lmn}(\vec{r})/|\hat{u}_{lmn}(\vec{r})|$. The expected and SD value of $\exp(i\hat{\vec{k}}_{lmn} \cdot \vec{r})$ is:

$$E[Re\{\hat{u}_{lmn}(\vec{r})/|\hat{u}_{lmn}(\vec{r})|\}] = Re\Big\{ \exp\Big(-i\big(\vec{k}_{lmn}(\vec{r}) \cdot \vec{r} + \phi_{lmn}(\vec{r})\big)\Big)\Big\} \tag{3.21}$$

$$E[Im\{\hat{u}_{lmn}(\vec{r})/|\hat{u}_{lmn}(\vec{r})|\}] = Im\Big\{ \exp\Big(-i\big(\vec{k}_{lmn}(\vec{r}) \cdot \vec{r} + \phi_{lmn}(\vec{r})\big)\Big)\Big\} \tag{3.22}$$

$$SD[Re\{\hat{u}_{lmn}(\vec{r})/|\hat{u}_{lmn}(\vec{r})|\}]$$
$$= \frac{1}{{}^{i}\Psi_{mn}(\vec{r})} \underbrace{\sqrt{\frac{N_t}{2}}}_{\substack{\text{Harmonic}\\ \text{Frequency}\\ \text{Selection}}} \underbrace{\alpha}_{\substack{\text{Smoothing}\\ \text{and}\\ \text{Directional}\\ \text{Filter}}} \underbrace{\frac{2|Re\{i\exp(-i(\vec{k}_{lmn}(\vec{r}) \cdot \vec{r} + \phi_{lmn}(\vec{r})))\}|}{N_t u_{0lmn}}}_{\text{Normalization}} \tag{3.23}$$

$$SD[Im\{\hat{u}_{lmn}(\vec{r})/|\hat{u}_{lmn}(\vec{r})|\}]$$
$$= \frac{1}{{}^{i}\Psi_{mn}(\vec{r})} \underbrace{\sqrt{\frac{N_t}{2}}}_{\substack{\text{Harmonic}\\ \text{Frequency}\\ \text{Selection}}} \underbrace{\alpha}_{\substack{\text{Smoothing}\\ \text{and}\\ \text{Directional}\\ \text{Filter}}} \underbrace{\frac{2|Im\{i\exp(-i(\vec{k}_{lmn}(\vec{r})\cdot\vec{r}+\phi_{lmn}(\vec{r})))\}|}{N_t u_{0lmn}}}_{\text{Normalization}} \tag{3.24}$$

Computing L2-norm of in-plane gradients:

$$\hat{k}_{lmn}(\vec{r}) = \sqrt{\left|\frac{\partial}{\partial x}\frac{\hat{u}_{lmn}(\vec{r})}{|\hat{u}_{lmn}(\vec{r})|}\right|^2 + \left|\frac{\partial}{\partial y}\frac{\hat{u}_{lmn}(\vec{r})}{|\hat{u}_{lmn}(\vec{r})|}\right|^2}, \tag{3.25}$$

and

$$E[\hat{k}_{lmn}(\vec{r})] = \|\vec{k}_{lmn}(\vec{r})\| = k_{lmn}(\vec{r}) \tag{3.26}$$

$$SD[\hat{k}_{lmn}(\vec{r})] = \frac{1}{{}^{i}\Psi_{mn}(\vec{r})} \underbrace{\sqrt{\frac{N_t}{2}}}_{\substack{\text{Harmonic}\\ \text{Frequency}\\ \text{Selection}}} \underbrace{\alpha}_{\substack{\text{Smoothing}\\ \text{and}\\ \text{Directional}\\ \text{Filter}}} \underbrace{\frac{2}{N_t u_{0lmn}(\vec{r})}}_{\text{Normalization}} \underbrace{\frac{1}{\sqrt{2}\Delta}}_{\substack{\text{In-plane}\\ \text{Gradients}}}. \tag{3.27}$$

In the equation above, $\hat{k}_{lmn}$ is the estimate of k_{lmn}.

Hence, the SNR of the wavenumber reconstructed is $SNR_{\hat{k}} = E[\hat{k}_{lmn}]/SD[\hat{k}_{lmn}]$. Then, the inverse of the wave speed is computed $\hat{c}^{-1}_{lmn} = \hat{k}_{lmn}/\omega_n$. Note that $SNR_{\hat{c}^{-1}} = SNR_{\hat{k}}$ because the mean and SD are both scaled by $1/\omega_n$ (i.e., $E[\hat{c}^{-1}] = E[\hat{k}_{lmn}]/\omega_n$ and $SD[\hat{c}^{-1}] = SD[\hat{k}_{lmn}]/\omega_n$), resulting in no change in the SNR. Additionally, using linearization via Taylor series, it can be shown that $SNR_{\hat{c}} = SNR_{\hat{c}^{-1}}$, where $SNR_{\hat{c}}$ is the SNR of $\hat{c}$. Therefore, based on Eqs. 3.26-3.27, $SNR_{\hat{c}}$ is given as:

$${}^{c}\Psi_{lmn}(\vec{r}) = {}^{i}\Psi_{mn}(\vec{r})\frac{\sqrt{N_t}}{\alpha}k_{lmn}(\vec{r})u_{0lmn}(\vec{r})\Delta \tag{3.28}$$

where α is

$$\alpha = \sqrt{\sum_{x=-N_x/2}^{N_x/2-1}\sum_{y=-N_y/2}^{N_y/2-1}\left(h_{GK}(\vec{r}) * *\zeta_l(\vec{r})\right)^2}, \tag{3.29}$$

and ${}^{i}\Psi_{mn}$ is the magnitude image SNR, N_x and N_y are the number of x and y pixels imaged, respectively, Δ is the isotropic in-plane resolution, $**$ is the 2D convolution operator, and $\zeta_l(\vec{r})$ is the 2D inverse Fourier Transform of $Z_l(\vec{k})$.

However, due to the high SNR assumption in the derivation, SNR values at the output of the directional filters, ${}^{u}\Psi_{lmn}$, which do not satisfy the high SNR assumption, are thresholded prior to the weighting step by equating them to zero (i.e., set ${}^{c}\Psi_{lmn} = 0$ if ${}^{u}\Psi_{lmn}(\vec{r}) < {}^{thr}\Psi_{lmn}(\vec{r})$). The SNR threshold, ${}^{thr}\Psi_{lmn}(\vec{r})$, is determined by comparing the results of Monte Carlo computations to the analytical derivations. After thresholding, the SNR-weighted reconstruction weights are chosen as:

$$W_{lmn}(\vec{r}) = \frac{{}^{c}\Psi^2_{lmn}(\vec{r})}{\sum_{lmn} {}^{c}\Psi^2_{lmn}(\vec{r})}, \tag{3.30}$$

where

$${}^{u}\Psi_{lmn}(\vec{r}) = {}^{i}\Psi_{mn}(\vec{r}) \frac{u_{0lmn}(\vec{r})\sqrt{N_t}}{\sqrt{2}\alpha}. \tag{3.31}$$

The required data and parameters to determine ${}^{c}\Psi_{lmn}(\vec{r})$ in Eq. 3.30 are given in Eq. 3.28, which are image SNR ${}^{i}\Psi_{mn}(\vec{r})$,, number of phase offsets N_t, the energy of convolution of Gaussian kernel and the directional filter α, the wavenumber $k_{lmn}(\vec{r})$, the filtered displacement $u_{0lmn}(\vec{r})$ and the in-plane image voxel size Δ .

3.3 Methods

3.3.1 Reconstructions

For wave speed reconstructions, tomoelastography inversion has been implemented for the proposed SNR weighting and the original amplitude weighting schemes, as explained in the previous section. To summarize regarding Eq. 3.3, the original tomoelastography reconstruction uses $\hat{u}^4_{0lmn}$ as weights (i.e., amplitude-weighted as given in Eq. 3.5), and the SNR-weighted reconstruction

uses ${}^{c}\Psi_{lmn}$ (as given in Eq. 3.30). Each SNR value (${}^{u}\Psi$ for each index and pixel) at the output of the direction filter (i.e., ${}^{u}\Psi$) is checked if it is greater than the threshold, which is determined by the minimum SNR (${}^{thr}\Psi$) that analytical derivations hold for. If ${}^{u}\Psi$ exceeds the threshold, the weight is set to the square of the SNR of c^{-1} (${}^{c}\Psi$); otherwise, ${}^{c}\Psi$ is set to zero.

3.3.2 Simulations

MRE simulations are performed on four simulation phantoms (SPs). The displacement data for the first simulation phantom (SP#1) were generated via MATLAB (Burlington, MA, USA), whereas the second (SP#2), third (SP#3) and fourth (SP#4) simulation phantoms were generated via COMSOL Multiphysics (COMSOL, Stockholm, Sweden) finite element method (FEM) software, as depicted in Figure 3.2A. Wave speed maps were reconstructed from the displacement data using MATLAB for all simulation phantoms.

In SP#1, a 2D plane wave simulation was generated in a homogeneous medium at a single frequency using MATLAB. The wave speed was 3.2 m/s, and the excitation frequency was swept from 30 to 72 Hz with 6 Hz increments. The resolution of SP#1 was 1.5 mm isotropic and size of the phantom is 15×15 cm^2, hence 100×100 pixels. Zero padding was used to extend the data to 128×128 pixels, 192×192 mm^2.

SP#2 was a square-shaped phantom with each side 20 cm long, consisting of two media with different wave speeds: 1.9 m/s for $y > 0$ and 2.5 m/s for $y \leq 0$ (with the origin being the center of the phantom). Prescribed sinusoidal displacement with an amplitude of 5 μm in the x-direction was assigned to the top side, and frequency-domain analyses were performed for excitation frequencies of 30 to 72 Hz with 6 Hz increments. Complex displacement data in the x- and y-directions were exported with 1.5 mm isotropic resolution to be processed in MATLAB .

For SP#2, data were read in MATLAB and cropped to the middle 162 $mm \times$

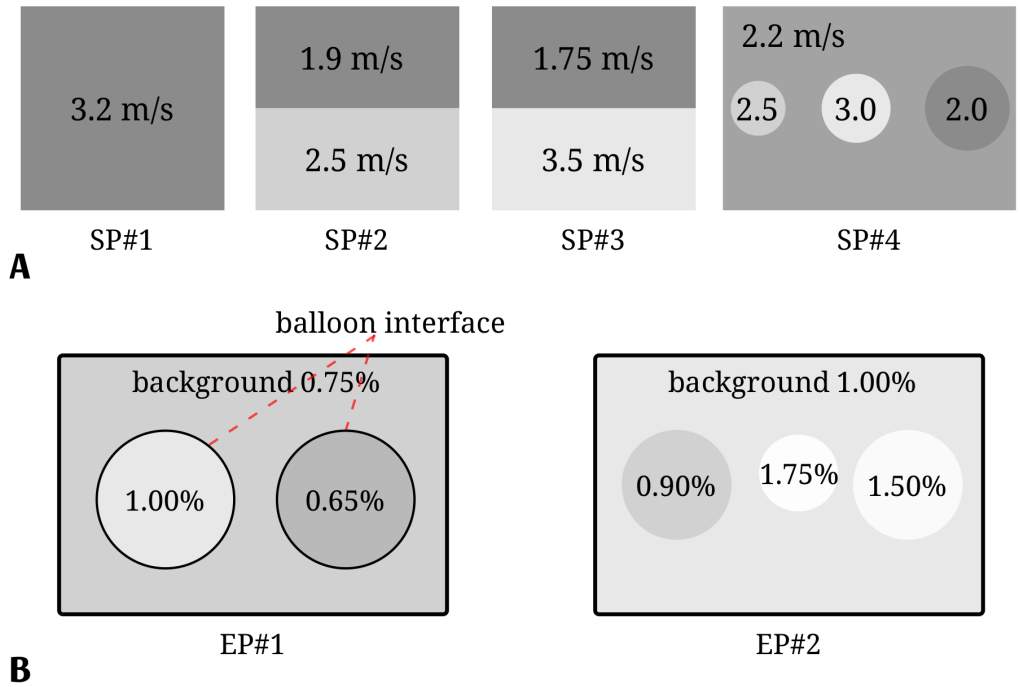


Figure 3.2: (a) Simulation phantoms depicting ground truth values for the real part of their wave speeds. (b) Experimental phantoms showing the agar-agar powder concentrations for the background and inclusions.

162 mm square to decrease the effect of reflected waves in the inversion. Furthermore, zero padding was used to extend the region of interest to 189 $mm \times 189$ mm with the center square, 100 $mm \times 100$ mm, being the phantom.

Additionally, to be convenient and use the same reconstructions used for the experimental data, the displacement fields in z-direction were taken as zero, since in the MRE experiments, the displacement fields are recorded in all three directions.

SP#3 was the same as SP#2 with two media having wave speeds of 1.75 and 3.5 m/s.

SP#4 was 3D, with three inclusions having different sizes and shear wave speeds. The diameters of the inclusions were 1.5, 2.5 and 3.5 cm, having shear wave speeds of 2.5, 3 and 2 m/s, respectively. The dimensions of the phantom were $20 \times 10 \times 8$ cm^3 with resolution 1.5 mm isotropic and the shear wave speed

for the background was 2.2 m/s. The excitation frequency was swept from 30 to 72 Hz with 6 Hz increments.

For SPs#2-4, the Poisson ratio (ν) and density (ρ) were assigned as 0.499 and 1040 kg/m^3, respectively. To account for damping in the models, complex Young's moduli were assigned as $E = 2(1+\nu)\rho c^2 + i0.05(2(1+\nu)\rho c^2)$, where c is the wave speed, as given for each phantom in Figure 3.2A.

Using COMSOL Multiphysics, MRE simulations were conducted on a 3D human abdomen model developed from Austin Man v2.4, with voxel size $2 \times 2 \times 2\ mm^3$ [56]. The Poisson ratio, density and complex Young's moduli were assigned for the segmented tissues obtained from previous studies [32,57–59]. The assigned parameters are given in Table 3.1. Prescribed displacement was assigned to the surface of the anterior abdomen, and frequency domain analyses were performed, sweeping the excitation frequency from 30 to 48 Hz with 6 Hz increments. Complex displacement fields were exported with 2 mm isotropic voxels and then converted to eight phase offset real displacement data. Then, simulated complex MRI signal data were constructed with unit magnitude and eight phase offset real displacement data being the phase to be processed for wave speed map calculations using MATLAB. In addition, to evaluate the performance of the weighting schemes under noise, complex AWGN was added to the simulated complex MRI signal at different SNR levels in a reasonable range for each excitation frequency. The mean SNR level was 20, the minimum was 16 and the maximum was 24. Furthermore, 12 directional filters were employed for all of the data mentioned in this study.

Note that for all of the simulated MRE data when noise is not added, the image SNR ($^i\Psi$) is assumed to be very high so that they cancel out in the normalization of the weighting. Thus, none of the weights are thresholded. However, this is called the no-noise case in this paper since noise is not added, but only a constant high SNR is assigned to the image SNR in Eq. 3.28.

Tissue Name	Density (kg/m^3)	Poisson's ratio	Real Part of the Young's Modulus (kPa)
Colon	1040	0.499	15
Colon Internal	1040	0.499	15
Aorta	1040	0.499	15
Duodenum	1040	0.499	22.7
Blood Vessel	1040	0.499	15
Gall Bladder	1040	0.499	12.5
Cerebro Spinal Fluid	1040	0.499	12
Bone Cortical	1040	0.220	2400
Bone Marrow	1040	0.220	2400
Liver	1040	0.499	8
Peritoneal Cavity	1040	0.499	12.5
Cartilage	1040	0.499	12.5
Lung Inflated	1040	0.430	3
Fat	1040	0.499	9.6
Pancreas	1040	0.499	8
Small Intestine	1040	0.499	22.7
Small Intestine Internal	1040	0.499	22.7
Muscle	1040	0.499	9.6
Diaphragm	1040	0.499	12.5
Spinal Cord	1040	0.499	8
Spleen	1040	0.499	12.5
Nerve	1040	0.499	12.5
Stomach	1040	0.499	22.7
Stomach Internal	1040	0.499	22.7
Skin Dry	1040	0.420	101.2
Distal Convoluted Tubule	1040	0.499	12.5
Tendon	1040	0.499	12.5

Table 3.1: Material properties of the segmented parts of human abdomen

3.3.3 Validation of analytical SNR derivations and performance analyses

To validate the analytically derived SNR equation in Eq. 3.30, MCS was conducted on single excitation frequency data (72 Hz) of SP#1. For a number of trials (N), chosen as 100, AWGN was added to the displacement data, followed by tomoelastography inversion. First, the mean and SD of wave speed maps were computed over N and then averaged over a region of interest (ROI) with size MxM (M=87 pixels). The SNR was obtained by the ratio of the 2D-averaged mean to the SD. In addition, the analytically approximated SNR values were compared with the SNR obtained by MCS. The noise level of AWGN was swept from SNR=0.5 to 10 with an incremental step of 0.1. The minimum SNR value that the high SNR assumption holds ($^{thr}\Psi$) for the analytical approximations was determined. Additionally, to analyze the effect of the assumption of the wave in a directional filter being fully present or fully absent, another simulation was performed. The angle of the plane wave was swept from 0° to 360° with 1° increments when the image SNR was 5, and 12 directional filters were present.

The quality of the reconstructed wave speed maps was evaluated using three performance metrics. The first metric is the estimation error, in which the root mean square (RMS) error is computed for each reconstructed wave speed map with respect to the ground truth. This metric was computed for SPs#1-4.

The second metric is edge response analysis to investigate the resolution. This metric was only evaluated for SP#2 and SP#3. In the reconstructed wave speed maps, the number of pixels required for the transition between two mediums with different wave speeds was measured.

For the third metric, SNR performance, MCSs were conducted on SP#1. The number of trials was chosen as 50. The mean and SD were calculated over 50 trials and then averaged in an ROI of 87x87 pixels. The noise level of AWGN was swept from mean SNR=1 to 5 with 0.1 increments. Note that the "mean SNR" is the expected value of the SNRs of multifrequency displacement data since the

SNR of the displacement data can be different at each frequency due to differences in MEG duration resulting in differences in TE and hence in SNR (${}^{i}\Psi_{mn}$). Thus, this variation was simulated by letting the SNR levels of the complex AWGN vary by 20%.

3.3.4 MRI experiments

MRE experiments were conducted on a Siemens TIM Trio 3 Tesla MRI scanner. A spin-echo echo-planar imaging (EPI-SE) pulse sequence with a trapezoidal motion encoding gradient (MEG) was used for acquisition. A single receive channel of the spine coil was used to record the signal. Data were collected for 8 excitation frequencies, 30 to 72 Hz, with 6 Hz increments. The sequence parameters were TR = 500 ms, TE = 82 ms ($\omega_1/2\pi = 30\ Hz$), TE = 71 ms ($\omega_2/2\pi = 36\ Hz$), TE = 70 ms ($\omega_{3,4,5,6,7,8}/2\pi = [42:6:72]\ Hz$), FOV = 240 mm x 180 mm, resolution = 2.5 x 2.5 x 2.5 mm^3, amplitude of MEG G_{MEG} = 20 mT/m, and number of MEGs $N_{MEG} = 1$. Five slices were acquired in each TR. Two acquisitions were made for each scan by switching the polarity of the zeroth- and first-moment nulled MEG, matched to the excitation frequency. Eight phase offset data were collected for each excitation frequency.

The experimental phantoms (EPs) are shown in Figure 3.2B. EPs#1-2 were prepared from different concentrations of agar-agar powder (Agar-Agar Kobe I pulv., Roth, Karlsruhe, Germany), which were stirred in water and boiled for approximately 2 minutes.

For EP#1, agar-agar powder concentrations for the background, first and second inclusions were 0.75%, 1.00% and 0.65%, respectively. In EP#1, inclusions were injected inside balloons; hence, there were balloon interfaces between the inclusions and the background.

For EP#2, agar-agar powder concentrations for the background, first, second and third inclusions were 1.00%, 0.90%, 1.75% and 1.50%, respectively. There were no interfaces between inclusions and the background in EP#2. A box with

dimensions of 19x15x10 cm^3 was used. A few drops of olive oil were applied to the inner surfaces of the box to allow the phantom to be removed easily without rupturing after solidification. Three rods with diameters of 3.5, 2 and 3.5 cm were placed vertically in the first, second and third inclusions, respectively. The background agar-agar water mixture was poured and allowed to solidify for 12 hours at room temperature. Then, each rod was removed, and each agar-agar powder water mixture was poured and allowed to solidify for half an hour, one by one. The whole phantom was allowed to solidify for another 12 hours at room temperature. An identical box side surface 19x15 cm^2 was cut. For the experiment, the phantom was placed inside the cut box and placed horizontally on the patient table in the MRI scanner, with the cut surface at the top. Hence, the phantom was excited by a plate, driven by a mechanical actuator, through the window opening of the cut box. Unless the phantom was placed in a box during the experiment, deformation was observed as multiple ruptures appeared on the phantom during the experiment. Hence, it was decided to perform the experiments inside a box. Descriptive photographs showing the preparation steps of EP#2 are depicted in 3.3.

Furthermore, multifrequency MRE displacement data of a human liver provided online on BIOQIC-Apps (Charité - Universitätsmedizin Berlin, Berlin, Germany) [60] were utilised in tomoelastography inversion using the mentioned weighting schemes. The excitation frequencies are 30, 40 and 50 Hz, with 2.7 mm in-plane resolution and 5 mm slice thickness.

For all experimental data, assuming a high SNR, noise on the phase was measured using the imaginary (or real) part of the noise measured on the background, inside a rectangular ROI with a size of 96x15 pixels for phantoms and 22x17 pixels for the human abdomen, of the complex MRI signal by averaging in the phase offset and direction of motion dimensions.

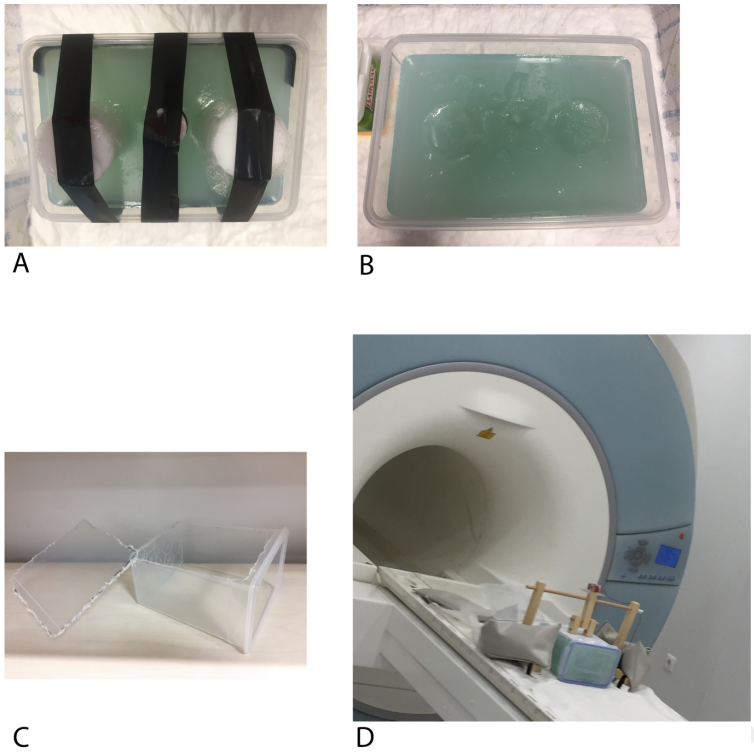


Figure 3.3: (a) Solidifying the background around the rods where inclusions will be poured. (b) Agar-agar solutions are poured after removal of the rods, one by one. (c) Identical box having a cut surface to be used in the experiment. (d) Phantom in B is placed inside the cut box, on the patient table horizontally, excitation is applied by a plate placed through the window opening of the box, driven mechanically.

3.4 Results

3.4.1 Simulation results

Validation of analytical SNR derivations using MCS: The MCS results to validate the SNR derivations are depicted in Figure 3.4. It can be observed that the analytical derivations hold for ${}^{i}\Psi_{mn}(\vec{r}) \geq 3$ since the ratio of the means and SDs becomes steady, and their deviations are approximately 1%. Hence, using Eq. 3.31, the corresponding SNR threshold, ${}^{thr}\Psi_{lmn}(\vec{r})$, was computed at the output of directional filters, equating low SNR weights to zero. In other words, ${}^{thr}\Psi_{lmn}(\vec{r})$ is determined by setting ${}^{i}\Psi_{mn}(\vec{r}) = 3$ in Eq. 3.31, which yields

${}^{thr}\Psi_{lmn}(\vec{r}) = 3u_{0lmn}(\vec{r})\sqrt{N_t}/(\sqrt{2}\alpha)$. Figure 3.4C demonstrates that the SNR of the wave speed computed by MCS deviates from the analytical SNR when the wave propagation direction and direction of one of the directional filters do not exactly match. This deviation is due to the assumption in the derivation that a directional filter exactly matches to a wave or exactly misses it. Since 12 directional filters have been used for this simulation, the largest deviation occurs at multiples of 15°, measured as 9%.

Estimation Error: The estimation accuracy values for the results of tomoelastography inversions using the two different weighting schemes were computed for SPs#1-4, measured by the RMS percentage error normalized to the ground truth. For the amplitude-weighted reconstruction, the normalized RMS errors were 2%, 4%, 6% and 5% for SPs#1, 2, 3 and 4, respectively. The same results were obtained for the SNR-weighted reconstruction, except for SP#2, for which the normalized RMS error was 3%. Wave speed maps, line profiles and mean±SD plots for SP#4 are depicted in Figure 3.5, in which no significant differences are observed between results of two weighting schemes.

Edge Response Analysis: The edge responses on the center cross-sectional line of the reconstructed wave speed maps are illustrated for each weighting technique in Figure 3.6. The number of pixels required for the transition was measured to compare the resolution of the wave speed maps reconstructed using different weightings in tomoelastography inversion. The transition was quantified as 3 pixels for all reconstructions.

SNR Performance: The normalized mean and standard deviation versus mean SNR of complex MRI signal obtained by MCS is demonstrated in Figure 3.7. Note that the normalized mean and standard deviation imply that the computed mean and SD were divided by the ground truth wave speed value of 3.2 m/s. With a low SNR, there is 10% bias when the amplitude-weighted reconstruction has been used, whereas there is no bias when SNR weighting has been used. In addition, the normalized SD for the SNR-weighted reconstruction is lower than the normalized SD of the conventional weighting by a factor of two.

Abdomen MRE Simulations: Reconstructed wave speed maps are depicted in Figure 3.8 for the no-noise and AWGN-added cases and compared with the assigned wave speed values used in the simulation. For the no-noise case, the reconstructed wave speed maps are in good agreement with the ground truth wave speed map, except for some blurriness. For the noise-added case, it can be seen that the wave speed map reconstructed by conventional weighting suffers from noise, whereas the reconstructed wave speed map is slightly affected by noise when SNR weighting has been used.

3.4.2 Experimental results

The reconstructed wave speed maps for EP#1 are depicted in Figure 3.9A. Mean and SD of the measured wave speed values over the selected ROIs (Figure 3.9B) for EP#1 are demonstrated in Figure 3.9C. The second inclusion (0.65%) was expected to be softer than the background (0.75%); however, this result can be only observed for the SNR-weighted reconstruction, whereas in amplitude-weighted inversion, this difference cannot be differentiated well, as shown in Figure 3.9C. The amplitude-weighted reconstruction estimated the wave speed of the second inclusion (0.65%) to be greater than the background (0.75%) with a considerable deviation. It is also observed that, due to the interfaces of the balloons, which have short T_2s, around inclusions, the SNR-weighted reconstruction estimated a low wave speed.

The reconstructed wave speed results for each frequency, weights for each reconstruction and combined wave speed maps for EP#2 are shown in Figure 3.10. Mean and SD of the measured wave speed values over the selected ROIs for EP#2 are reported in Figure 3.11. The mean shear wave speed for the inclusion prepared with 1.75% agar-agar was measured to be greater than that of the inclusion prepared with 1.50% agar-agar only for the SNR-weighted inversion. Wave artifacts existing on the background of wave speed reconstruction using amplitude weights, as observed in Figure 3.10, resulted in greater wave speed deviations (Figure 3.11). To report quantitatively, mean and SD of the estimated wave speed

for the background using amplitude weighted reconstruction is 2.93 ± 0.31 m/s, whereas for SNR-weighted reconstruction mean and SD of the estimated wave speed is 3.00 ± 0.22 m/s.

As observed in Figure 3.10, by comparing the two weighting schemes used in combining the reconstructed wave speed maps at different frequencies, it can be seen that amplitude weighting uses a single reconstruction result more heavily than others for each pixel, which is computed from the data that carry the maximum displacement and discards the other inversion results, because the fourth power of the magnitude of the displacement is used. On the other hand, SNR weighting uses more equally distributed weights.

Single frequency and combined wave speed maps for human liver are given in Figure 3.12A. To compare the computed wave speeds in the liver and spleen with previously reported values in the literature, wave speeds were measured in ROIs depicted on the magnitude image in Figure 3.12B. In the multifrequency result, for the liver, the mean and SD of the wave speeds were calculated as 1.68 ± 0.18 m/s and 1.54 ± 0.20 m/s for the amplitude-weighted and SNR-weighted reconstructions, respectively. For the spleen, the mean and SD of the wave speeds were calculated as 2.50 ± 0.23 m/s and 2.35 ± 0.21 m/s for the amplitude-weighted and SNR-weighted reconstructions, respectively.

3.5 Discussion

In this work, a weighting scheme for combining multi-inversion data to maximize the SNR of the combined wave speed map has been proposed. The proposed reconstruction was evaluated using three quality metrics, namely, estimation accuracy, spatial resolution and SNR performance.

The analytical SNR approximations are derived by assuming that the noise remains approximately Gaussian despite the nonlinear operations in tomoelastography inversion when the SNR is high enough. Hence, the SNR threshold was

determined by comparing the SNR computed by MCSs and analytical approximations. It can be observed in Figure 3.4 that analytical approximations match with the MCS results for ${}^{i}\Psi_{mn}(\vec{r}) > 3$ (Figure 3.4). This result implies that the high SNR assumption used in the derivations fails below this value because the noise significantly deviates from Gaussian. Thresholding is necessary to eliminate the biased wave speed information reconstructed from these data. In addition, the MRE data having SNR below this value carry very little useful information, so they can be eliminated. The weighting schemes that are related to the amplitude of the displacement can be improved by using thresholding. Using the fourth power of the displacement eliminates the low displacement data because it is similar to choosing only the data with the highest displacement value, in a way thresholds the low displacement data, but this method also excludes useful data. Previously, to eliminate biased results from elasticity ROI measurements, various researchers reported wave-speed or shear modulus values in ROIs by masking them with a phase difference SNR threshold [11, 61]. Here, thresholding is done prior to combining multiple wave-speed maps, where SNR threshold has been determined by MCs. Furthermore, SNR estimates are used for weighting to combine multi-inversion results.

Additionally, analytical approximations for SNR are derived for assuming local homogeneity of the MRE magnitude image. For instance, SNR approximations may fail for the regions of tissues with rapid T_2 changes if a T_2-weighted EPI-SE pulse sequence is used, which is a common pulse sequence used in MRE imaging. The underestimation of wave speeds at the balloon interfaces, observed in Figure 3.9, might be due to the assumption of slow variation in the magnitude of the MRI signal spatially in the analytical approximation of the SNR.

Another assumption in the SNR derivations is that the response of the directional filter is set to 1 if the wavenumber is in the range of the directional filter; otherwise, it is set to 0. However, the filter response is not equal to 1 when there is some angle between the direction of the wavenumber and the directional filter while the wavenumber is still in the range of the filter. In Figure 3.4C, it is observed that the analytical SNR deviates from the MCS-computed SNR by 7% at most when twelve directional filters are present and the image SNR is 5.

Furthermore, analytical SNR approximations are derived for a single channel receive coil. When phased array coils are used, the method of obtaining the phase information requires additional nonlinear techniques [62]. One possible solution for this problem is to process each channel information separately. In this case, the determined threshold will still be valid. However, when phase information is obtained from the combined image, a similar analysis must be carried out to understand the effect of these nonlinear techniques on the estimation of the wave speed.

Viscous damping distribution has not been reconstructed in this study. Usually, complex shear modulus is reported in MRE [63–66] , where the real part is the storage modulus related to elastic properties of the tissue and the imaginary part is the loss modulus related to viscous properties of the tissue. To compute viscous damping distribution $\vec{k}$ can be defined as a complex vector while assuming spatially constant wave amplitudes for u_{0lmn}, as formulated in Tzschatzsch et al. [32].

No differences are observed for the estimation accuracies and spatial resolutions of the proposed and conventional weighting schemes, and all of them are in good agreement with the ground truths; however, SNR performance analyses demonstrated that no bias occurred, and the SNR of the wave speed map was improved twofold when SNR weights were used instead of amplitude weights. Therefore, the proposed SNR weighting reconstruction significantly improved the SNR of the final wave speed map while achieving the same performance for the accuracy and spatial resolution compared to that of the conventional reconstruction. Similarly, probably due to noise, amplitude-weighted reconstruction could not have differentiated the wave speed alterations in EPs#1-2, whereas SNR-weighted reconstruction yielded the expected wave speed results, as observed in Figures 3.9- 3.10.

It is not possible to directly compare the method and results in Tzschatzsch et al. [32] because of differences in the implementations of Gaussian smoothing and directional filtering. For instance, the standard deviation of the Gaussian kernel is 2.75 mm in Tzschatzsch et al. [32]; however, it is 2.16 mm for the in-vivo

liver here. Hence, smoothing is slightly less in this study. Also, the compositions of directional filters are different. The directional filter's radial component is a ramp filter in Tzschatzsch et al. [32]. Directional filter in the Eqs. 3.14 -3.15 were utilized to eliminate the black stripe artifacts at organ boundaries, as reported in Tzschatzsch et al. [32] due to directional filters.

Regarding Figure 3.8, the blurriness of reconstructed wave speed maps for both weighting schemes is because of the number of directional filters in tomoelastography reconstruction since increasing the number of directional filters decreases the spatial resolution. For the noise-added case, it is observed that the amplitude-weighted inversion result has been severely affected by noise, whereas the SNR-weighted inversion result has been slightly affected.

In this study, MMRE displacement data for a healthy human abdomen FEM model have been introduced for the first time. The community can also benefit from this model to evaluate their inversion techniques for liver and spleen MRE.

For all experimental phantoms, the wave speeds measured were approximately 30% lower than the values observed by Hamhaber et al. [41], in which the same agar-agar powder had been used. The difference could be the result of using tap water instead of distilled water. Furthermore, the number of motion-encoding directions, excitation frequencies and inversion techniques are different.

The mean wave speeds of the liver and spleen were found to be consistent with the values reported in the literature [32, 57]. Since in-vivo data have a good SNR at the level of 15 approximately, it is not expected to encounter any biases in the results due to noise level. In a good SNR level, amplitude-weighted and SNR-weighted reconstruction should yield similar results, slightly lower or higher than each other, which is also the case here.

When single frequency in-vivo results are analyzed, it is observed that SNR-weighted wave-speed maps are more invariant to excitation frequency used compared to amplitude-weighted results. Low elasticity regions present in the center of the liver in SNR-weighted wave speed map in Figure 3.12, could be due to

elasticity variations in some anatomical details such as blood vessels; however, it is not possible to know the exact reason of this lower elasticity since ground truth for in-vivo data is absent. As future work, to understand such elasticity variations in the SNR-weighted reconstruction, an extended in-vivo study has to be performed on a sufficient number of healthy and unhealthy subjects having age and sex diversity. For this study, despite the absence of a ground truth for the human liver results, based on significant improvements in the SNR of the elastography maps without any loss in resolution and accuracy, one may argue that SNR weighting is useful for MRE inversion.

Inspecting the derived SNR characteristic of the estimated wave speed in Eq. 3.28, it can be seen that most of the parameters are the same spatially and for weighting indices. However, these parameters are necessary for thresholding. The parameters that are not constant are the image SNR, the magnitude of the wavenumber and the amplitude of the displacement. The image SNR may vary spatially, most likely due to variation in the magnitude of the signal or through indices if the imaging parameters differ between scans such as TE. Since the SNR depends on the wavenumber, SNR weighting will favor reconstruction from the lowest excitation frequency among the same wave speed information obtained for the same spatial position if it is assumed that all the other parameters in Eq. 3.28 are constant. If it is assumed that all the parameters except the amplitude of the filtered displacement are constant, then SNR weighting becomes equal to weighting with the square of the amplitude of the displacement with thresholding. To summarize, the proposed method both benefits from weighting with square of SNR and thresholding. For combining wave speed maps with the noise distribution of Gaussian, the optimum weighting for maximum SNR is to use square of SNR [54]. However, for low SNR cases, the noise distribution is not Gaussian; hence estimated SNR is incorrect due to Gaussian noise assumption in the derivations; therefore, thresholding is essential. To demonstrate the effect of thresholding, reconstructed wave speed maps using SNR weights with thresholding and without thresholding for noisy abdomen MRE simulation data have been demonstrated in Figure 3.13. It is observed that without thresholding reconstructed map is is biased in the regions with higher wave speed values.

The proposed weighting scheme may be more advantageous when there are SNR variations in the collected data because due to the image SNR term in Eq. 3.28, improvement in the SNR performance becomes more significant than that in the original weighting scheme. Note that even though the noise level is the same throughout the experiment, the signal level may differ. For example, to collect MRE data at various excitation frequencies, the TE is varied to match it to the excitation frequency unless fractional encoding [67] is used.

When multidirectional and multifrequency data are acquired, the methods developed in this study may be applicable to reconstructions other than tomoelastography, such as Helmholtz's inversion [28–30], multifrequency dual elasto visco inversion [31], nonlinear inversion) [26, 27] and multi-model direct inversion [33]. Note that the SNR-weighted reconstruction requires derivation of the analytical noise statistics. In this work, this derivation has been performed for tomoelastography. For other inversion algorithms, noise statistics must be rederived for the implementation of SNR weighting. Even reconstructions using amplitude-based weighting schemes such as using the first order, second order or energy of the displacement can benefit from employing thresholding.

Another idea could have been using strain weighting instead of amplitude weighting to eliminate cases of low elastic strain because the strain is directly related to the shear; hence, the magnitude of the shear strain produced by motion is more essential than the magnitude of the shear wave displacement. In fact, McGarry et al. [36] showed in their nonlinear inversion method for elasticity reconstruction that strain-SNR measured by the octahedral shear strain (OSS)-SNR is more useful than motion-SNR to determine the reliability of the reconstructed elastogram from the displacement data. Improvements in the elasticity map were demonstrated in [37, 68] when OSS was used for strain weighting in tomoelastography and Helmholtz inversion. Notably, OSS weighting is successful at interfaces and boundaries, which is expected because it uses strain weighting, so the reconstructed wave speed that is computed from the data with greater displacement jumps is weighted more, similar to slip-interface imaging [69].

Moreover, this analysis is consistent with the conclusion of Manduca et al. [52]

since they suggested evaluating the reliability of the elasticity map generated depending on the number of derivatives used based on the number of derivatives in the SNR metric. For instance, it is recommended to use OSS-SNR [36] for the inversion methods consisting of only the first derivative and Laplacian-SNR for the reconstructions using the second derivative of the displacement field.

Furthermore, the SNR characteristics of an MMRE inversion has been investigated for the first time. The SNR derivations that have been developed in this study provide a useful tool for researchers to investigate the sensitivity of the SNR of the final wave speed map to the various parameters of the reconstruction technique, namely, tomoelastography. For example, one may investigate the sensitivity to the number of phase offsets and filter parameters.

3.6 Conclusion

A new weighting scheme for combining multi-inversion reconstructions to maximize the SNR of the final wave speed map in tomoelastography has been proposed. The performance of the proposed weighting scheme is compared with that of the conventional amplitude-based method by using three performance measures, namely, the estimation error, spatial resolution and SNR of the final wave speed maps. SNR weighting significantly improved the SNR performance of the wave speed map while achieving the same performance for accuracy and spatial resolution. In addition, bias in the wave speed map has been eliminated in the low SNR case using the SNR weighting reconstruction.

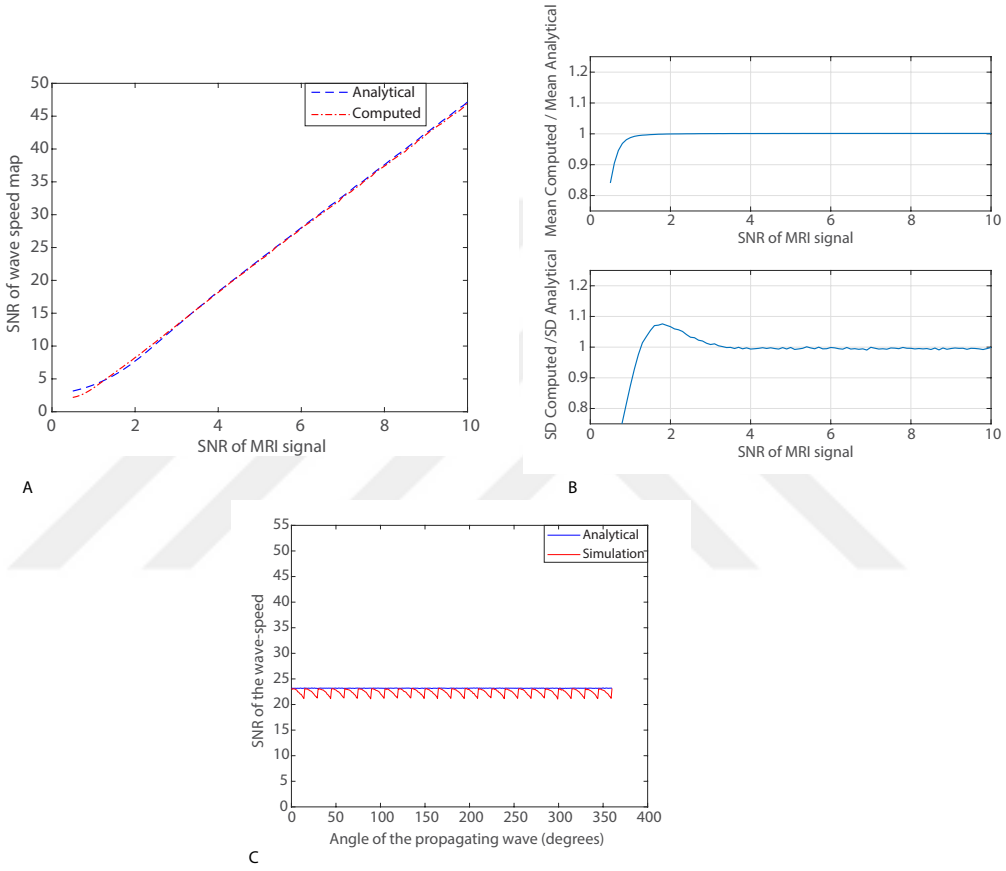


Figure 3.4: Validation of analytical approximations for the SNR by comparing it to the computed SNR using Monte Carlo simulations. (a) The SNR of the wave speed versus the SNR of the complex MRI signal for analytical and computed SNR values. (b) (Top) Ratio of the 2D-averaged mean of the wave speed reconstructed over 100 repetitions to the analytical mean wave speed at each image SNR. (Bottom) Ratio of the 2D-averaged SD of the wave speed reconstructed over 100 repetitions to the analytical SD of the wave speed at each image SNR. It can be observed that analytical derivations hold for ${}^{i}\Psi_{mn}(\vec{r}) \geq 3$ since the ratio of SDs becomes steady. (c) Comparison of analytical and MCS computed SNR, where the x-axis indicates the angle of the plane propagating in the x-y plane (i.e., $\arg\{\vec{k}\}$) when SNR=5, and 12 directional filters are present.

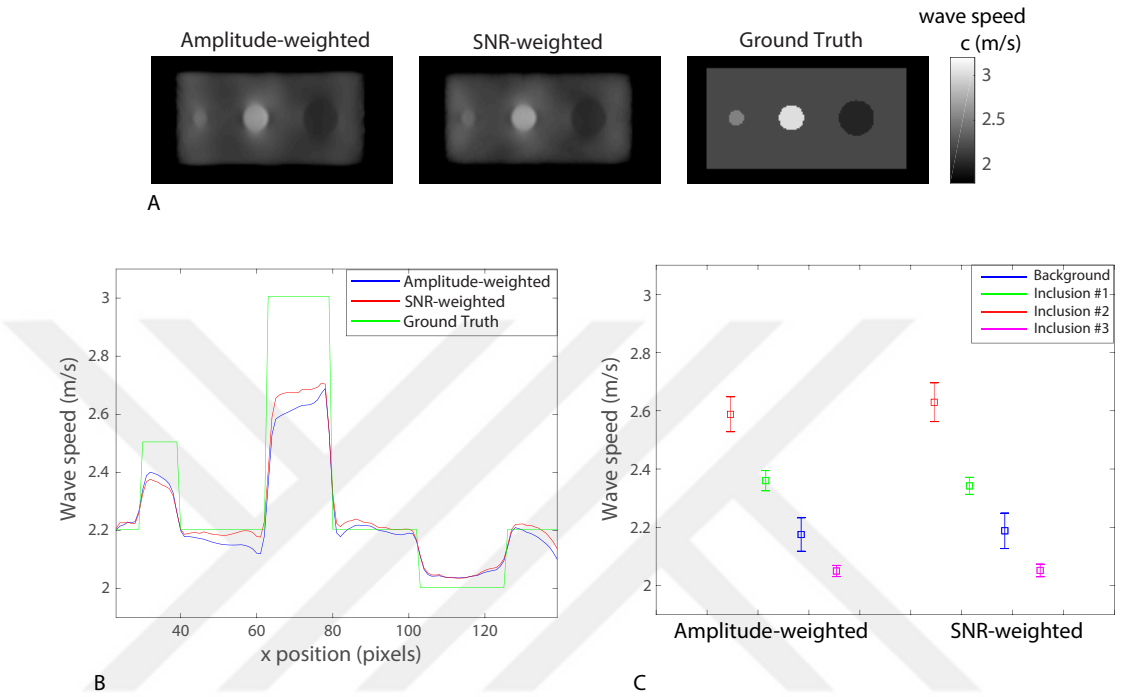


Figure 3.5: (A) Wave speed maps (B) line profiles for center horizontal line (C) mean±SD plots for each region for the two weighting schemes for SP#4. Assigned shear wave speed values are 2.2, 2.5, 3 and 2 m/s for background, inclusion #1-4, respectively.

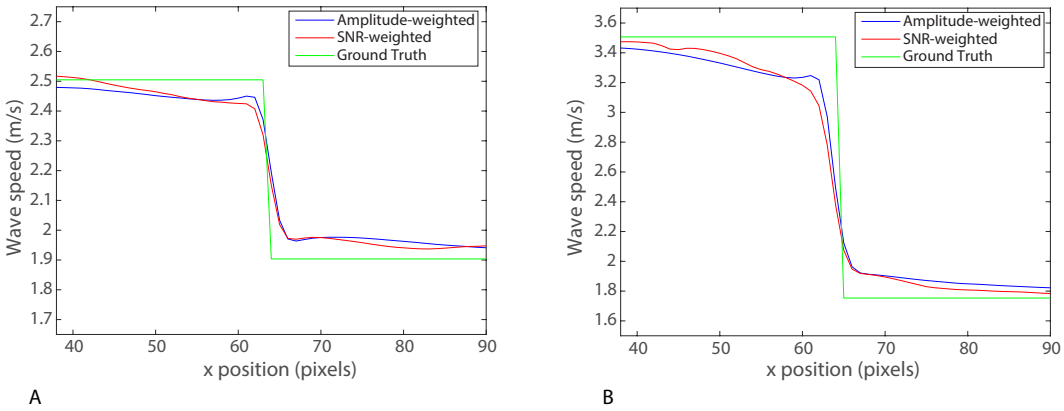


Figure 3.6: Wave speed values plotted for a cross-sectional line near the step between two mediums to analyze edge response for the two weighting schemes for (a) SP#2 and (b) SP#3.

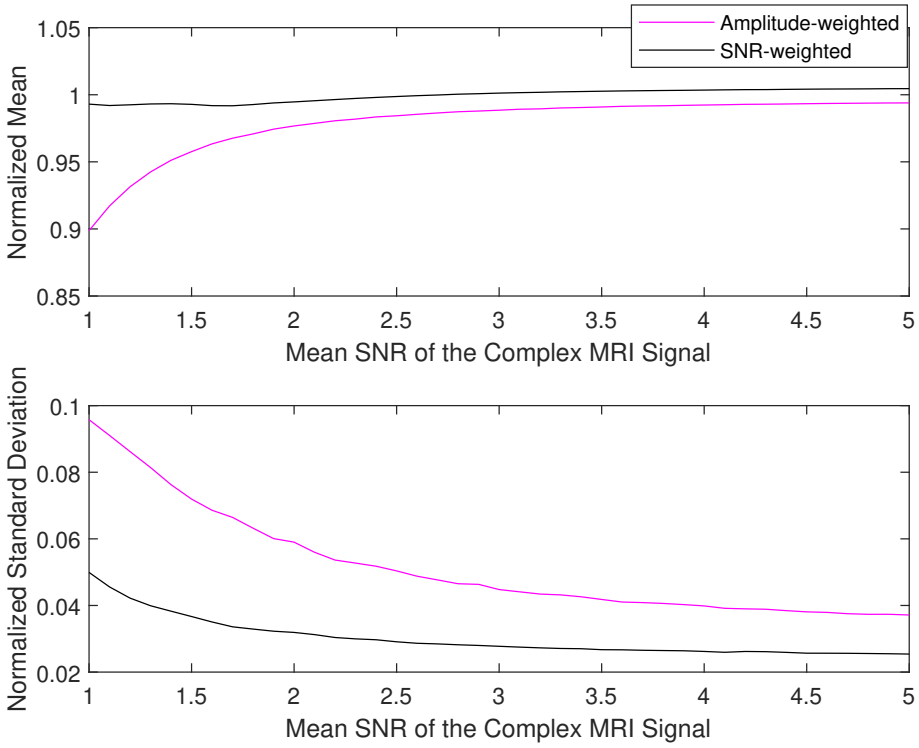


Figure 3.7: SNR performances computed by Monte Carlo simulations. 2D-averaged mean and standard deviation of wave speed maps, normalized to the ground truth wave speed, versus the image SNR.

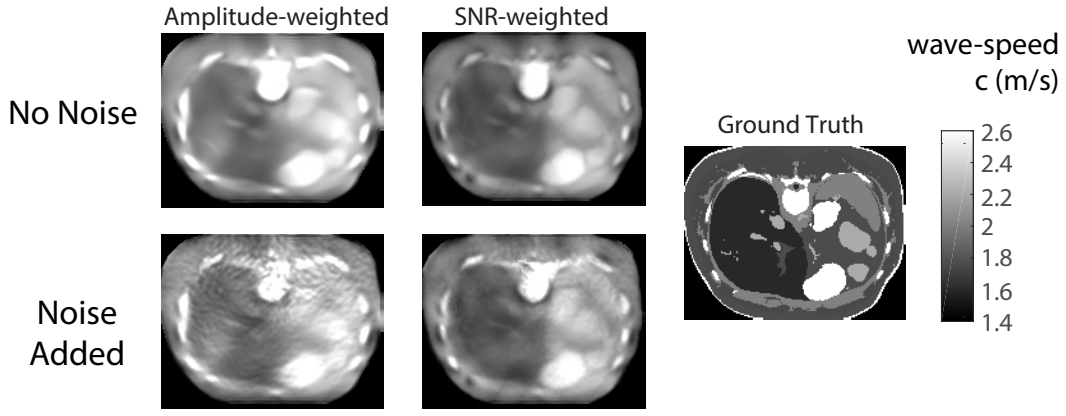


Figure 3.8: Reconstructed wave speed maps for the 3D healthy human abdomen model for the no-noise and noise-added case. The ground truth is also given, demonstrating the magnitude of the assigned wave speed distribution for the simulations.

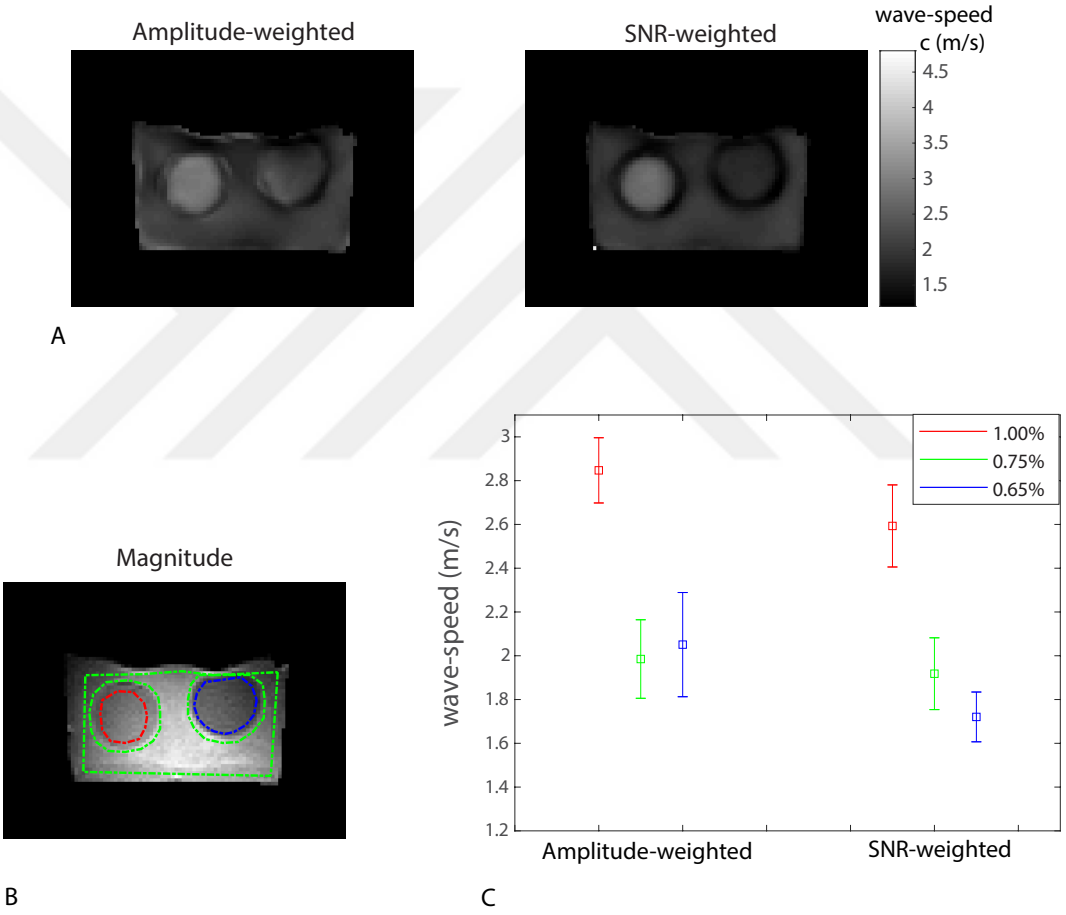


Figure 3.9: For EP#1 (a) Reconstructed wave speed maps (b) Selected ROIs for measuring wave speed values, depicted on the MRE magnitude image. The ROI for the background is selected as the region between the green curves. (c) Mean and SD values over the ROI, shown by squares and bars, respectively.

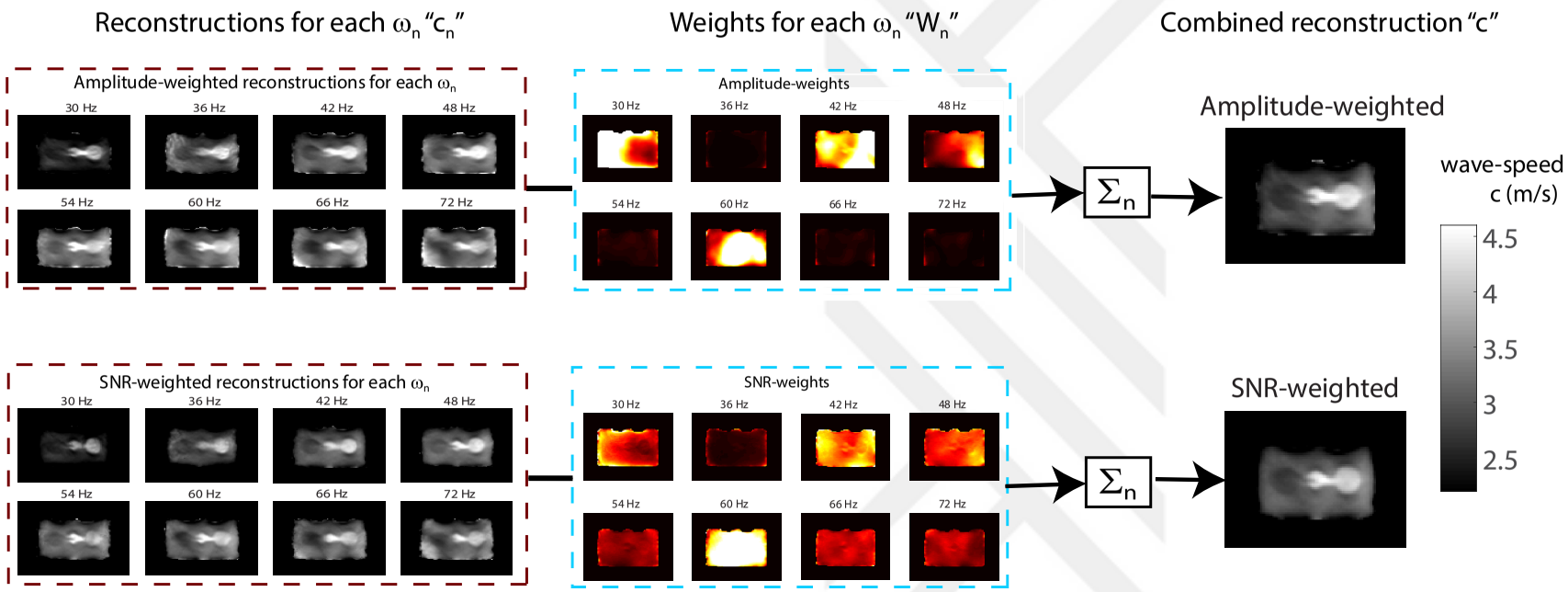


Figure 3.10: Reconstructed wave speed maps and weights for the two weighting schemes at each frequency in addition to the combined wave speed maps for EP#2.

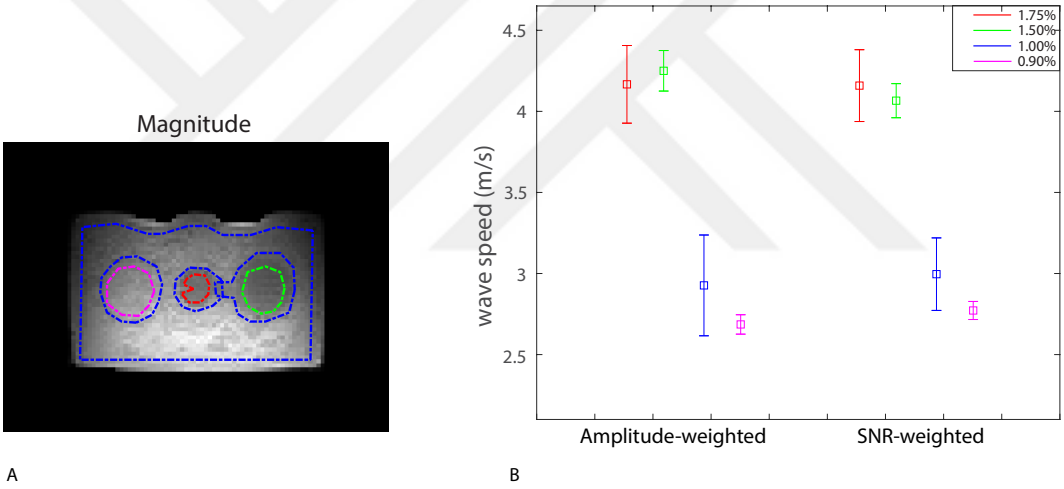


Figure 3.11: For EP#2 (a) Selected ROIs for measuring wave speed values, depicted on the MRE magnitude image. The ROI for the background is selected as the region between the blue curves. (b) Mean and SD values over the ROI, shown by squares and bars, respectively.

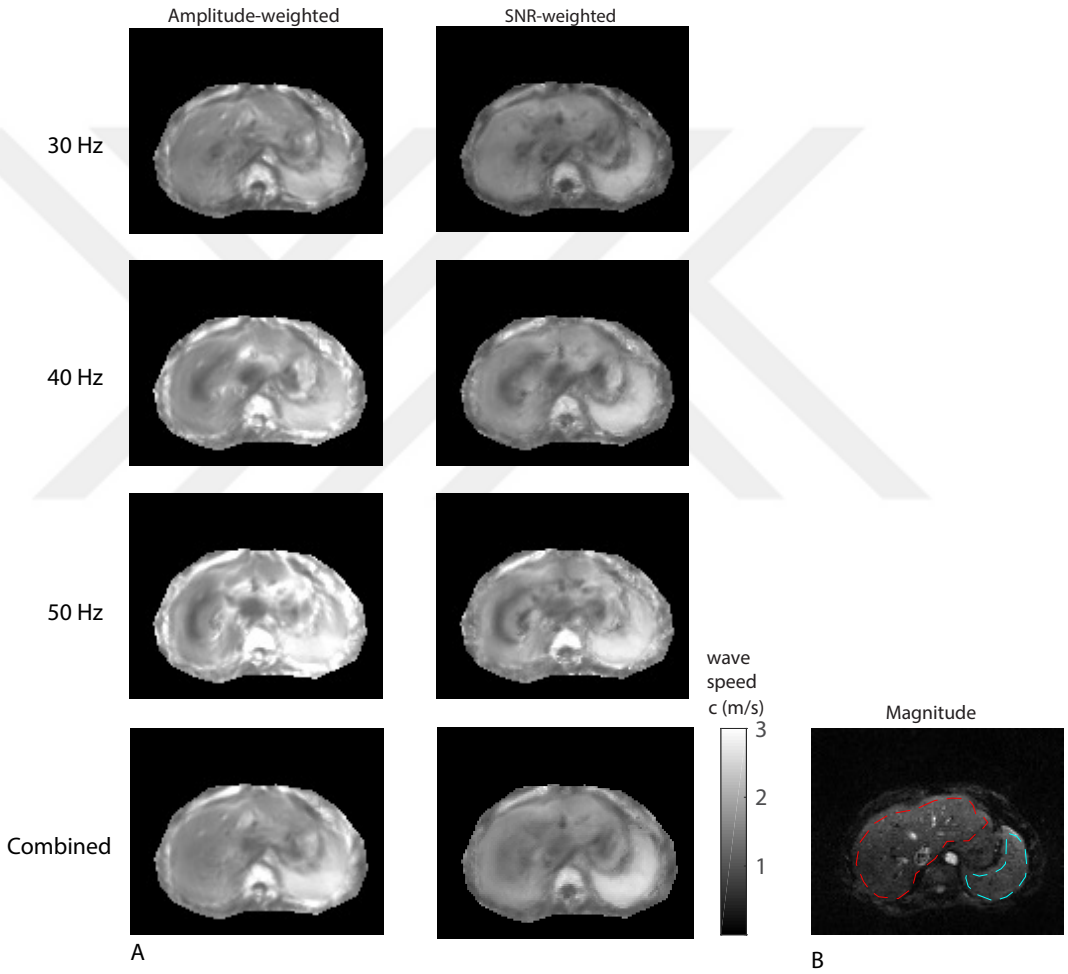


Figure 3.12: (a) Single frequency and combined multifrequency results for wave speed maps for MRE abdomen data. (b) Anatomical ROIs (liver (red) and spleen (blue)), selected on the MRE magnitude image, for measuring the mean and SD of the estimated shear wave speeds.

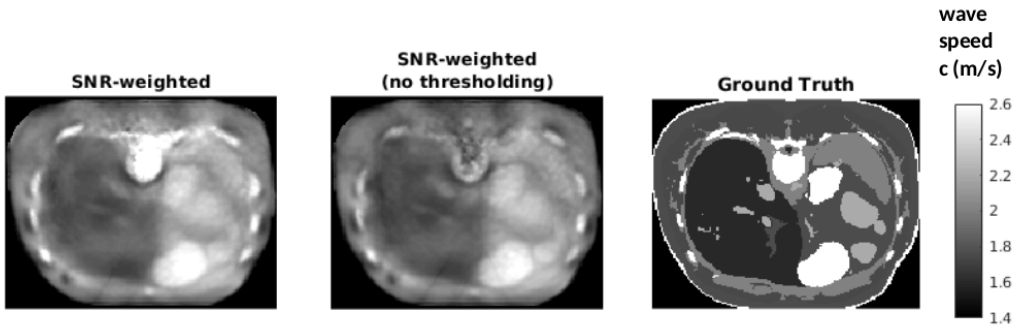


Figure 3.13: Reconstructed wave speed maps using SNR weights with and without thresholding for the 3D healthy human abdomen model noise-added case. The ground truth isalso given, demonstrating the magnitude of the assigned wave speed distribution for the simulations.

Chapter 4

Improving the SNR and Correcting the Bias in Elastograms in Helmholtz Inversion for MRE

4.1 Introduction

In MR elastography (MRE), 3D Helmholtz inversion is widely used for elasticity reconstruction [29, 70], which is also applicable to multifrequency MRE (MMRE) [31]. Noise in the collected MRE data may cause bias in the estimation of elasticity. Prior to the inversion, using weighted-least-squares (WLS) with the SNR estimate of each complex shear moduli using SNR thresholding, may improve the SNR and reduce the bias in the SNR of the elastogram.

4.2 Theory

The primary noise on the complex MRI signal can modelled as additive white Gaussian noise (AWGN). Using high SNR assumption, the standard deviation of the noise on the phase is equal to SNR of the MRI signal (i.e., image SNR) and noise distribution of the complex shear modulus $\boldsymbol{G^*}(\vec{r})$ can be derived analytically for Helmholtz inversion, similar to the analysis conducted for tomoelastography. For each motion direction and excitation frequency, an equation is obtained using Helmholtz equation. Each equation represents a row in $\boldsymbol{\Delta u}(\vec{r},\omega)\boldsymbol{G^*}(\vec{r}) = -\rho\omega^2\boldsymbol{u}(\vec{r},\omega)$, where it is solved for $\boldsymbol{G^*}(\vec{r})$, for each position $\vec{r}$. Here, Δ is Laplacian operator, $\boldsymbol{u}$ is the displacement vector, $\omega = 2\pi f_{exc}$ and f_{exc} is the excitation frequency. Note that in Laplacian operator can be in 3D as in Hirsch et al. [30] or by assuming single polarity of motion it can be implemented in 2D as in Papazoglou et al. [31]. Here, single polarity of motion was assumed, hence Laplacian operator reduced to second derivative operator [31]. Each equation is weighted by its using weighted-least-squares (WLS) method to improve SNR of the inversion. If the SNR value cannot meet the minimum SNR threshold required for the high SNR assumption in the analytical derivations, then that equation (i.e., row) is simply deleted, hence not involved in the inversion. The thresholding reduces the bias in the elasticity inversion.

Considering the noise on the complex MRI signal, and with the high SNR assumption formulating noise on the displacement u, similar to the derivation in Chapter 3, noise on shear modulus is estimated on $\boldsymbol{G^*}(\vec{r}) = -\rho\omega^2\boldsymbol{u}(\vec{r},\omega)/\boldsymbol{\Delta u}(\vec{r},\omega)$. To derive noise characteristics for the division operation, Taylor series expansion was used and first term in the expansion was considered, ignoring higher order terms due to high SNR assumption. Here, the second derivative term is responsible from the bias due to noise.

By high SNR assumption, it is assumed that Gaussian noise on the complex MRI signal is still Gaussian despite the nonlinear operations in the inversion algorithm.

If the derivative kernel is chosen as central difference $d = [0.5 \quad 0 \quad -0.5]/\delta$, then SNR of the complex shear modulus G^* is given as:

$$\Psi_{G^*} = \frac{-u_0(0.25u_{-2} - 0.5u_0 + 0.25u_2)}{\sqrt{(0.25u_{-2} + 0.25u_2)^2\psi_0^2 + 0.0625u_0^2\psi_{-2}^2 + 0.0625u_0^2\psi_2^2}} \tag{4.1}$$

4.3 Methods

To verify SNR approximations, Monte Carlo simulations (MCS) were performed on a simulated plane wave data by adding AWGN with SNR swept from 1 to 30 by 0.5 increments. The minimum SNR required for the high SNR assumption used in the derivations was determined by comparing MCS results with the analytical approximations. MMRE simulations were conducted on a phantom with two homogeneous mediums. Elasticity maps were generated using the original Helmholtz inversion and the proposed inversion for both no-noise and noise added cases. Then, the SNR performance of the proposed inversion was assessed by adding AWGN for each SNR level, and then by computing the elasticity map and its SNR by MCS. Furthermore, the brain model, described in previous chapters, consisting of scalp, skull, falx cerebri, cerebrospinal fluid, gray matter and white matter, developed from the segmented brain images of a healthy human, was imported to COMSOL Multiphysics (COMSOL, Stockholm, Sweden). Young's modulus, Poisson's ratio, density and damping parameters were assigned to the model. MMRE brain simulation data were collected by performing frequency domain analysis on the model, by rotationally vibrating the head about the y -axis, similar to the excitation of a bite actuator. The excitation frequency was swept from 24 to 60 Hz with 4 Hz increments. Furthermore, elasticity inversions for an in-vivo MMRE brain data [17], comprising excitation frequencies from 20 to 60 Hz with 5 Hz increments, were obtained for both reconstructions.

4.4 Results

Validation of SNR analytical approximations using MCS is depicted in Figure 4.1, demonstrating mean, standard deviation and SNR of the magnitude of the complex shear modulus $|G^*|$. The minimum image SNR value that analytical approximations hold is determined as 10. For image SNR < 10, the noise on the elastogram is not Gaussian, hence the derivations do not hold.

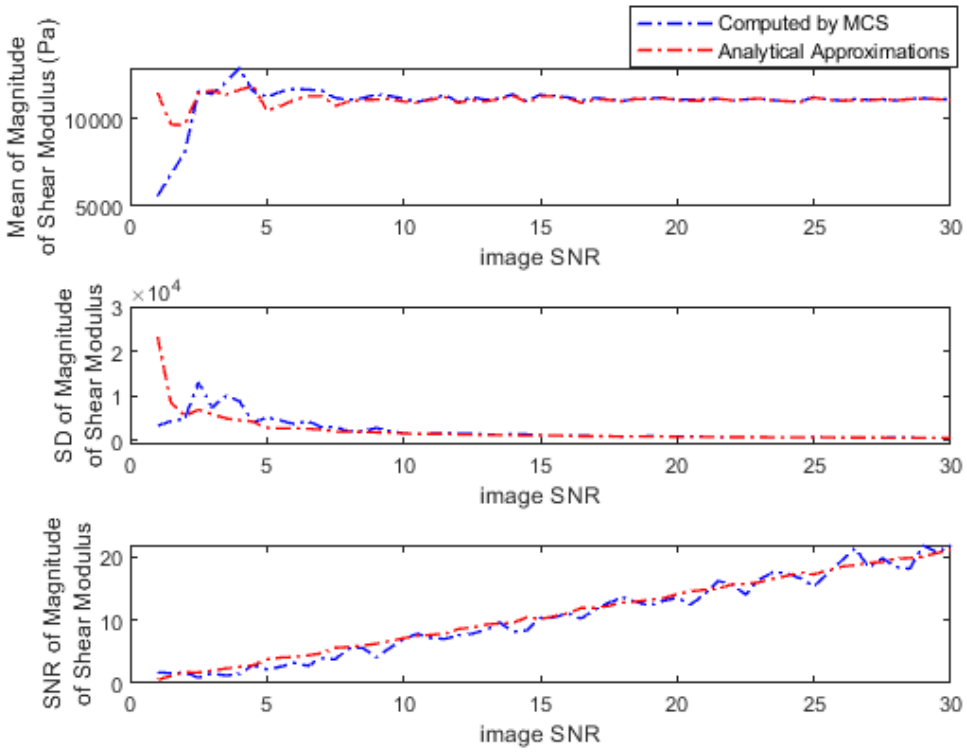


Figure 4.1: Validation of analytical approximations by Monte Carlo simulations are demonstrated by mean, standard devitation (SD) and SNR of magnitude of complex shear modulus versus image SNR. The minimum image SNR value that analytical approximations hold is determined as 10.

Elasticity maps for the simulation phantom with two homogeneous mediums are given in Figure 4.2. SNR performance of the inversions are demonstrated in Figure 4.3, depicting estimated magnitude of shear moduli normalized with respect to the ground truth and their SNR.

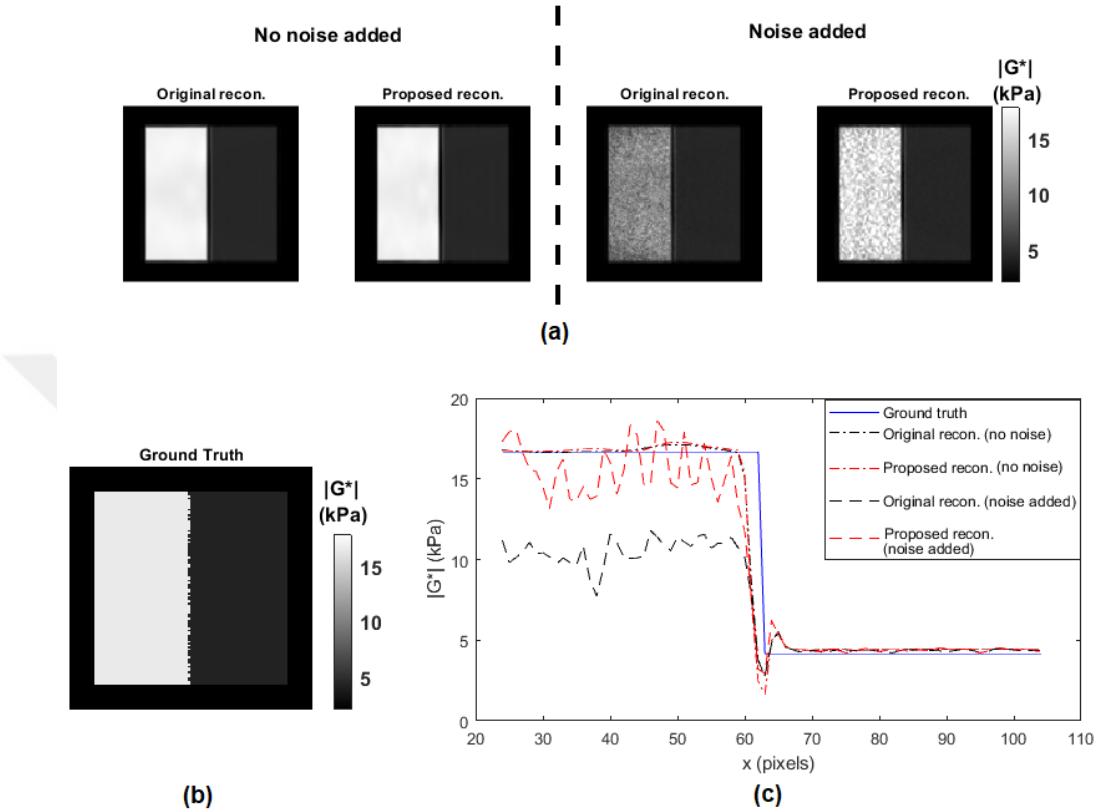


Figure 4.2: (a) Magnitude of complex shear modulus ($|G^*|$) maps for simulation phantom for no-noise and noise added case. (b) Ground truth for $|G^*|$ map for the simulation phantom. (c) Horizontal profiles of $|G^*|$ maps in (a) and (b).

Inversion results for simulated 3D brain MRE data for no-noise and noise added cases are shown in Figure 4.4. In-vivo brain elastograms are given in Figure 4.5.

4.5 Discussion and Conclusion

Analytical approximations for SNR of the complex shear modulus have been validated by MCS and the SNR threshold required for the approximations to hold has been determined (Figure 4.1). Inversion results for the simulation phantom given in Figure 4.2 demonstrates that elasticity is underestimated in the stiff region by approximately 35% due to noise when the original Helmholtz inversion is used. Fortunately, this bias can be corrected by the proposed reconstruction, as

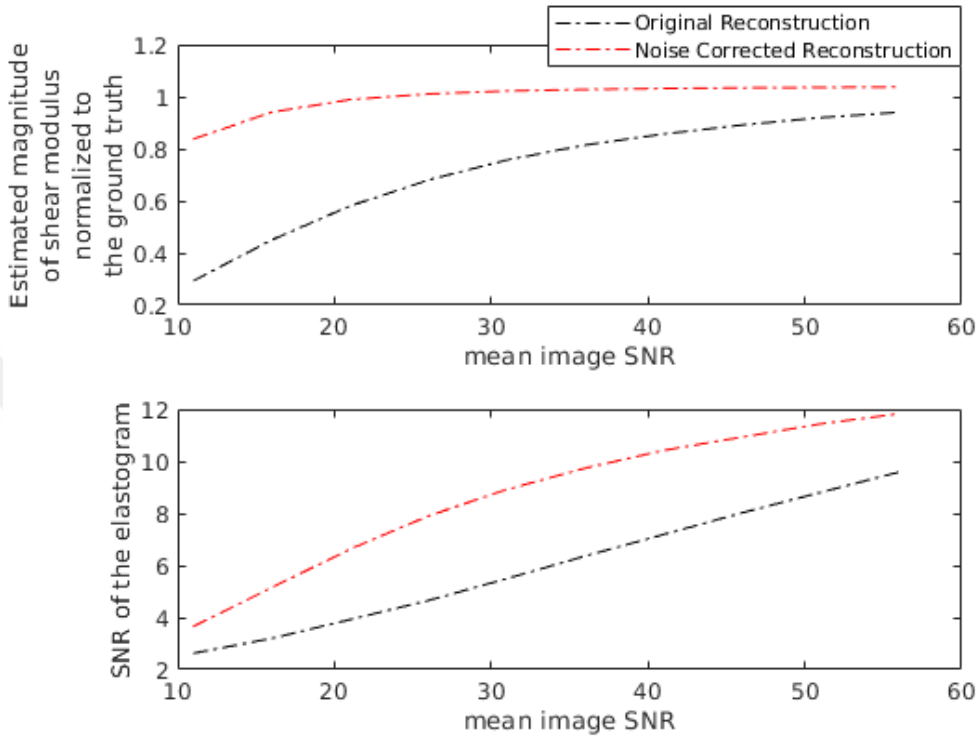


Figure 4.3: Estimated magnitude of mean complex shear modulus ($|G^*|$) normalized to the ground truth and SNR of $|G^*|$ versus mean image SNR. Hence, mean $|G^*|$ normalized to the ground truth is desired to be equal to 1.

seen in Figure 4.2. Underestimation of shear modulus by the original Helmholtz inversion for different SNR levels is observed in Figure 4.3. For the proposed inversion, bias is 10% for SNR=25 and there is almost no bias when SNR is 30, whereas for the original inversion underestimation is 50% when SNR is 30. As observed in Figure 4.3, SNR of the elastogram improved by 1.6 times with the proposed reconstruction. In Figure 4.4, it can be seen that for noisy data, the original reconstruction underestimates the complex shear modulus, whereas underestimation is less for the proposed inversion. Comparing reconstructed elasticity maps with the ground truth for the no-noise case, one can conclude that the Helmholtz inversion is not exactly accurate and has resolution problems with low reconstruction SNR gain. Consistent with the simulation results, the estimate of the complex shear modulus map has increased when the proposed noise corrected inversion is used compared to the original inversion, as given in Figure 4.5.

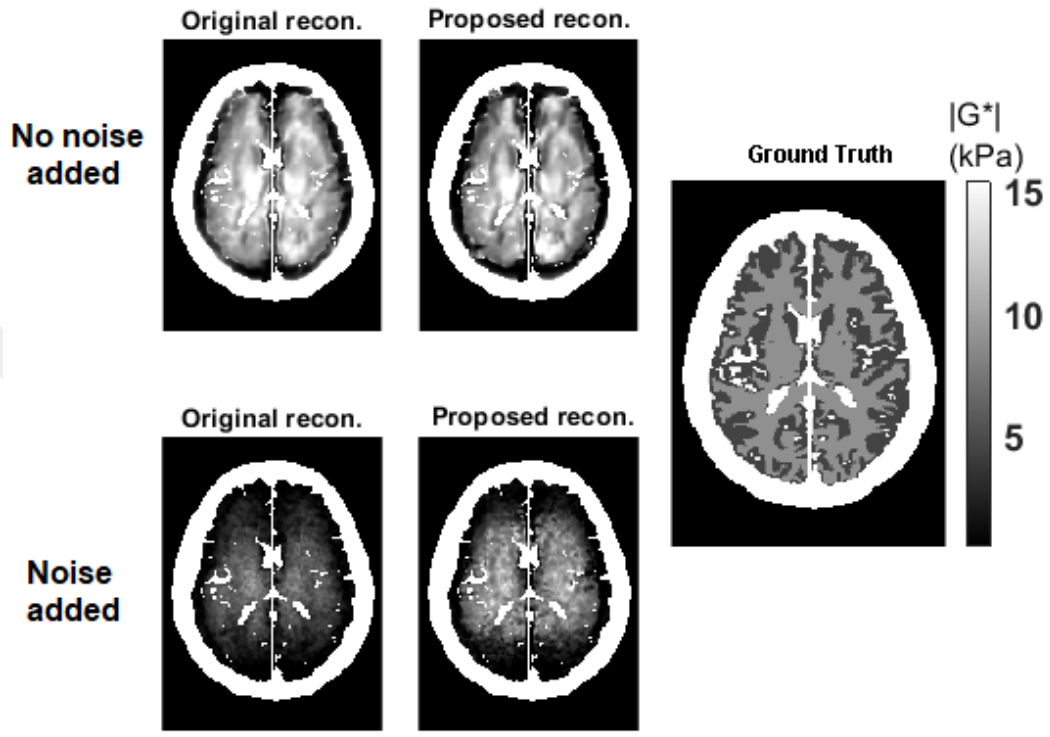


Figure 4.4: $|G^*|$ maps for the simulated brain MRE data for the no-noise and noise added cases, compared with the ground truth $|G^*|$.

In the SNR derivations, second order term in Taylor expansion should be included, which will yield an SNR threshold depending on resolution δ, excitation frequency f_{exc} and shear modulus G^*. Due to ignoring second order in the Taylor expansion in SNR derivations, there is still bias for image $SNR > 10$, as depicted in Figure 4.3. Because the threshold was determined for the simulation phantom in Figure 4.1. As future work, the threshold can be implemented by comparing the noise contribution due to the first and second derivative terms. This comparison may show the dependence of the threshold on resolution, excitation frequency and shear modulus. Since shear modulus is the unknown parameter, thresholding should be iterative.

Furthermore, SNR analysis should be re-derived without the assumption of single polarization of motion.

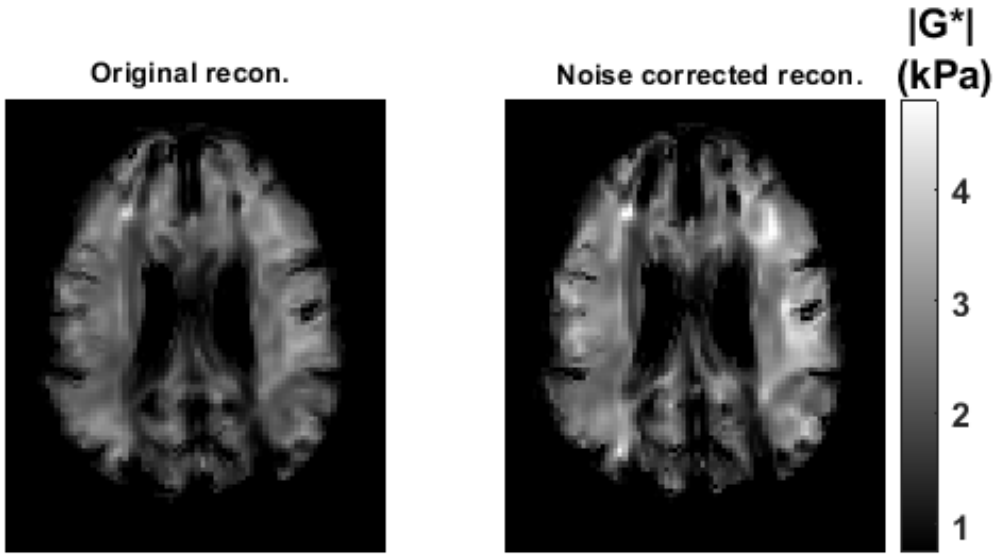


Figure 4.5: Reconstructed $|G^*|$ maps for in-vivo human brain.

The Helmholtz inversion is one of the most common inversion techniques used among MRE research groups. The bias in the estimation of the elasticity, caused by noise in the data, is significantly reduced when thresholded SNR estimates of elasticities were included in the inversion using WLS method.

Chapter 5

Use of Octahedral Shear Strain in the MRE Inversion

5.1 Introduction

Inversion techniques involving multifrequency MR elastography (MMRE) compensate the influence of amplitude nulls on the elastograms [31, 32], by combining computations at different frequencies by amplitude-weighted averaging or directly without any weighting. Because shear strain relates to shear modulus, strain-SNR is more reliable than motion-SNR to estimate data quality in reconstructing elastography maps [36]. Therefore, combining inversions at different frequencies using octahedral shear strain (OSS) weighted averaging may give more reliable maps [68]. The purpose of this study is to investigate the effect of OSS-weighting on multifrequency inversion techniques such as tomoelastography [32] and multifrequency Helmholtz inversion [31].

Here, it is proposed to use strain-weighting instead of amplitude-weighting to eliminate cases of low elastic strain [68]. The strain is directly related to the shear, hence the magnitude of the shear strain produced by motion is more essential than the magnitude of the shear wave displacement. In fact, it has been shown

by McGarry et al. [36] in their non-linear inversion method for elasticity reconstruction that strain-SNR measured by the octahedral shear strain (OSS)-SNR is more useful than motion-SNR to determine the reliability of the reconstructed elastogram from the displacement data.

5.2 Theory

The original tomoelastography which uses amplitude weighting as described in Chapter 4 was implemented to be compared with proposed OSS-weighted tomoelastography. For the proposed strain-weighted reconstruction, OSS computation has been used, which is the maximum value of shear strain on any plane, defined by the equation:

$$\begin{aligned} OSS(\vec{r}) =& \frac{2}{3}\Big((\epsilon_{xx}(\vec{r}) - \epsilon_{yy}(\vec{r}))(\epsilon_{xx}(\vec{r}) - \epsilon_{yy}(\vec{r}))^* \\ &+ (\epsilon_{yy}(\vec{r}) - \epsilon_{zz}(\vec{r}))(\epsilon_{yy}(\vec{r}) - \epsilon_{zz}(\vec{r}))^* \\ &+ (\epsilon_{xx}(\vec{r}) - \epsilon_{zz}(\vec{r}))(\epsilon_{xx}(\vec{r}) - \epsilon_{zz}(\vec{r}))^* \\ &+ 6(\epsilon_{xy}(\vec{r})\epsilon^*_{xy}(\vec{r}) + \epsilon_{yz}(\vec{r})\epsilon^*_{yz}(\vec{r}) + \epsilon_{xz}(\vec{r}))\epsilon^*_{xz}(\vec{r}))\Big)^{0.5}, \end{aligned} \tag{5.1}$$

where * denotes the complex conjugate operation and ϵ is the complex strain, which is calculated as follows:

$$\begin{bmatrix} \epsilon_{xx} & \epsilon_{xy} & \epsilon_{xz} \\ \epsilon_{yx} & \epsilon_{yy} & \epsilon_{yz} \\ \epsilon_{zx} & \epsilon_{zy} & \epsilon_{zz} \end{bmatrix} = \begin{bmatrix} \frac{du_1}{dx} & \frac{1}{2}(\frac{du_1}{dy} + \frac{du_2}{dx}) & \frac{1}{2}(\frac{du_1}{dz} + \frac{du_3}{dx}) \\ \frac{1}{2}(\frac{du_2}{dx} + \frac{du_1}{dy}) & \frac{du_2}{dy} & \frac{1}{2}(\frac{du_2}{dz} + \frac{du_3}{dy}) \\ \frac{1}{2}(\frac{du_3}{dx} + \frac{du_1}{dz}) & \frac{1}{2}(\frac{du_3}{dy} + \frac{du_2}{dz}) & \frac{du_3}{dz} \end{bmatrix}$$

OSS-weights are only used for weighting in frequency index and the original, $\hat{u}^4_{0lmn}$ weighting is used for propagation and motion encoding directions, i.e.,

$$W_{lmn}(\vec{r}) = \frac{\sqrt{OSS_n(\vec{r})}\sum_n \hat{u}^4_{0lmn}(\vec{r})}{\sum_{lmn}\sqrt{OSS_n(\vec{r})}\sum_n \hat{u}^4_{0lmn}(\vec{r})}. \tag{5.2}$$

Note that here, the square-root of OSS has been used because strain is related to the square of the wave speed.

Additionally, OSS weighting can be applied to any multifrequency MRE inversion. Here, OSS weighting is used on Helmholtz inversion, which is explained in Chapter 5. Note that OSS weights were added using weighted-least-squares method prior to the inversion.

5.3 Methods

For OSS-weighted tomoelastography, the methodology used are the same as described in Section 4.3.

Additionally, OSS-weighted Helmholtz inversion was tested on simulated brain data and in-vivo brain data. The results for no-weighting and OSS-weighted were compared. Furthermore, the brain model, described in Chapter 2, was used. Using COMSOL Multiphysics, frequency domain analysis was performed by rotating the head around y-axis, similar to the excitation of a bite actuator (i.e. head bobble excitation). Excitation frequency was swept from 24 to 60 Hz with 4 Hz increments. In addition, a human brain data acquired in a recent study [17], were used. The brain data were obtained with 2 mm isotropic voxels and excitation frequency was swept from 20 to 60 Hz with 5 Hz increments.

5.4 Results

Estimation Error: The estimation accuracy values for the results of tomoelastography inversions using the two different weighting schemes were computed for SPs#1-4, measured by the RMS percentage error normalized to the ground truth. For the amplitude-weighted reconstruction, the normalized RMS errors were 2%, 4%, 6% and 5% for SPs#1, 2, 3 and 4, respectively. For the OSS-weighted reconstruction, the normalized RMS errors were 2%, 3%, 6% and 5% for SPs#1, 2, 3 and 4, respectively. Wave speed maps, line profiles and mean±SD plots for SP#4 are depicted in Figure 5.1, in which no significant differences are observed

between results of two weighting schemes.

Edge Response Analysis: The edge responses on the center cross-sectional line of the reconstructed wave speed maps are illustrated for each weighting technique in Figure 5.2. The transition was measured as 3 pixels for both reconstructions.

SNR Performance: The normalized mean and standard deviation versus mean SNR of complex MRI signal obtained by MCS is demonstrated in Figure 5.3. With a low SNR, there is 10% bias when the amplitude-weighted reconstruction has been used, whereas bias is smaller than 1% when OSS weighting has been used. However, the normalized SD for the OSS-weighted reconstruction is higher than the normalized SD of the conventional weighting.

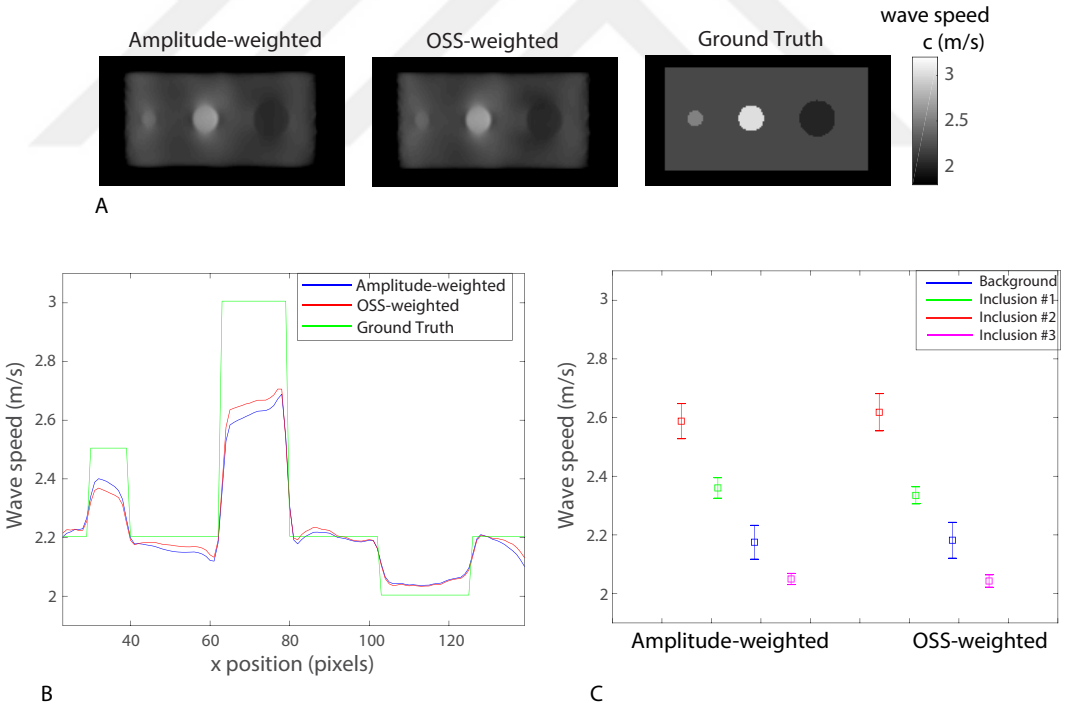
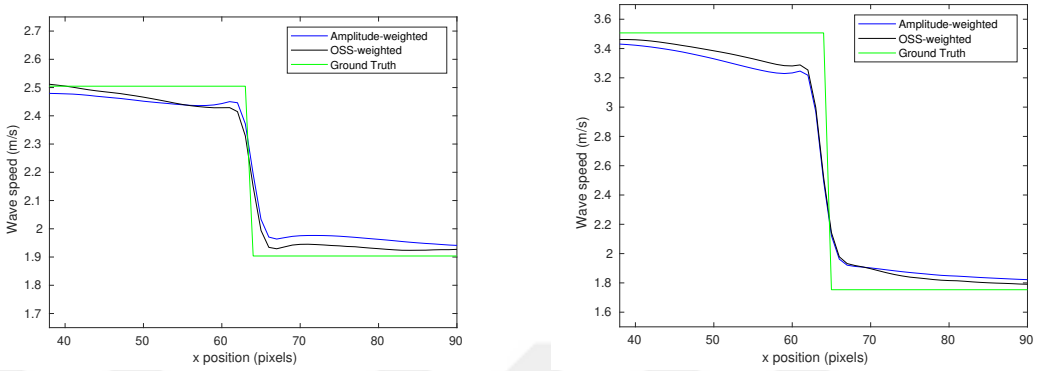


Figure 5.1: (a) Wave speed maps (b) line profiles for center horizontal line (c) mean±SD plots for each region for the two weighting schemes for SP#4. Assigned shear wave speed values are 2.2, 2.5, 3 and 2 m/s for background, inclusion #1-4, respectively.

Abdomen MRE Simulations: Reconstructed wave speed maps are depicted in Figure 5.4 for the no-noise and AWGN-added cases and compared with the assigned wave speed values used in the simulation. For the no-noise case, the



(a) (b)

Figure 5.2: Wave speed values plotted for a cross-sectional line near the step between two mediums to analyze edge response for the two weighting schemes for (a) SP#2 and (b) SP#3.

reconstructed wave speed maps are in good agreement with the ground truth wave speed map, except for some blurriness. For the noise-added case, it can be seen that the wave speed map reconstructed by conventional weighting suffers from noise, whereas the reconstructed wave speed map is slightly affected by noise when SNR weighting has been used.

Brain MRE Simulations For brain model MRE data, elasticity maps reconstructed by OSS-weighted and conventional Helmholtz inversion are given in Figure 5.5.

5.4.1 Experimental results

The reconstructed wave speed maps for EP#1 are depicted in Figure 5.6A. Mean and SD of the measured wave speed values over the selected ROIs (Figure 5.6B) for EP#1 are demonstrated in Figure 5.6C. The second inclusion (0.65%) was expected to be softer than the background (0.75%); however, this result cannot be observed for both weighting schemes observe this result only for the SNR-weighted reconstruction. Balloon interfaces caused less artifact when OSS weighting was used.

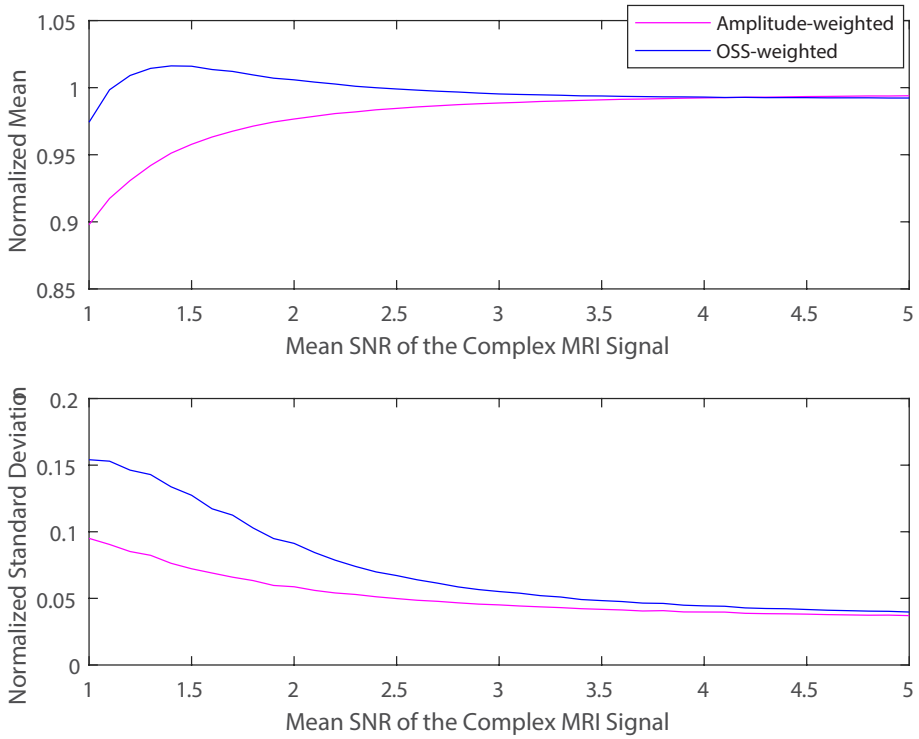


Figure 5.3: SNR performances computed by Monte Carlo simulations. 2D-averaged mean and standard deviation of wave speed maps, normalized to the ground truth wave speed, versus the image SNR.

The reconstructed wave speed results for each frequency, weights for each reconstruction and combined wave speed maps for EP#2 are shown in Figure 5.7. Mean and SD of the measured wave speed values over the selected ROIs for EP#2 are reported in Figure 5.8. The mean shear wave speed for the inclusion prepared with 1.75% agar-agar was measured to be less than or equal to that of the inclusion prepared with 1.50% agar-agar for both weighting schemes, which was not expected.

As observed in Figure 3.10, by comparing the two weighting schemes used in combining the reconstructed wave speed maps at different frequencies, it can be seen that amplitude weighting uses a single reconstruction result more heavily than others for each pixel, which is computed from the data that carry the maximum displacement and discards the other inversion results, because the fourth power of the magnitude of the displacement is used. On the other hand, SNR

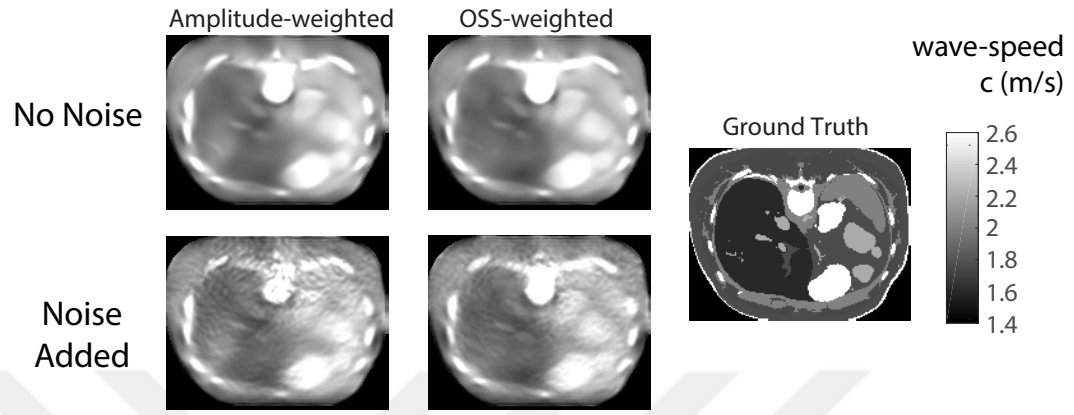


Figure 5.4: Reconstructed wave speed maps for the 3D healthy human abdomen model for the no-noise and noise-added case. The ground truth is also given, demonstrating the magnitude of the assigned wave speed distribution for the simulations.

weighting uses more equally distributed weights.

Single frequency and combined wave speed maps for human liver are given in Figure 5.9A. To compare the computed wave speeds in the liver and spleen with previously reported values in the literature, wave speeds were measured in ROIs depicted on the magnitude image in Figure 5.9B. In the multifrequency result, for the liver, the mean and SD of the wave speeds were calculated as $1.68\pm0.18\ m/s$ and $1.77\pm0.26\ m/s$ for the amplitude-weighted and SNR-weighted reconstructions, respectively. For the spleen, the mean and SD of the wave speeds were calculated as $2.50\pm0.23\ m/s$ and $2.42\pm0.19\ m/s$ for the amplitude-weighted and SNR-weighted reconstructions, respectively.

For in-vivo brain MRE data, elasticity maps reconstructed by OSS-weighted and conventional Helmholtz inversion are given in Figure 5.10.

5.5 Discussion and Conclusion

In this study, strain weighting was proposed instead of amplitude weighting for combining multifrequency inversion results.

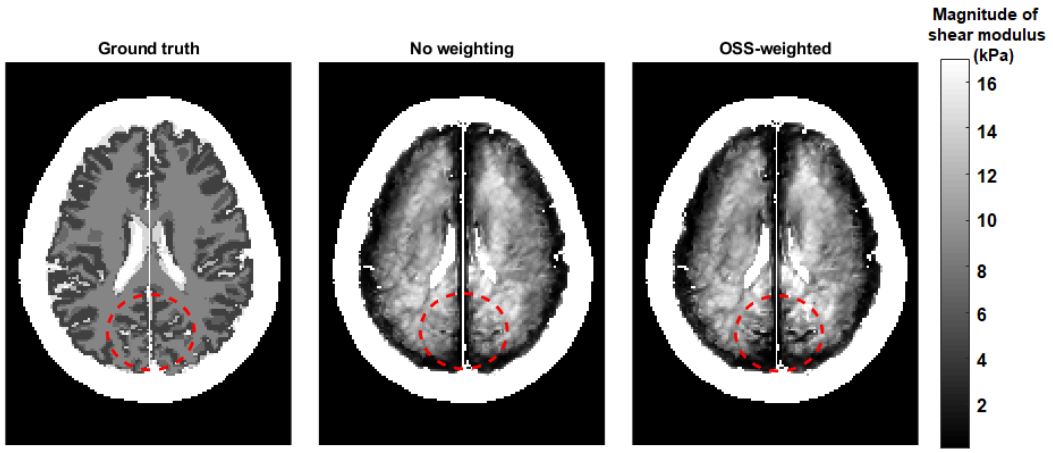


Figure 5.5: Ground truth, conventional multifrequency Helmholtz inversion (no-weighting) and OSS-weighted Helmholtz inversion for the brain simulation data. Differences between no-weighting and OSS-weighted inversions are observed mainly in sulci of the brain.

Two weighting schemes were compared for three performance metrics, namely estimation accuracy, resolution and SNR performance. No differences were observed for estimation accuracy and resolution Figure 5.1, 5.2. Bias was reduced in low SNR cases when OSS weighting was used; however, SNR of the wave speed map decreased 5.3, compared to amplitude-weighted reconstruction.

In the liver simulation, reconstructed wave speed maps are in good agreement with the ground truth for no noise case. For the noise added case, SNR of the OSS-weighted map is slightly greater than amplitude-weighted map. Here, the added noise has an SNR level of 20, hence according to the simulation results, the SNR performances are expected to be the same.

Regarding EP#1 results in Figure 5.6, reconstructed median wave speed values for 0.75% and 0.65% agar-agar concentrated inclusions are the same, in other words can not be differentiated by both weighting schemes. One may argue that OSS-weighting is more successful at handling the balloon interface, which is expected as it uses strain-weighting, so the reconstructed wave speed that is computed from the data with greater displacement jumps is weighted more, similar to slip-interface imaging [69].

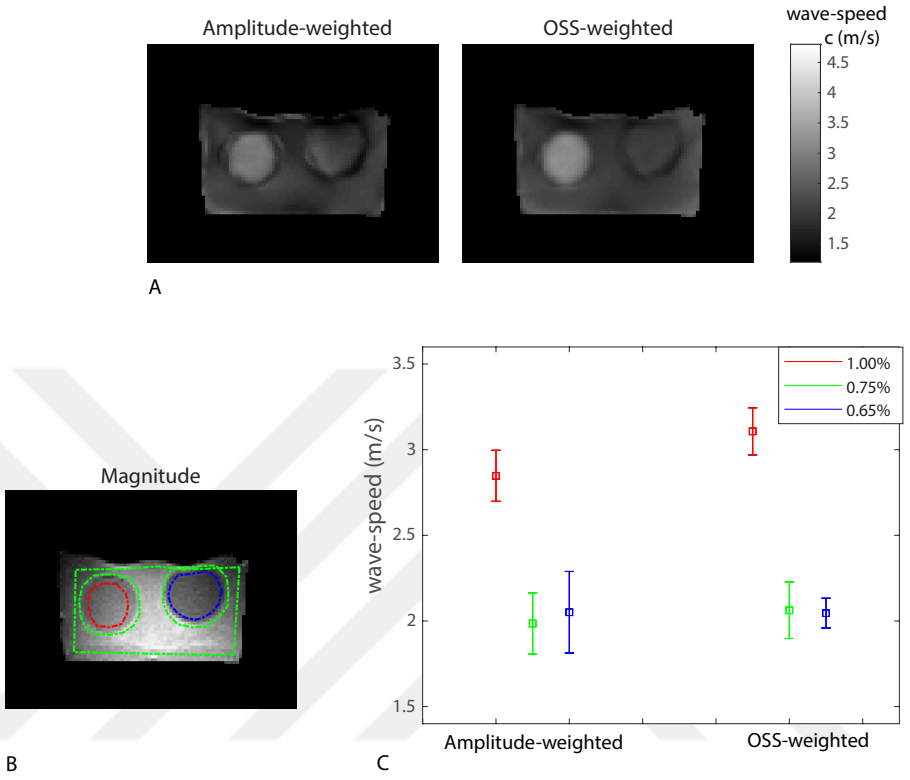


Figure 5.6: For EP#1 (a) Reconstructed wave speed maps (b) Selected ROIs for measuring wave speed values, depicted on the MRE magnitude image. The ROI for the background is selected as the region between the green curves. (c) Mean and SD values over the ROI, shown by squares and bars, respectively.

As observed in Figure 5.7, comparing the weighting schemes used in combining the reconstructed wave speed maps at different frequencies, it can be seen that amplitude-weighting uses single reconstruction result for each pixel, which is computed from the data that carries the maximum displacement and discards the other inversion results, due to using fourth power of the magnitude of the displacement. On the other hand, OSS weighting uses more equally-distributed weights. Unfortunately, reconstructed median wave speed values for 1.75% and 1.50% agar-agar concentrated inclusions can not be differentiated by both weighting schemes Figure 5.8.

Moreover, larger deviations in the amplitude-weighted reconstructed wave speed maps are observed for some parts of the phantoms, compared to the OSS-weighted ones, Figures 5.6C, 5.8B.

Additionally, the mean wave speed of in-vivo liver and spleen were found to be consistent with the values reported in the literature [32, 57].

For the brain model that has been studied, the OSS-weighted Helmholtz inversion resulted in higher resolution maps than the conventional Helmholtz inversion as it can be observed in Figure 5.5. However, both of OSS-weighted and conventional multifrequency Helmholtz inversion results are not the desired elastograms, compared to the ground truth, because of the local homogeneity assumption in Helmholtz inversion. Consistent with the observations for the simulation brain data, human brain elastograms for OSS-weighted and conventional Helmholtz inversion results similar but the OSS-weighted result seems sharper and more sensitive to rapid stiffness changes (Figure 5.10), however, the ground truth is not known.

Although using OSS-weighted Helmholtz inversion recovered some anatomical details better than conventional Helmholtz inversion, these are just two cases that further investigation is required.

In conclusion, OSS-weighted tomoelastography did not promise significant improvements compared to the amplitude-weighted tomoelastography. One may discuss that use of OSS weights can prevent artifacts at the boundaries of encapsulated tumors or tissues with membranes; however this should be examined further.

As future work, OSS weights should be used in an elasticity inversion technique that does not assume local homogeneity and test the inversion on the brain or other tissues, thus it is likely to observe more improvements. Furthermore, OSS weighting may benefit from thresholding by eliminating the displacement data with low strain values in the inversion. Additionally, including Laplacian-SNR weights in the inversion can be compared with OSS-weighted averaging because results in a recent study [38] imply that Laplacian-SNR weights may work better for elasticity inversion techniques that involves second derivative of the displacement field.

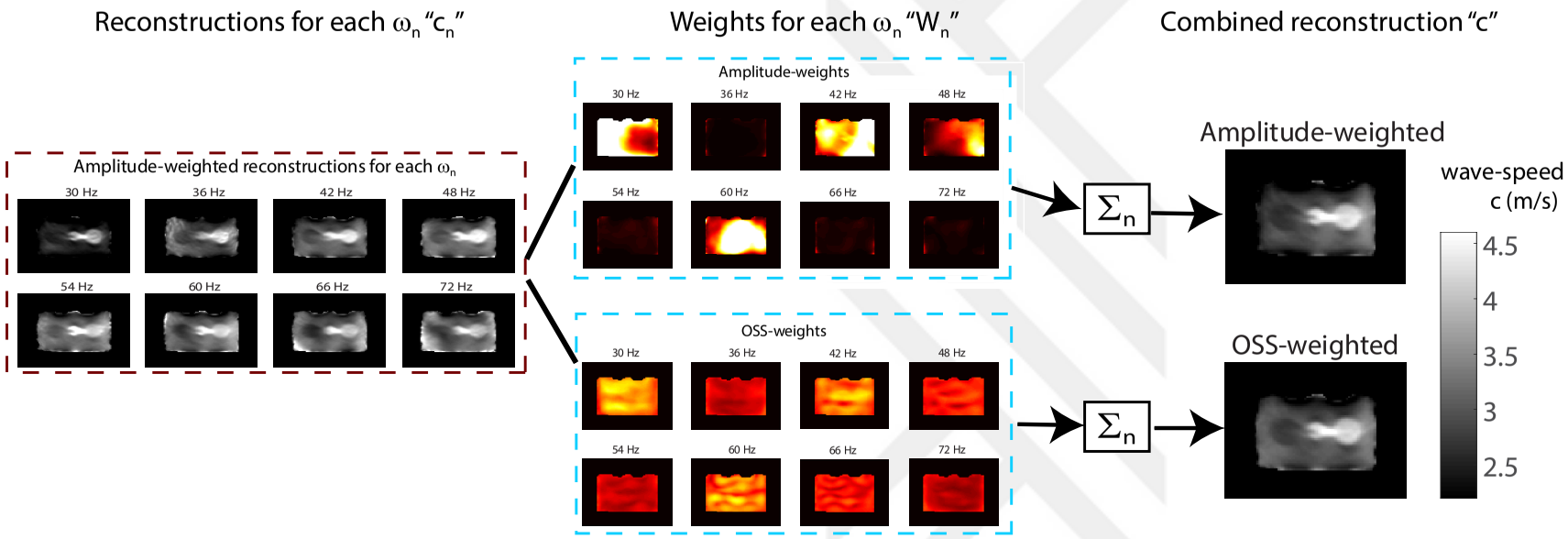


Figure 5.7: Reconstructed wave speed maps and weights for the two weighting schemes at each frequency in addition to the combined wave speed maps for EP#2.

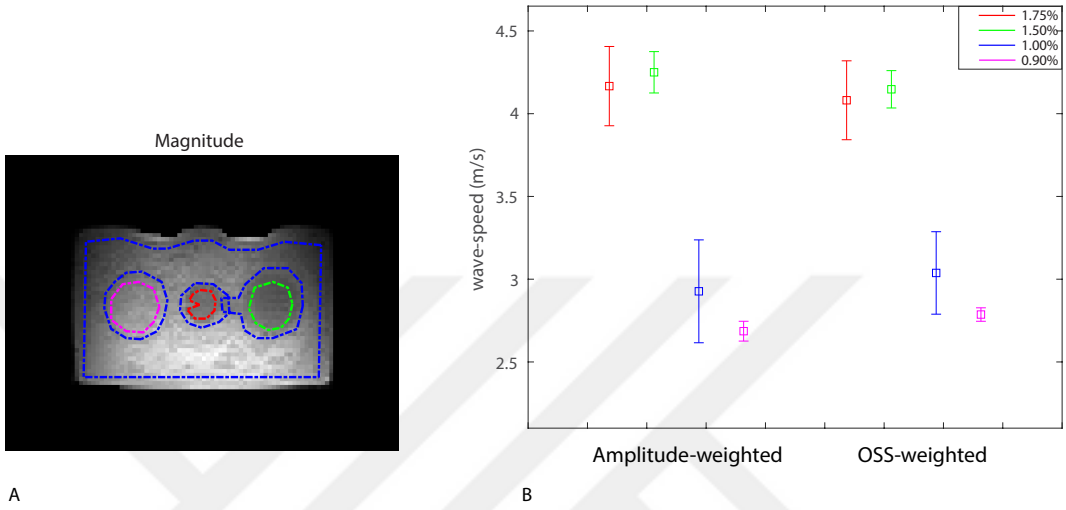


Figure 5.8: For EP#2 (a) Selected ROIs for measuring wave speed values, depicted on the MRE magnitude image. The ROI for the background is selected as the region between the blue curves. (b) Mean and SD values over the ROI, shown by squares and bars, respectively.

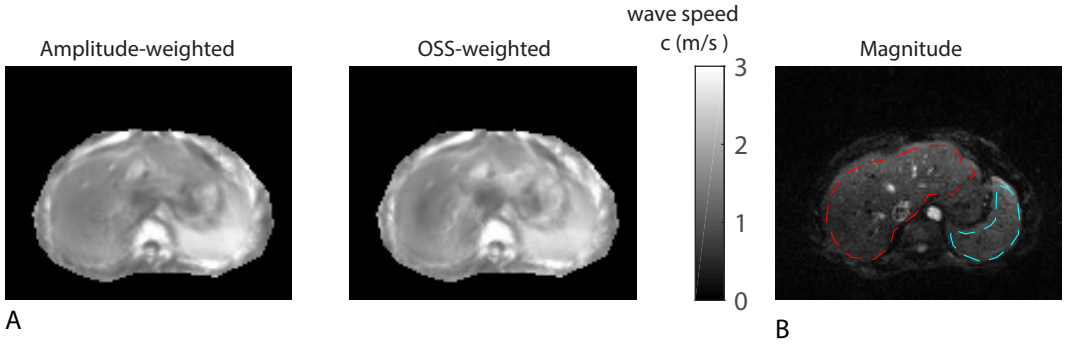


Figure 5.9: (a) Single frequency and combined multifrequency results for wave speed maps for MRE abdomen data. (b) Anatomical ROIs (liver (red) and spleen (blue)), selected on the MRE magnitude image, for measuring the mean and SD of the estimated shear wave speeds.

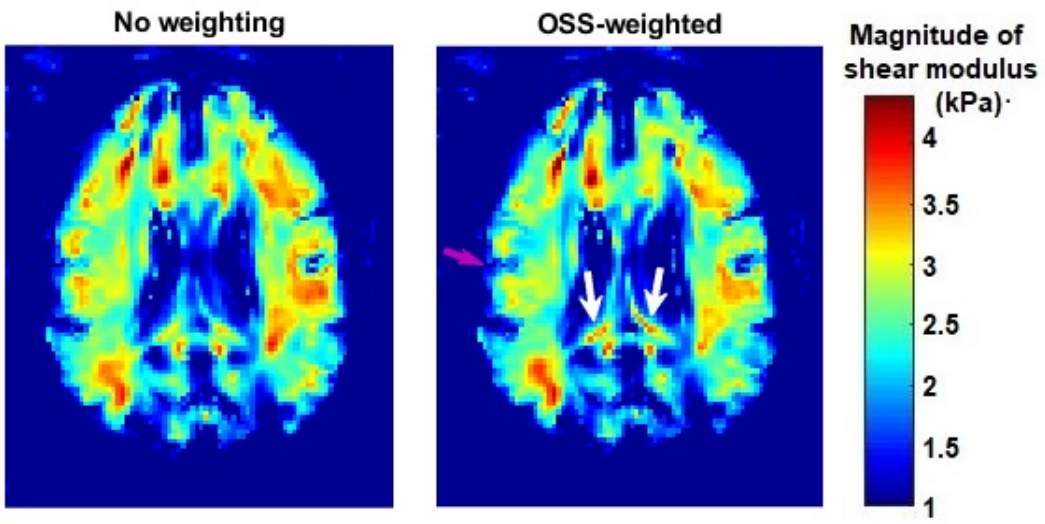


Figure 5.10: Conventional multifrequency Helmholtz inversion (no-weighting) and OSS-weighted Helmholtz inversion for healthy human experiment data. Differences between two images can be observed mainly in splenium of the corpus collosum and sulci, shown by the white arrows and the purple arrow, respectively. Stiff and anisotropic splenium of corpus callosum can be observed in OSS-weighted averaging inversion but it cannot be observed clearly in the inversion without weighting.

Chapter 6

Discussion and Conclusion

In this thesis, frequency response analysis of the elasticity phantoms and the brain were performed. Furthermore, weighting schemes used in combining multiple elasticity maps were studied.

By phantom simulations, experiments and brain simulations, it has been demonstrated that high shear wave displacement, such as 10-20 times of the applied displacement, can be observed at mode frequencies of the tissue during MR elastography. However, further investigation to validate modes of shear waves in human brain is required.

The major challenge was measuring the applied displacement to the head by the bite actuator. In the experiments, only the displacement of the actuator was measured but not how it was transferred to the head. The methodology to measure the input displacement applied to the head during MR elastography can be improved by the recent techniques proposed such as measuring displacement of the head and skull simultaneously [43].

It is also possible that the brain model lacks some important segment or property of the brain which would prevent the formation of modes of shear waves such as isotropy assumption for elasitcity.

If modes of shear waves could be validated by in-vivo experiments, then this would have a few outcomes. First, safety of MRE [19] of the brain should be further investigated. Second, the findings on skull-brain motion transfer can be useful for TBI studies examined by MR elastography [20–22]. Third, beneficial for detecting change in elasticity since mode frequency shifts as the elasticity alters.

Since eigenfrequencies depend on geometry, size, and material parameters of the object [71], the brain development from childhood to adulthood and aging of the brain could be studied by detecting a shift in eigenfrequencies.

The second part of the thesis concentrates on the weighting schemes for combining multiple reconstructed elastograms.

SNR weighting was proposed for tomoelastography and Helmholtz inversions. For both inversions, analytical approximations for SNR of the elasticity map were required. These derivations were carried out with high SNR assumption, thus it was assumed the Gaussian noise on the complex MRI signal remained as Gaussian on the elasticity map despite the nonlinear operations in the inversions.

For tomoelastography, SNR-weighted reconstruction was compared to amplitude-weighted reconstruction for three performance metrics, namely estimation accuracy, edge response analysis and SNR performance. While not altering the accuracy or spatial resolution of the wave speed map with the proposed weighting method, the SNR of the wave speed map has been improved twofold. In addition, bias on the wave speed map was eliminated by using SNR weighting.

For Helmholtz inversion, use of SNR weights improved the SNR of the elastogram 1.6 times and reduced the bias. However, the SNR derivations should be improved by considering second order terms of Taylor expansion.

Furthermore, OSS weighting has been proposed to combine elasticity maps reconstructed for different excitation frequencies in tomoelastography and Helmholtz inversion. In contrast to SNR weighting, OSS weighting is independent

of the inversion that does not require additional derivation. Thus, it can be easily applied to any multifrequency MRE inversion. For OSS weighting, maximum strain is calculated spatially for displacement data at each excitation frequency. No significant improvements were observed by using OSS weights. Although OSS-weighted Helmholtz inversion yielded sharper elastograms, further investigation is necessary.

In conclusion, modes of shear waves might be formed during brain MRE; hence further study on safety and actuation methodologies could be necessary. In addition, the quality of elastograms can be improved by designing weighting schemes for multi-inversion MRE.

Bibliography

[1] R. Muthupillai, D. Lomas, P. Rossman, J. F. Greenleaf, A. Manduca, and R. Ehman, "Magnetic resonance elastography by direct visualization of propagating acoustic strain waves," *Science*, vol. 269, no. 5232, pp. 1854–1857, 1995.

[2] I. Sack, J. Rump, T. Elgeti, A. Samani, and J. Braun, "Mr elastography of the human heart: noninvasive assessment of myocardial elasticity changes by shear wave amplitude variations," *Magnetic Resonance in Medicine*, vol. 61, no. 3, pp. 668–677, 2009.

[3] B. Robert, R. Sinkus, J.-L. Gennisson, and M. Fink, "Application of dense-mr-elastography to the human heart," *Magnetic Resonance in Medicine*, vol. 62, no. 5, pp. 1155–1163, 2009.

[4] L. Huwart, F. Peeters, R. Sinkus, L. Annet, N. Salameh, L. C. ter Beek, Y. Horsmans, and B. E. Van Beers, "Liver fibrosis: non-invasive assessment with mr elastography," *NMR in Biomedicine*, vol. 19, no. 2, pp. 173–179, 2006.

[5] O. Rouviere, M. Yin, M. A. Dresner, P. J. Rossman, L. J. Burgart, J. L. Fidler, and R. L. Ehman, "Mr elastography of the liver: Preliminary results1," *Radiology*, vol. 240, no. 2, pp. 440–448, 2006.

[6] K. Uffmann, S. Maderwald, W. Ajaj, C. G. Galban, S. Mateiescu, H. H. Quick, and M. E. Ladd, "In vivo elasticity measurements of extremity skeletal muscle with mr elastography," *NMR in Biomedicine*, vol. 17, no. 4, pp. 181–190, 2004.

[7] M. A. Dresner, G. H. Rose, P. J. Rossman, R. Muthupillai, A. Manduca, and R. L. Ehman, "Magnetic resonance elastography of skeletal muscle," *Journal of Magnetic Resonance Imaging*, vol. 13, no. 2, pp. 269–276, 2001.

[8] S. Papazoglou, J. Braun, U. Hamhaber, and I. Sack, "Two-dimensional waveform analysis in mr elastography of skeletal muscles," *Physics in Medicine and Biology*, vol. 50, no. 6, p. 1313, 2005.

[9] R. Sinkus, J. Lorenzen, D. Schrader, M. Lorenzen, M. Dargatz, and D. Holz, "High-resolution tensor mr elastography for breast tumour detection," *Physics in medicine and biology*, vol. 45, no. 6, p. 1649, 2000.

[10] A. L. McKnight, J. L. Kugel, P. J. Rossman, A. Manduca, L. C. Hartmann, and R. L. Ehman, "Mr elastography of breast cancer: preliminary results," *American Journal of Roentgenology*, vol. 178, no. 6, pp. 1411–1417, 2002.

[11] S. A. Kruse, G. H. Rose, K. J. Glaser, A. Manduca, J. P. Felmlee, C. R. Jack Jr, and R. L. Ehman, "Magnetic resonance elastography of the brain," *Neuroimage*, vol. 39, no. 1, pp. 231–237, 2008.

[12] P. Latta, M. L. Gruwel, P. Debergue, B. Matwiy, U. N. Sboto-Frankenstein, and B. Tomanek, "Convertible pneumatic actuator for magnetic resonance elastography of the brain," *Magnetic resonance imaging*, vol. 29, no. 1, pp. 147–152, 2011.

[13] U. Hamhaber, I. Sack, S. Papazoglou, J. Rump, D. Klatt, and J. Braun, "Three-dimensional analysis of shear wave propagation observed by in vivo magnetic resonance elastography of the brain," *Acta biomaterialia*, vol. 3, no. 1, pp. 127–137, 2007.

[14] I. Sack, B. Beierbach, U. Hamhaber, D. Klatt, and J. Braun, "Non-invasive measurement of brain viscoelasticity using magnetic resonance elastography," *NMR in Biomedicine*, vol. 21, no. 3, pp. 265–271, 2008.

[15] C. Arıyürek, "Modes of shear wave in magnetic resonance elastography," Master's thesis, Bilkent University, 2014.

[16] D. M. McGrath, N. Ravikumar, I. D. Wilkinson, A. F. Frangi, and Z. A. Taylor, "Magnetic resonance elastography of the brain: An in silico study to determine the influence of cranial anatomy," *Magnetic resonance in medicine*, vol. 76, no. 2, pp. 645–662, 2016.

[17] F. Dittmann, S. Hirsch, H. Tzschätzsch, J. Guo, J. Braun, and I. Sack, "In vivo wideband multifrequency mr elastography of the human brain and liver," *Magnetic resonance in medicine*, vol. 76, no. 4, pp. 1116–1126, 2016.

[18] C. Ariyurek, Y. Ider, N. Gurler, S. Ozdemir, A. Emek, A. Ergun, and E. Atalar, "Modes of shear waves in brain mr elastography," in *In Proceedings of the 22nd Annual Meeting of ISMRM, Milan, Italy*, p. 4270, 2014.

[19] E. Ehman, P. Rossman, S. Kruse, A. V. Sahakian, and K. Glaser, "Vibration safety limits for magnetic resonance elastography," *Physics in Medicine & Biology*, vol. 53, no. 4, p. 925, 2008.

[20] R. J. Okamoto, A. J. Romano, C. L. Johnson, and P. V. Bayly, "Insights into traumatic brain injury from mri of harmonic brain motion," *Journal of experimental neuroscience*, vol. 13, p. 1179069519840444, 2019.

[21] A. A. Badachhape, R. J. Okamoto, C. L. Johnson, and P. V. Bayly, "Relationships between scalp, brain, and skull motion estimated using magnetic resonance elastography," *Journal of biomechanics*, vol. 73, pp. 40–49, 2018.

[22] Z. Yin, Y. Sui, J. D. Trzasko, P. J. Rossman, A. Manduca, R. L. Ehman, and J. Huston III, "In vivo characterization of 3d skull and brain motion during dynamic head vibration using magnetic resonance elastography," *Magnetic resonance in medicine*, vol. 80, no. 6, pp. 2573–2585, 2018.

[23] C. Ariyurek, , S. Ozdemir, A. Ergun, Y. Ider, and E. Atalar, "Use of shear wave mode data in elasticity inversion in mr elastography," in *Proceeding of the 34th Annual Scientific Meeting of ESMRMB, Barcelona, Spain*, p. 343, 2017.

[24] D. Plewes, C. Luginbuhl, C. Macgowan, and I. Sack, "An inductive method to measure mechanical excitation spectra for mri elastography," *Concepts in*

Magnetic Resonance Part B: Magnetic Resonance Engineering: An Educational Journal, vol. 21, no. 1, pp. 32–39, 2004.

[25] A. Manduca, R. Muthupillai, P. Rossman, J. F. Greenleaf, and R. L. Ehman, "Image processing for magnetic-resonance elastography," in *Medical Imaging 1996: Image Processing*, vol. 2710, pp. 616–624, International Society for Optics and Photonics, 1996.

[26] E. E. Van Houten, M. I. Miga, J. B. Weaver, F. E. Kennedy, and K. D. Paulsen, "Three-dimensional subzone-based reconstruction algorithm for mr elastography," *Magnetic Resonance in Medicine: An Official Journal of the International Society for Magnetic Resonance in Medicine*, vol. 45, no. 5, pp. 827–837, 2001.

[27] E. E. Van Houten, M. M. Doyley, F. E. Kennedy, J. B. Weaver, and K. D. Paulsen, "Initial in vivo experience with steady-state subzone-based mr elastography of the human breast," *Journal of magnetic resonance imaging*, vol. 17, no. 1, pp. 72–85, 2003.

[28] A. Manduca, D. S. Lake, S. A. Kruse, and R. L. Ehman, "Spatio-temporal directional filtering for improved inversion of mr elastography images," *Medical image analysis*, vol. 7, no. 4, pp. 465–473, 2003.

[29] S. Papazoglou, U. Hamhaber, J. Braun, and I. Sack, "Algebraic helmholtz inversion in planar magnetic resonance elastography," *Physics in Medicine & Biology*, vol. 53, no. 12, p. 3147, 2008.

[30] S. Hirsch, J. Guo, R. Reiter, S. Papazoglou, T. Kroencke, J. Braun, and I. Sack, "Mr elastography of the liver and the spleen using a piezoelectric driver, single-shot wave-field acquisition, and multifrequency dual parameter reconstruction," *Magnetic resonance in medicine*, vol. 71, no. 1, pp. 267–277, 2014.

[31] S. Papazoglou, S. Hirsch, J. Braun, and I. Sack, "Multifrequency inversion in magnetic resonance elastography," *Physics in Medicine & Biology*, vol. 57, no. 8, p. 2329, 2012.

[32] H. Tzschätzsch, J. Guo, F. Dittmann, S. Hirsch, E. Barnhill, K. Jöhrens, J. Braun, and I. Sack, "Tomoelastography by multifrequency wave number recovery from time-harmonic propagating shear waves," *Medical image analysis*, vol. 30, pp. 1–10, 2016.

[33] A. M. Silva, R. C. Grimm, K. J. Glaser, Y. Fu, T. Wu, R. L. Ehman, and A. C. Silva, "Magnetic resonance elastography: evaluation of new inversion algorithm and quantitative analysis method," *Abdominal imaging*, vol. 40, no. 4, pp. 810–817, 2015.

[34] M. C. Murphy, A. Manduca, J. D. Trzasko, K. J. Glaser, J. Huston III, and R. L. Ehman, "Artificial neural networks for stiffness estimation in magnetic resonance elastography," *Magnetic resonance in medicine*, vol. 80, no. 1, pp. 351–360, 2018.

[35] E. Barnhill, P. J. Davies, C. Ariyurek, A. Fehlner, J. Braun, and I. Sack, "Heterogeneous multifrequency direct inversion (hmdi) for magnetic resonance elastography with application to a clinical brain exam," *Medical image analysis*, vol. 46, pp. 180–188, 2018.

[36] M. McGarry, E. Van Houten, P. Perrinez, A. Pattison, J. Weaver, and K. Paulsen, "An octahedral shear strain-based measure of snr for 3d mr elastography," *Physics in Medicine & Biology*, vol. 56, no. 13, p. N153, 2011.

[37] C. Ariyurek, B. Tasdelen, A. Sadeghi-Tarakameh, Y. Ider, and E. Atalar, "Analysis and maximization of snr in mr elastography inversion," in *In Proceedings of the 27th Annual Meeting of ISMRM, Montréal, Canada*, p. 3962, 2019.

[38] A. Manduca, D. Lake, K. Huynh, R. Eon, E. Annoni, and E. RL., "Consistent snr measures for magnetic resonance elastography," in *In Proceedings of the 23rd Annual Meeting of ISMRM, Toronto, Ontario, Canada*, p. 2519, 2015.

[39] C. L. Johnson, J. L. Holtrop, M. D. McGarry, J. B. Weaver, K. D. Paulsen, J. G. Georgiadis, and B. P. Sutton, "3d multislab, multishot acquisition

for fast, whole-brain mr elastography with high signal-to-noise efficiency," *Magnetic resonance in medicine*, vol. 71, no. 2, pp. 477–485, 2014.

[40] C. Guenthner and S. Kozerke, "Encoding and readout strategies in magnetic resonance elastography," *NMR in Biomedicine*, vol. 31, no. 10, p. e3919, 2018.

[41] U. Hamhaber, F. Grieshaber, J. Nagel, and U. Klose, "Comparison of quantitative shear wave mr-elastography with mechanical compression tests," *Magnetic Resonance in Medicine: An Official Journal of the International Society for Magnetic Resonance in Medicine*, vol. 49, no. 1, pp. 71–77, 2003.

[42] D. C. Ghiglia and M. D. Pritt, "Two-dimensional phase unwrapping: theory, algorithms, and software," *Wiely-Interscience, first ed.(April 1998)*, 1998.

[43] Y. Sui, M. In, A. Manduca, M. A. Bernstein, R. L. Ehman, J. I. Huston, and Z. Yin, "Simultaneous fat-water mr elastography imaging using distortion-free diadem-epi," in *In Proceedings of the 28th Annual Meeting of ISMRM*, p. 3309, 2020.

[44] A. Romano, M. Scheel, S. Hirsch, J. Braun, and I. Sack, "In vivo waveguide elastography of white matter tracts in the human brain," *Magnetic resonance in medicine*, vol. 68, no. 5, pp. 1410–1422, 2012.

[45] D. Tweten, R. Okamoto, and P. Bayly, "Requirements for accurate estimation of anisotropic material parameters by magnetic resonance elastography: A computational study," *Magnetic resonance in medicine*, vol. 78, no. 6, pp. 2360–2372, 2017.

[46] M. D. McGarry, E. Van Houten, C. Guertler, R. J. Okamoto, D. R. Smith, D. R. Sowinski, C. L. Johnson, P. Bayly, J. Weaver, and K. D. Paulsen, "A heterogenous, time harmonic, nearly incompressible transverse isotropic finite element brain simulation platform for mr elastography," *Physics in Medicine & Biology*, 2020.

[47] D. R. Smith, C. A. Guertler, R. J. Okamoto, A. J. Romano, P. V. Bayly, and C. L. Johnson, "Multi-excitation magnetic resonance elastography of the

brain: Wave propagation in anisotropic white matter," *Journal of Biomechanical Engineering*, vol. 142, no. 7, 2020.

[48] G. Bertalan, J. Guo, H. Tzschätzsch, C. Klein, E. Barnhill, I. Sack, and J. Braun, "Fast tomoelastography of the mouse brain by multifrequency single-shot mr elastography," *Magnetic resonance in medicine*, vol. 81, no. 4, pp. 2676–2687, 2019.

[49] D. Klatt, U. Hamhaber, P. Asbach, J. Braun, and I. Sack, "Noninvasive assessment of the rheological behavior of human organs using multifrequency mr elastography: a study of brain and liver viscoelasticity," *Physics in Medicine & Biology*, vol. 52, no. 24, p. 7281, 2007.

[50] K. J. Parker, M. M. Doyley, and D. J. Rubens, "Imaging the elastic properties of tissue: the 20 year perspective," *Physics in medicine & biology*, vol. 56, no. 1, p. R1, 2010.

[51] P. Kalra, B. Raterman, X. Mo, and A. Kolipaka, "Magnetic resonance elastography of brain: Comparison between anisotropic and isotropic stiffness and its correlation to age," *Magnetic resonance in medicine*, vol. 82, no. 2, pp. 671–679, 2019.

[52] A. Manduca, D. Lake, K. Huynh, R. Eon, E. Annoni, and R. Ehman, "Consistent snr measures for magnetic resonance elastography," in *In Proceedings of the 23rd Annual Meeting of ISMRM, Toronto, ON*, p. 2519, 2015.

[53] A. Manduca, T. E. Oliphant, M. A. Dresner, J. Mahowald, S. A. Kruse, E. Amromin, J. P. Felmlee, J. F. Greenleaf, and R. L. Ehman, "Magnetic resonance elastography: non-invasive mapping of tissue elasticity," *Medical image analysis*, vol. 5, no. 4, pp. 237–254, 2001.

[54] M. Unser and M. Eden, "Weighted averaging of a set of noisy images for maximum signal-to-noise ratio," *IEEE transactions on acoustics, speech, and signal processing*, vol. 38, no. 5, pp. 890–895, 1990.

[55] M. A. Bernstein and Y. Ikezaki, "Comparison of phase-difference and complex-difference processing in phase-contrast mr angiography," *Journal of Magnetic Resonance Imaging*, vol. 1, no. 6, pp. 725–729, 1991.

[56] J. W. Massey and A. E. Yilmaz, "Austinman and austinwoman: High-fidelity, anatomical voxel models developed from the vhp color images," in *2016 38th Annual International Conference of the IEEE Engineering in Medicine and Biology Society (EMBC)*, pp. 3346–3349, IEEE, 2016.

[57] F. Dittmann, H. Tzschätzsch, S. Hirsch, E. Barnhill, J. Braun, I. Sack, and J. Guo, "Tomoelastography of the abdomen: Tissue mechanical properties of the liver, spleen, kidney, and pancreas from single mr elastography scans at different hydration states," *Magnetic resonance in medicine*, vol. 78, no. 3, pp. 976–983, 2017.

[58] Y. K. Mariappan, K. J. Glaser, and R. L. Ehman, "Magnetic resonance elastography: a review," *Clinical anatomy*, vol. 23, no. 5, pp. 497–511, 2010.

[59] A. Kolipaka, D. Woodrum, P. A. Araoz, and R. L. Ehman, "Mr elastography of the in vivo abdominal aorta: a feasibility study for comparing aortic stiffness between hypertensives and normotensives," *Journal of Magnetic Resonance Imaging*, vol. 35, no. 3, pp. 582–586, 2012.

[60] "Mmre liver data. bioqic apps website. https://bioqic-apps.charite.de/downloads," Published November 06, 2018. Accessed November 07, 2018.

[61] M. Yin, J. A. Talwalkar, K. J. Glaser, S. K. Venkatesh, J. Chen, A. Manduca, and R. L. Ehman, "Dynamic postprandial hepatic stiffness augmentation assessed with mr elastography in patients with chronic liver disease," *American Journal of Roentgenology*, vol. 197, no. 1, pp. 64–70, 2011.

[62] C. D. Constantinides, E. Atalar, and E. R. McVeigh, "Signal-to-noise measurements in magnitude images from nmr phased arrays," *Magnetic Resonance in Medicine*, vol. 38, no. 5, pp. 852–857, 1997.

[63] M. A. Green, L. E. Bilston, and R. Sinkus, "In vivo brain viscoelastic properties measured by magnetic resonance elastography," *NMR in Biomedicine: An International Journal Devoted to the Development and Application of Magnetic Resonance In vivo*, vol. 21, no. 7, pp. 755–764, 2008.

[64] D. Klatt, S. Papazoglou, J. Braun, and I. Sack, "Viscoelasticity-based mr elastography of skeletal muscle," *Physics in Medicine & Biology*, vol. 55, no. 21, p. 6445, 2010.

[65] D. Fovargue, S. Kozerke, R. Sinkus, and D. Nordsletten, "Robust mr elastography stiffness quantification using a localized divergence free finite element reconstruction," *Medical image analysis*, vol. 44, pp. 126–142, 2018.

[66] E. H. Clayton, J. R. Garbow, and P. Bayly, "Frequency-dependent viscoelastic parameters of mouse brain tissue estimated by mr elastography," *Physics in Medicine & Biology*, vol. 56, no. 8, p. 2391, 2011.

[67] J. Rump, D. Klatt, J. Braun, C. Warmuth, and I. Sack, "Fractional encoding of harmonic motions in mr elastography," *Magnetic Resonance in Medicine: An Official Journal of the International Society for Magnetic Resonance in Medicine*, vol. 57, no. 2, pp. 388–395, 2007.

[68] C. Ariyurek, B. Tasdelen, E. Barnhill, A. Ergun, Y. Ider, and E. Atalar, "Usage of octahedral shear strain weights in the inversion of multifrequency mr elastography," in *In Proceedings of the 26th Annual Meeting of ISMRM, Paris, France*, p. 1076, 2018.

[69] Z. Yin, K. J. Glaser, A. Manduca, J. J. Van Gompel, M. J. Link, J. D. Hughes, A. Romano, R. L. Ehman, and J. Huston III, "Slip interface imaging predicts tumor-brain adhesion in vestibular schwannomas," *Radiology*, vol. 277, no. 2, pp. 507–517, 2015.

[70] T. E. Oliphant, A. Manduca, R. L. Ehman, and J. F. Greenleaf, "Complex-valued stiffness reconstruction for magnetic resonance elastography by algebraic inversion of the differential equation," *Magnetic Resonance in Medicine: An Official Journal of the International Society for Magnetic Resonance in Medicine*, vol. 45, no. 2, pp. 299–310, 2001.

[71] P. M. Morse, *Theoretical acoustics*. Princeton University Press, 1986.